SCINTILLATOR CANDIDATE COMPOUNDS

By

David Michael Smiadak

A THESIS

Submitted to
Michigan State University
in partial fulfillment of the requirements
for the degree of

Materials Science and Engineering - Master of Science

2015

ABSTRACT

SCINTILLATOR CANDIDATE COMPOUNDS

By

David Michael Smiadak

Crystals with composition $MgTa_2O_6$ and Ce:LuAG were synthesized using the micro-pulling-down method. The crystals were prepared from powdered oxides and the results were characterized with x-ray powder diffraction, x-ray luminescence, scanning electron microscopy, and energy-dispersive x-ray spectroscopy.

Analysis confirmed single crystal growths of Ce:LuAG while two phases were identified in the $MgTa_2O_6$ growths. Production parameters for these crystal growths are detailed. Further development is required in the case of $MgTa_2O_6$ as growth results did not produce detectable emission spectra required of scintillators.

The growth of single crystal Ce:LuAG was confirmed and the spectral analysis matched those of published values. Ce:LuAG was confirmed to be an appropriate scintillator material that can be grown with in-house equipment at Lawrence Berkeley National Laboratory. Scanning electron microscopy and energy-dispersive x-ray spectroscopy testing were performed at Michigan State University.

For my wonderful wife Saeeda

ACKNOWLEDGEMENTS

I would like to thank all of the individuals at both Michigan State University and Lawrence Berkeley National Laboratory whom assisted me in my pursuit of a Master of Science Degree in Materials Science and Engineering at Michigan State University. Dr. Carl Boehlert has been both generous with his time and flexible with this project's scope, allowing me the opportunity to extend my work from Lawrence Berkeley National Laboratory with experimental analysis at Michigan State University. His technical assistance has been invaluable with shaping the scope of this project. I would also like to thank my thesis committee members Dr. Phillip Eisenlohr and Dr. Donald Morelli for their technical assistance and advice. I would like to thank both Dr. Edith Bourret-Courchesne and Dr. Didier Perrodin at Lawrence Berkeley National Laboratory for their invaluable assistance and guidance in the synthesis and characterization of the scintillator candidate compounds. I would also like to thank Dr. Gregory Bizarri, Dr. Ivan Khodyuk, Dr. Martin Gascon, and Dr. Tetiana Shalapaka at Lawrence Berkeley National Laboratory for their brain-storming and research suggestions as well as Dr. Paul Lecoq from CERN. I would like to thank Chris Rosen for his assistance in powder synthesis and x-ray powder diffraction testing at Lawrence Berkeley National Laboratory as well. I would also like to acknowledge the financial support provided by the Department of Homeland Security's Domestic Nuclear Detection Office. Finally, I would like to express my very great appreciation to my parents, Pam and Matt Smiadak for their unwaivering love and support.

TABLE OF CONTENTS

LIST OF TABLES

LIST OF FIGURES

KEY TO ABBREVIATIONS

μ-PD micro-pulling-down.

AC alternating current.

AE auto exposure.

AG analog gain.

ATM atmosphere.

BD Bridgman.

CB conduction band.

CCD charge coupled detector.

Ce:LuAG cerium doped lutetium aluminum garnet.

Ce:YAG cerium doped yttrium aluminum garnet.

Ce:YAP cerium doped yttrium aluminium perovskite.

CT x-ray computed tomography.

CV core-valence.

CX charge-transfer.

CZ Czochralski.

EDS energy-dispersive x-ray spectroscopy.

EFG edge-defined-film-fed.

FPS frames-per-second.

FWHM full width at half maximum.

FZ floating zone.

HE high-energy.

HEP high-energy physics.

HP hydraulically-pressed.

ICDD International Centre for Diffraction Data.

IDE integrated development environment.

IDLE Integrated DeveLopment Environment.

IR infrared.

LBNL Lawrence Berkeley National Laboratory.

LHC Large Hadron Collider.

LPF Linus Pauling File.

LuAG lutetium aluminum garnet.

LVSEM low-vacuum scanning electron microscopy.

LY light yield.

MAG magnification.

MP manually-pressed.

NP non-pressed.

OD outer diameter.

OE optical excitation.

OP-S oxide polishing suspension.

PC personal computer.

PET positron emission tomography.

PMT photomultiplier tubes.

PSI pounds per square inch.

RE rare earth.

RF radio-frequency.

RPM rotations per minute.

RT room temperature.

SA self-activated.

SE secondary electrons.

SEM scanning electron microscopy.

SP set-point.

SSC Superconducting Super Collider.

SX self-trapped exciton.

TEAM Texture and Elemental Analytical Microscopy.

UV ultraviolet.

VB Visual Basic.

VB valence bands.

XRL x-ray luminescence.

XRPD x-ray powder diffraction.

YAG yttrium aluminum garnet.

Introduction: Scintillator Principles and Properties

The objective of this study was to produce single crystals of desired compounds, evaluate the growth, and draw conclusions about their feasibility as a scintillator. A crystal is a solid consisting of a regular periodic arrangement of atoms.

A scintillator is a material possessing luminescent centers that absorbs high-energy photons and emits light in the visible or near-visible spectrum. The energy levels involved in this radiative transition must occur in the energy gap so that the emitted light is not lost through reabsorption. This transition has proven useful for detecting both x-ray and γ-ray photons.[1]

Scintillators exist as organics, inorganics, glasses, liquids, and gases. This study focuses on inorganic single crystal scintillators for applications in the field of high-energy physics (HEP) particle detection.

Scintillators are used in conjunction with photosensitive devices that are able to quantify the emitted visible light. These devices include photo-diodes and photomultiplier tubes (PMT).

In order to better understand the process of scintillation, it is useful to first describe the band structure of a material. This band structure is divided into three critical regions: conduction band (CB), valance band (VB), and the energy gap (E_g) that separates them.

The CB consists of electrons that have sufficient energy to travel throughout the crystal while the VB consists of electrons that are bound to the lattice structure. The CB and the VB are separated by the energy gap where no electron states exist.

Electrons can be promoted to the CB by absorbing energy from radiation interactions. This is the driving mechanism behind scintillation. Direct de-excitation through photon emission can be inefficient, with the resultant photon carrying energy beyond the visible spectrum. This excess energy can not be counted by photo-detection. Here is where the need for scintillators arises, to shift the wavelength of the photon into the visible or near visible spectrum.

In order to enhance photon emission, a small amount of impurity can be introduced into the lattice. This impurity is referred to as an activator or dopant. These activators create special energy sites within the lattice where the normal energy band structure is modified. These special energy sites can be within the traditionally forbidden energy gap where electrons can de-excite to the VB.

[1] B.C. Grabmaier, W. Rossner, and J. Leppert. Ceramic scintillators for x-ray computed tomography. *Physica Status Solidi (a)*, 130(2):K183–K187, April 1992

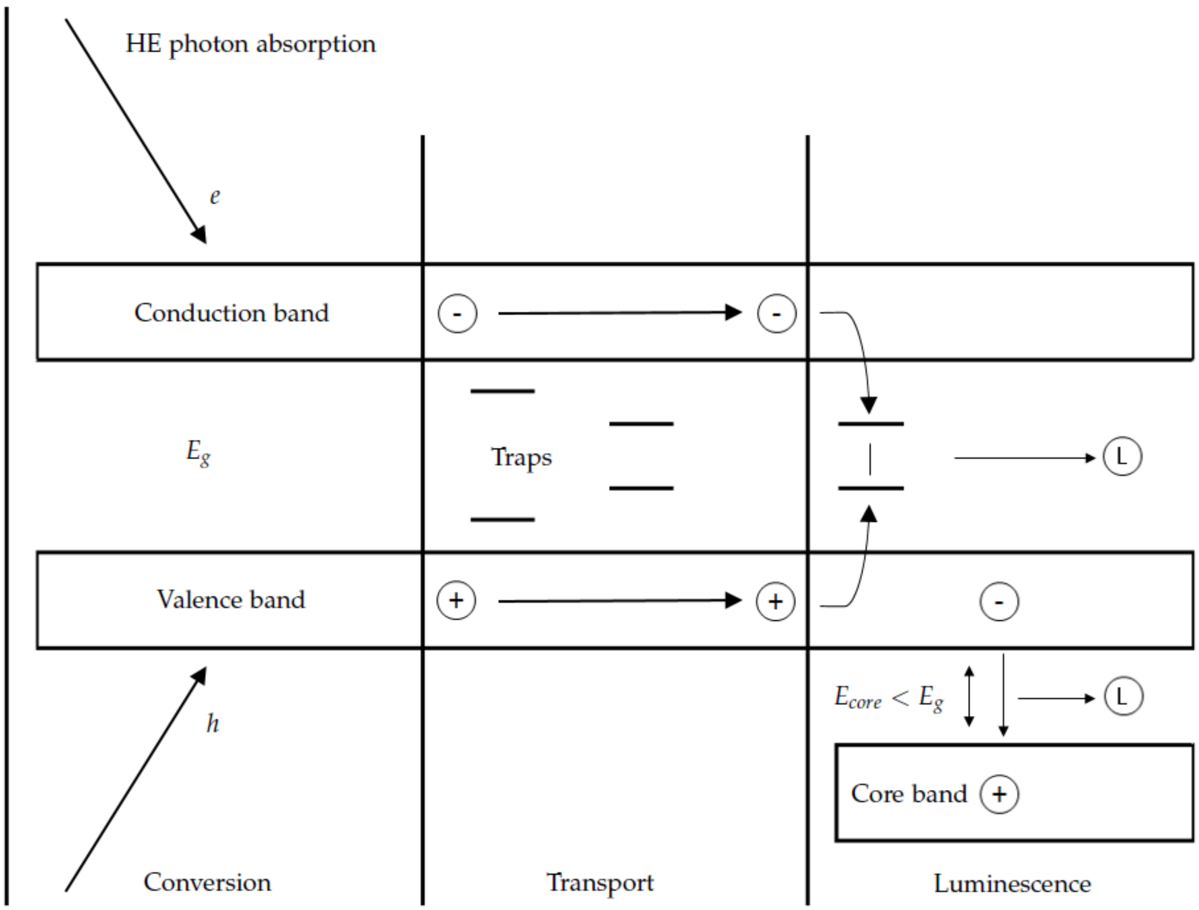

Figure 1: Sketch of scintillator conversion of a high energy (HE) photon.[14]

Due to the smaller energy of these activator sites, transitions between these sites and the VB result in photons with lower energies. This lower energy brings these photons into the visible or near-visible spectrum of emissions. These activator sites are referred to as luminescence centers or recombination centers when they reside in the energy gap.

This trapping of electrons is useful because these localized energy levels reside in the energy gap and avoid recombination with the lattice, allowing for light to escape the scintillator material. Electrons in this state become temporarily removed from the CB.[2]

Inorganic scintillation can be described in three phases:

1. Ionization event that creates an inner shell electron-hole and an energetic primary electron.
2. When the electron energy becomes less than the ionization threshold, electrons and electron-holes thermalize. This in turn transfers electrons to excite the luminescent centers in the energy gap.
3. Excited luminescent species relax to the ground state and emission of scintillation light occurs.

While each process occurs with characteristic time constants. the emission of scintillation light varies widely due to the quantum wave-function characteristics of the levels involved in these transitions.[3] Due to these complexities. predictive computational modeling has proved difficult in defining these time constants with experimentalists exploring well ahead of what computational modeling can reliably predict.[4]

Inorganic Scintillator: Properties

Inorganic scintillators are the focus of this study. Important properties that are considered when evaluating scintillator candidate materials are physical density, transparency, production and machinability, light yield, linearity of light output, decay time, and afterglow.

Physical Density

High physical density is critically important for high energy applications due to its inherently higher stopping power provided by the host lattice. Scintillators also benefit from elements with high effective atomic numbers (Z_{eff}), which have a larger physical size within the lattice to stop high energy particles within the crystal. Additionally, a higher density also reduces the physical size of a detector which is important for field applications.

---

[2] S. Kasap. *Principles of Electronic Materials and Devices*. McGraw-Hill Education, third edition, March 2005

[3] P. Lecoq, A. Annenkov, A. Gektin, M. Korzhik, and C. Pedrini. *Inorganic Scintillators for Detector Systems: Physical Principles and Crystal Engineering*. Springer-Verlag, first edition, 2006

[4] M.J. Weber. Inorganic scintillators: today and tomorrow. *Journal of Luminescence*, 100(1-4):35–45, 2002

Transparency

The transparency of a scintillator directly relates to its ability to transport photon scintillation to a coupled photo-detector. Scintillators typically absorb high-energy particles at their entrance face and this energy makes it to the other side of the crystal through a combination of reflections and scattering both at surfaces and within the material. Minimizing this visible photon path length is critical. Longer photon path lengths can be further susceptible to optical absorption and efficiency changes due to radiation damage.[5]

Production and Machinability

Ease of production and machinability are important when determining appropriate scintillator candidate materials. Significant cost can be accrued through equipment, production and the acquisition of raw materials.

End use of crystals typically require them to be installed in detectors with specific repeatable crystal geometry. Cleavage of single crystals can also be a concern. Incorrect orientation during machining can fracture a single crystal in unintended ways.

Additionally, a crystal must have appropriate chemical, mechanical, and radiation hardness. Crystals that do not undergo phase transformation or decompose into constitutive compounds between their melting temperature and RT are preferred because they are easier to produce.

Light Yield

A high light yield (LY), measured in photons/MeV, is desirable for most scintillator applications. For medical application, scintillators with high LY can reduce the amount of time a patient is exposed to radiation. Scintillator LY is largely driven by the processes that excite the luminescence centers of the scintillating ions.

The number of visible/UV photons, N_{ph}, produced per energy can be expressed as,

$$N_{\mathrm{ph}} = \frac{E}{\beta E_{\mathrm{g}}} \cdot S \cdot Q \tag{1}$$

where E is energy, β represents the average energy required to produce one thermalized electron-hole pair, E_{g} is the energy gap, S and Q are the quantum efficiencies of the transport and luminescence stages, respectively. The average energy required to produce a thermalized electron-hole pair, relates to the energy such that,

$$E_{\text{e-h}} = \beta E_{\mathrm{g}} \tag{2}$$

[5] C. Greskovich and S. Duclos. Ceramic scintillators. *Annual Review of Materials Science*, 27(1):69–88, August 1997

with $\beta \approx 2 - 3$.[6] The relative efficiency of a scintillator, η, can be expressed as,

$$\eta = \frac{E_{\text{gen}} N_{\text{ph}}}{E} \tag{3}$$

where E_{gen} is the energy of the UV/visible photon. One of the most efficient scintillators currently produced is ZnS:Ag with an efficiency of $\eta \approx 0.2$.

Another factor to consider when evaluating a scintillator candidate is the energy resolution of the scintillator and accompanying photodetector needed. Conventional solid state semi-conductors or photomultiplier-based photodetectors can detect generated visible or UV light with high sensitivity.[7] Energy resolution is most commonly defined as a system's ability to discriminate between γ-photons of different energies. This energy resolution is defined by the full width at half maximum (FWHM) of the photo-peak at a given energy divided by its energy. This value is thus a function of LY.

Linearity of Light Output

The ideal scintillator material would be able to convert each γ-photon to a photon of reduced energy in the visible spectrum. Each candidate material possesses less than ideal conversion due to an inhomogeneous scintillator micro-structure and Compton scattering. Compton scattering is the scattering of a photon by a charged particle, typically an electron. This decreases the energy and increases the wavelength of the affected photon.

Additionally, discrepancies in micro-structure can lead to spatial difference that lead to unique conversion efficiencies where Compton scattering produces electrons of varying lower energies. Proportionality is critically important when it comes to determine energy resolutions because non-linear deviations in LY are detrimental to scintillator performance.

Decay Time

Decay time, also referred to as scintillator response, is an important factor in determining the time resolution of a scintillator. The faster the decay time of the luminescent ion, the better the timing resolution. The radiative lifetime, τ, of the luminescent center is desired to be short for medical application because it can limit the time necessary for an individual to be exposed to the radiation. The 4f-5d optical transition produced by ions such as Ce^{3+} exhibit a typical decay time of 10-60 ns range.

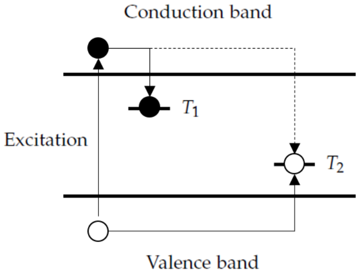

Figure 2: The afterglow mechanism where either an excitation event creates a free electron and electron-hole. The electron-hole is trapped at T_2 while the electron is trapped at T_1, only arriving at T_2 after a delay.[7]

[6] C.W.E. van Eijk. Inorganic-scintillator development. *Nuclear Instruments and Methods in Physics Research Section A: Accelerators, Spectrometers, Detectors and Associated Equipment*, 460(1):1–14, 2001

[7] G. Dhanaraj. *Springer Handbook of Crystal Growth*. Springer-Verlag, first edition, 2010

Afterglow

Afterglow is the fraction of scintillating light present for a given period of time once the ionizing radiation has stopped. It is often desirable for this effect to be minimized or eliminated completely. If not controlled for a specific application it will take more time to discriminate between γ-photons, decreasing timing resolution.[8]

Afterglow can be significantly longer than the radiative lifetime and occurs because of delayed radiant recombination of electrons and electron-holes due to the trapping of either as shown in Figure 2.

Inorganic Scintillator: Mechanisms

Many of the scintillation mechanisms are related to excitons which can be described as an electrically neutral quasiparticle. This exciton state occurs where an electron and an electron-hole are attracted to each other by electrostatic Coulomb forces as shown in Figure 3.

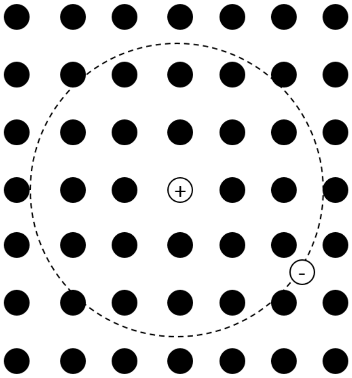

Figure 3: Frenkel exciton, a bound state of attraction between an electron and electron-hole.

Examples of final stage luminescence in scintillators includes free and impurity-bound excitons, and self-trapped exciton (SX). Some scintillators are considered self-activated (SA) while others use activator/dopant ions, core-valence (CV) luminescence, or charge-transfer (CX) emission.

Intrinsic scintillator materials are self-activated and can involve electron and electron-hole recombination. Additional mechanisms for self-activation involve exciton luminescence by either free, self-trapped or defect-trapped exciton states.[9]

Extrinsic scintillator materials are externally activated, typically associated with a dopant ion. Examples of these dopant ions include Tl^{+}, Ce^{3+}, and Eu^{2+}.[10]

Free and impurity-bound exciton

Excitons are formed when an ionization electron and electron-hole are bound into pair states. This is largely considered a low temperature mechanism that is bound as an entity to an impurity atom or defect. At room temperature (RT) this emission type is weak because the exciton state is quickly disassociated.

Self-trapped exciton

The SX case describes an ionization electron-hole localizing on one or more atoms with associated lattice relaxation. The effect results from the trapping of a spatially diffuse electron as shown in Figure 4.

[8] C.R. Ronda and A.M. Srivastava. *Scintillators*, chapter 5, pages 105–132. Wiley-VCH Verlag GmbH and Co. KGaA, 2007

[9] S.E. Derenzo, M.J. Weber, E.D. Bourret-Courchesne, and M.K. Klintenberg. The quest for the ideal inorganic scintillator. *Nuclear Instruments and Methods in Physics Research Section A: Accelerators, Spectrometers, Detectors and Associated Equipment*, 505(1-2):111–117, 2003

[10] M.J. Weber. Scintillation: mechanisms and new crystals. *Nuclear Instruments and Methods in Physics Research Section A: Accelerators, Spectrometers, Detectors and Associated Equipment*, 527(1-2):9–14, 2004

Self-activated

In SA driven scintillators the luminescent species is a constituent of the crystal. This mechanism typically has reduced decay time and luminosity at RT.

Activator ions

This extrinsic mechanism is driven by dopant ions such as Tl^+, Ce^{3+}, and Eu^{2+}. The ionization electron-holes and electrons are trapped on the same luminescent ion that falls within the energy gap. The specific activator ion explored in this study is the Ce^{3+} 5d→4f transition for the Ce doped Ce:LuAG single crystal. At RT, the 5d→4f transition of Ce^{3+} center can be exploited for fast and efficient scintillation in both yttrium aluminum garnet (YAG) and lutetium aluminum garnet (LuAG) matrices.

Rare earth ions are characterized by an incompletely filled 4f shell. The Ce^{3+} ion deals specifically with an electron that returns from the 5d orbital to the 4f orbital. Of the trivalent ions, Ce^{3+} is the simplest case with its single electron with the excited 5d configuration.[11]

The 5d→4f transition shown in Ce^{3+} doped scintillators produces a high LY in the visible region with time responses in the nanosecond range.[12]

Ions such as Ce^{3+} and Pr^{3+} are important dopants in scintillators because they occur in more than one valence state and can induce photoionization. The energy gap must be large enough to accommodate these additional energy traps for utilization. It is important to note that the energy gap can not be too large because this reduces the light yield of the scintillator.[13]

An important consideration in these crystals is inhomogeneous distributions of the dopant. Inhomogeneous distributions are associated with the dependence of the segregation coefficient of dopant on the crystallization rate. As a result, the activator distribution is not uniform through the fiber. The core of a crystal will have a lower scintillation efficiency relative to its perimeter.[14] This efficiency can be expressed as,

$$k_{\text{eff}} = k\left[k + (1-k)\exp\left(-\frac{V\delta}{D}\right)\right]^{-1} \tag{4}$$

where $k = C_S/C_L$ in which C_S and C_L are the activator concentration in crystals and melt, D is the diffusion coefficient, V is the growth rate, and δ is the distance of the solidification interface.

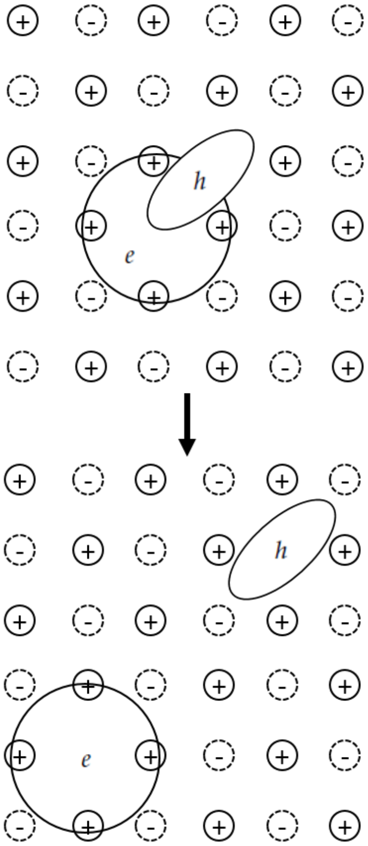

Figure 4: Self-trapped exciton.

---

[11] G. Blasse and B.C. Grabmaier. *Luminescent Materials*. Springer-Berlin Heidelberg, first edition, 1994

[12] C.W.E. van Eijk, J. Andriessen, P. Dorenbos, and R. Visser. Ce^{3+} doped inorganic scintillators. *Nuclear Instruments and Methods in Physics Research Section A: Accelerators, Spectrometers, Detectors and Associated Equipment*, 348(2-3):546–550, 1994

[13] M. Nikl, J.A. Mares, N. Solovieva, J. Hybler, A. Voloshinovskii, K. Nejezchleb, and K. Blazek. Energy transfer to the Ce^{3+} centers in $Lu_3Al_5O_{12}$:Ce scintillator. *Physica status solidi*, 201(7):R41 – R44, May 2004

[14] A.V. Gektin. *Trends in Scintillation Crystals*, chapter 17, pages 299–312. Wiley-VCH Verlag GmbH and Co. KGaA, 2010

Core-valence luminescence

The CV mechanism occurs when the energy gap between the VB and the top core band is less than the fundamental energy gap. This CV transition is responsible for a fast sub-nanosecond luminescence, characteristic of CV luminescence.[15] This mechanism is also depicted in Figure 1.

Charge-transfer

Lastly, the CX mechanism is characterized by the excitation of radiative centers resulting from an energy transfer from excited states.

Inorganic Scintillator: Applications & Requirements

Scintillators have a variety of applications and consequently different material requirements. A broader category of scintillators used within counting technique devices can be generalized. These applications include HEP calorimeter for SSC/LHC, nuclear physics, astrophysics, PET, gamma cameras, neutrons, and industrial applications. These applications demand high light yields but vary in requirements for short decay times. Decay times for astrophysics and gamma cameras are typically less important.

Densities across these applications are preferred high with the exception of neutron counting. Ruggedness is also a critical factor for non-laboratory applications in industry and use in the field.

Integrating technique applications include x-ray computed tomography (CT) and x-ray imaging. Both of these applications require high light yields. Additionally, CT has strict requirements for decay time and no afterglow is ideal. Decay time is considered less important in x-ray imaging.[16]

Historical Development

Inorganic scintillators have been studied for well over a century with the last seventy-five years having shown the most productive development and refinement of scintillators for both medical and industrial application. A list of influential scintillators is shown in Table 1.

1896-1939

The earliest scintillators were highlighted by the discovery of calcium tungstate ($CaWO_4$) and zinc sulfide (ZnS). Notable achievements included the discovery of x-rays by Wilhelm Röntgen, radioactivity by Henri Becquerel, and α-particle scattering by

[15] P. Lecoq, A. Annenkov, A. Gektin, M. Korzhik, and C. Pedrini. *Inorganic Scintillators for Detector Systems: Physical Principles and Crystal Engineering*. Springer-Verlag, first edition, 2006

[16] C.W.E. van Eijk, J. Andriessen, P. Dorenbos, and R. Visser. Ce^{3+} doped inorganic scintillators. *Nuclear Instruments and Methods in Physics Research Section A: Accelerators, Spectrometers, Detectors and Associated Equipment*, 348(2-3):546–550, 1994

Ernest Rutherford. The observation of α-particles is widely considering the starting point of modern nuclear physics. William Crookes then used ZnS to count radioactive particles, marking the beginning of scintillator commercialization.

1940-1980

A push of exploration fueled by World War II and the Cold War yielded scintillation properties of most pure and activated alkali halide crystals. This period of scintillator development was highlighted with the development of the PMT and experimental physics where scintillators found a critical role in the detection of elementary particles and to measure their frequency.

1980-Present

Modern development of scintillators has focused on precision applications in HEP and high light outputs demanded from medical imaging applications.

Compound	Mechanism	Density (g/cm^3)	Light Yield $(phot/MeV)$	Decay Time (ns)	Emission max (nm)	Energy Resolution (% fwhm @ $662keV$)	Reference
BaF_2	SX	4.88	3,900-11,000	340-920	310	11.4	[29, 37, 44, 66]
BaF_2	CV	4.88	1,300-2,000	0.6-0.8	220		[13, 37, 44, 72]
$BiGe_3O_{12}\ (BGO)$	Bi^{3+}	7.13	7,100-10,600	300	460-510	9.05	[8, 63, 66]
$CaF2 : Eu$	Eu^{2+}	3.18	24,000				[29]
$CaWO_4$	CX	6.1	15,000-25,000	8,000	425	6.3-6.6	[47, 51, 81]
$CdS : In$	In^{3+}	4.8		0.2	520		[10]
$CdWO_4$	CX	7.9	7,800-15,800	5,000-20,000	480	8-8.8	[32, 44, 66]
CeF_3	Ce^{3+}	6.16	4,000	27	340	20	[48]
CsF	CV	4.1-4.64	1,900-2,000	2-4	390		[50]
$CsI : Na$	Na^{+}	4.51	38,000-49,000		425	7.4	[8, 29, 66]
$CsI : Tl$	Tl^{+}	4.51	55,000-61,000	980	530-560	5.7	[8, 24, 29, 53, 66]
$Gd_2SiO_5 : Ce\ (GSO)$	Ce^{3+}	6.71	2,800-21,500	56-600	430	7-9.2	[2, 45, 66]
$LaBr3 : Ce$	Ce^{3+}	5.1	61,000	30	356; 387	2.9	[74]
$LaCl3 : Ce$	Ce^{3+}	3.8	49,000	25	330; 352	3.1	[75]
$LiL : Eu$	Eu^{2+}	4.08	15,000	1,200	475	7.5	[54, 69]
$Lu_2SiO_5 : Ce\ (LSO)$	Ce^{3+}	7.4	22,200-33,000	40	420		[45]
$Lu_3Al_5O_{12} : Ce\ (LuAG)$	Ce^{3+}	6.7	5,606-12,500	10-70	500-510		[41, 43]
$Lu_3Al_5O_{12} : Pr$	Pr^{3+}	6.7	16,000-17,000	21-26	308; 310	4.6-5	[16, 17, 57, 60, 68]
$LuAlO3 : Ce\,(LuAP)$	Ce^{3+}	8.34	9,600-20,500	11-835	365; 390		[41, 49]
$LuI_3 : Ce$	Ce^{3+}	5.6	76,000	complex	474; 522; 540	3.3	[6, 23, 67]
$LuPO_4 : Ce$	Ce^{3+}	6.53	17,200	25	360		[40]
$NaI : Tl$	Tl^{+}	3.67	43,000-45,000		415	5.6-7.1	[29, 61, 66]
$PbWO_4$	CX	8.2	300	2.5-98	490		[11]
$Y_3Al_5O_{12} : Ce\ (YAG)$	Ce^{3+}	4.55	16,700	85-119	300; 550		[46, 53]
$YAlO3 : Ce\ (YAP)$	Ce^{3+}	5.35	15,900-21,600	24.2-27	347; 365		[3, 9, 41, 43]
$ZnO : Ga$	Ga^{3+}	5.7	0.36-0.82		385		[13, 39]

Table 1: Historically influential scintillators.

Background: Selected Compounds and Methods

Scintillator Candidate: Ce:LuAG

The first scintillator candidate compound investigated is cerium doped lutetium aluminum garnet (Ce:LuAG), molecular formula Ce:LuAG . The undoped lattice is shown in Figure 5.

Lutetium belongs to the lanthanide chemical element series which along with scandium and yttrium form what is referred to as the rare earth elements. The lanthanide series has four different types of electronic transitions with fourteen of these having the ability to adopt the 2+ and 3+ charge states. These can be integrated into numerous compounds where small discrepancies in the location of the lanthanide impurity state can dramatically effect scintillator performance.[17]

While several other scintillators also use cerium as a dopant, including cerium doped yttrium aluminum garnet (Ce:YAG), and cerium doped yttrium aluminium perovskite (Ce:YAP), Ce:LuAG has been used preferably because of its higher density.[18] This increased density results in more stopping power for like sized scintillators. This also allows the scintillator to be made relatively thinner, increasing spatial resolution. For this reason its application as a thin film has also been investigated. For a more detailed comparison of their properties reference Table 1.

These cerium doped scintillators benefit from the fast decay time of the 5d→4f radiative transition of the Ce^{3+} luminescent center and high quantum efficiency at RT.[19]

Ce:LuAG is a mechanically and chemically stable scintillation material that also has high hardness, high effective Z (62.9), short decay time, and high light yield. For these reasons it has found applications in HE physics and medical applications where its ability to detect x-ray and γ-ray emissions is utilized.[20] With an emission in the range of 500-550 nm it can be coupled with photodetectors. For this reason many future HE particle accelerators plan to employ these crystals as scintillators.

Several methods of crystal growth have used to create single crystals of this compound from a melt of oxide powders including the Czochralski (CZ), Bridgman (BD) and micro-pulling-down (μ-PD) method.

[17] P. Dorenbos. Electronic structure engineering of lanthanide activated materials. *Journal of Materials Chemistry*, 22(42):22344–22349, 2012

[18] Y. Zorenko, V. Gorbenko, I. Konstankevych, B. Grinev, and M. Globus. Scintillation properties of $Lu_3Al_5O_{12}$:Ce single-crystalline films. *Nuclear Instruments and Methods in Physics Research Section A: Accelerators, Spectrometers, Detectors and Associated Equipment*, 486(1-2):309 – 314, 2002

[19] S. Liu, X. Feng, M. Nikl, L. Wu, Z. Zhou, J. Li, H. Kou, Y. Zeng, Y. Shi, Y. Pan, and A. Setlur. Fabrication and Scintillation Performance of Nonstoichiometric LuAG:Ce Ceramics. *Journal of the American Ceramic Society*, 98(2):510 – 514, February 2015

[20] E. Auffray, D. Abler, S. Brunner, B. Frisch, A. Knapitsch, P. Lecoq, G. Mavromanolakis, O. Poppe, and A. Petrosyan. LuAG material for dual readout calorimetry at future high energy physics accelerators. *IEEE Nuclear Science Symposium Conference Record*, pages 2245–2249, 2009

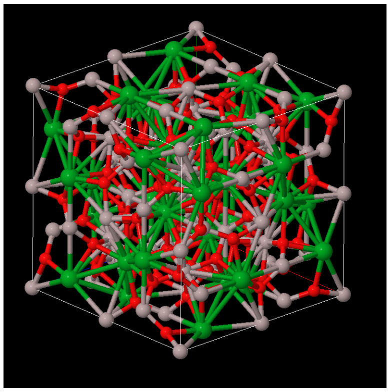

Figure 5: A cubic Ce:LuAG lattice structure with atomic positions of lutetium (green), aluminum (brown), and oxygen (red) taken from ICDD's PDF-4+ database, Crystal Structure Source: LPF.

Analysis of the Lu_2O_3-Al_2O_3 Phase Diagram

The Ce:LuAG compound belongs to the Lu_2O_3-Al_2O_3 phase diagram shown in Figure 6. It is also the most stable compound of those developed from the phase diagram and can be obtained from solid-state reaction. This is critically important and allows us to prepare the doped version of this material from synthesizing high purity powdered oxides where we can expect congruent melting at approximately 2060°*C*.

This phase diagram can be reference more generally as the Al_2O_3-RE_2O_3 system for rare earth elements. Each contains up to four intermediate compounds of alumina type that are stable only for the larger RE^{3+}, a garnet type (such as the Ce:LuAG investigated here), orthorhombic distorted perovskite type and monoclinic type that are of recent discovery.[21]

Single crystals can be made from many of these RE compounds finding applications as lasers and scintillators. These crystals also benefit from relatively easy doping with other activators of similar radii as the RE^{3+}.

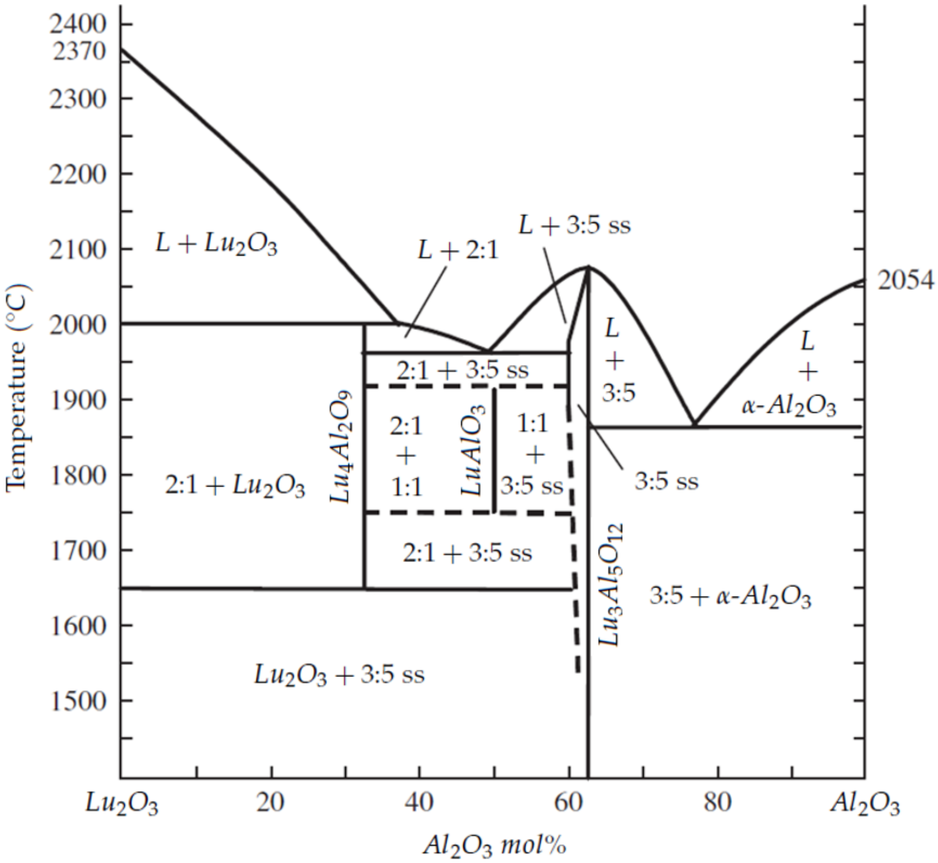

Figure 6: The Lu_2O_3-Al_2O_3 phase diagram.[62]

---

[21] D. Klimm. The melting behavior of lutetium aluminum perovskite $LuAlO_3$. *Journal of Crystal Growth*, 312:730–733, 2010

Scintillator Candidate: $MgTa_2O_6$

While several magnesium tantalates exist, the focus of this study will be on the alkaline earth tantalate $MgTa_2O_6$. The lattice structure of this compound is shown in Figure 7. This magnesium tantalate was selected because it had been proven stable in previous studies.[22]

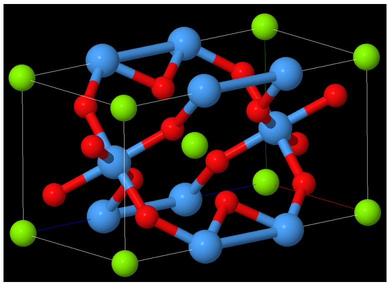

Figure 7: A tetragonal $MgTa_2O_6$ lattice structure with atomic positions of magnesium (green), tantalum (blue), and oxygen (red) taken from ICDD's PDF-4+ database.

The growing of $MgTa_2O_6$ crystals for scintillators is an exploratory study at this point with few examples of growth by any growth method with no known examples of μ-PD method growths. This tantalate has, however, been successfully grown using the floating zone (FZ) method.[23]

Other applications for this tantalate have been discovered for use as a dielectric resonator which has led to additional atomistic computer simulation research in an effort to better quantify its defect and possible dopant properties.[24]

Magnesium oxide (MgO), a constitutive compound of $MgTa_2O_6$ has found application as an easily prepared scintillator. Here, their relative insensitivity can be a benefit in some application because the light output does not saturate even under intense radiation. This scintillator has found application at the Michigan State University Cyclotron for beam focusing. They have also found additional applications in direct viewing of narrow beam images in the focal plane in magnetic spectrography, and as a phase measuring probe.[25]

Analysis of the MgO-Ta_2O_5 *Phase Diagram*

The $MgTa_2O_6$ compound belongs to the MgO-Ta_2O_5 phase diagram shown in Figure 8. From the phase diagram shown we can identify three stable compounds formed by the MgO-Ta_2O_5 system: $Mg_4Ta_2O_9$, $Mg_3Ta_2O_8$, and $MgTa_2O_6$. Both $Mg_4Ta_2O_9$ and $MgTa_2O_6$ have been studied and appear to be stable up to their melting points. The stability of $Mg_3Ta_2O_8$ is limited to the 1475-1675° C range. Pertinent melting temperatures are listed in Table 2. These temperatures will provide a useful reference when performing our μ-PD method experiments.

Compound	Melting Point (C)
Ta_2O_5	1872
MgO	2852
$MgTa_2O_6$	1775

Table 2: Constitutive compound melting temperatures in $MgTa_2O_6$.

---

[22] G. Halle and H. Mueller-Buschbaum. Investigations of Zn(1-x) M(x)Ta_2O_6 (M = Mg, and Ni) with a refinement of the crystal structure of $MgTa_2O_6$. *Journal of The Less-Common Metals*, 142:263–268, September 1988

[23] M. Higuchi, K. Ando, J. Takahashi, and K. Kodaira. Growth of $MgTa_2O_6$ single crystals by floating zone method and their optical properties. *Journal of the Ceramic Society of Japan*, 101(1):118–120, 1993

[24] C. Tealdi, M.S. Islam, L. Malavasi, and G. Flor. Defect and dopant properties of $MgTa_2O_6$. *Journal of Solid State Chemistry*, 177(11):4359–4367, 2004

[25] J.A. Nolen. An easily prepared scintillator for viewing accelerator beam spots. *Nuclear Instruments and Methods*, 156(3):595–596, November 1978

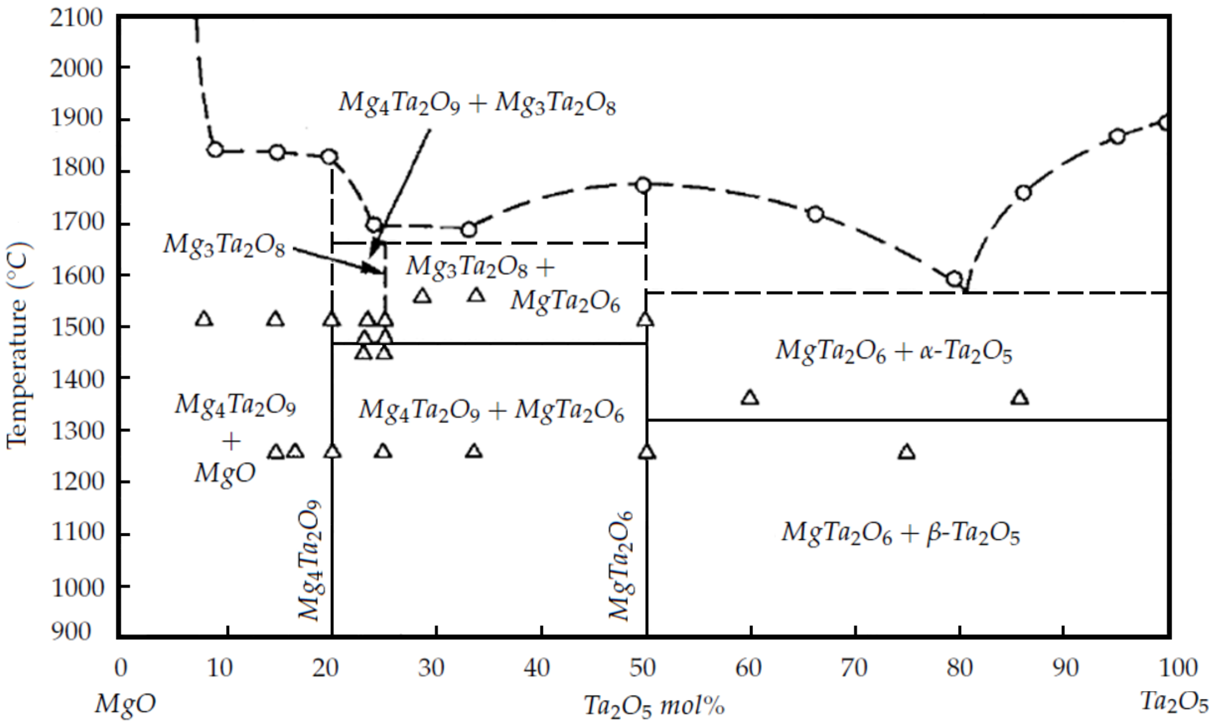

Figure 8: Preliminary phase diagram of the system MgO-Ta_2O_5.[4]

Powder Synthesis

Powder preparation and processing is critically important to the quality of the crystal growth. Constituent powder oxides were combined along molar ratios to produce powder samples of the desired compound.

It is critical that the powder components are high purity ($\geq$ 99.99%), approximately 100% phase purity, have high-specific surface area $\geq 5m^2g^{-1}$, and possess a median particle (agglomerate) size less than 3 μm, with no particles greater than 7 μm.[26]

The compounds tested in this study are limited to a single dopant or assumed to be self-activated. Additional precautions are typically needed when mixing dopants due to their small quantity relative to the other oxides, requiring molecular control of scintillation properties where dopants are essentially small percentage impurities. No sintering or hot-pressing was conducted on samples, however, these are options for further refining these powder compounds in future trails as they can further reduce sample contamination and improve densification.

The constitutive compounds must be mixed thoroughly in order to ensure that the combined sample will melt congruently in the crucible. Constituents were carefully weighed and in some instances mixed with high purity ethanol ($\geq$ 99.5%) and dried after thorough mixing with a mortar and pestle. Other samples were merely mixed thoroughly with a mortar and pestle. Samples were weighed on an analytical balance from Mettler Toledo.

In some instances samples were made more dense with a 12-ton force manual briquetting press from Chemplex. Between uses, the components of the press were cleaned in a VWR Model 50D ultrasonic cleaner to remove compacted powder from the housing and compression rod.

In other instances a hydraulic press was used to compress powder samples. These approaches are explicitly stated for each experiment conducted.

Figure 9: Mortar and pestle made from agate stone used to mix powder compounds.

[26] C. Greskovich and S. Duclos. Ceramic scintillators. *Annual Review of Materials Science*, 27(1):69–88, August 1997

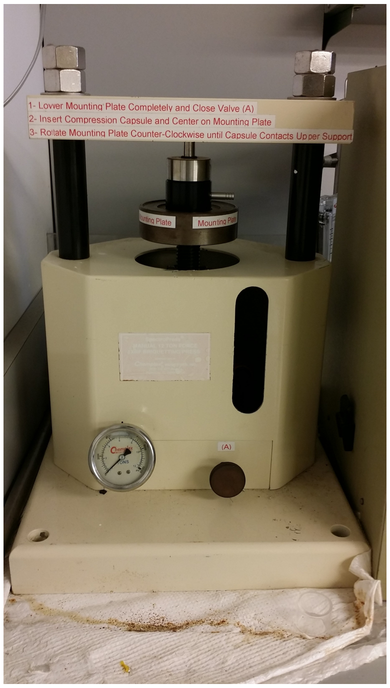

Figure 10: Densification was accomplished with a 12-ton force manual press.

Micro-Pulling-Down Method

The micro-pulling-down (μ-PD) method was used to conduct thin fiber crystal growths and is illustrated in Figure 11. The experimental setup utilizes induction heating from an electromagnetic coil to heat samples past their melting point. This coil encircles a crucible containing the compound to be formed into a crystal. This crucible is supported on an after-heater and surrounded by thermal insulation. The insulation is constructed from ceramics, typically high purity Al_2O_3. This is used to better control the temperature distribution surrounding the crucible. Additionally, the insulation saves RF power over the coarse of an experiment.

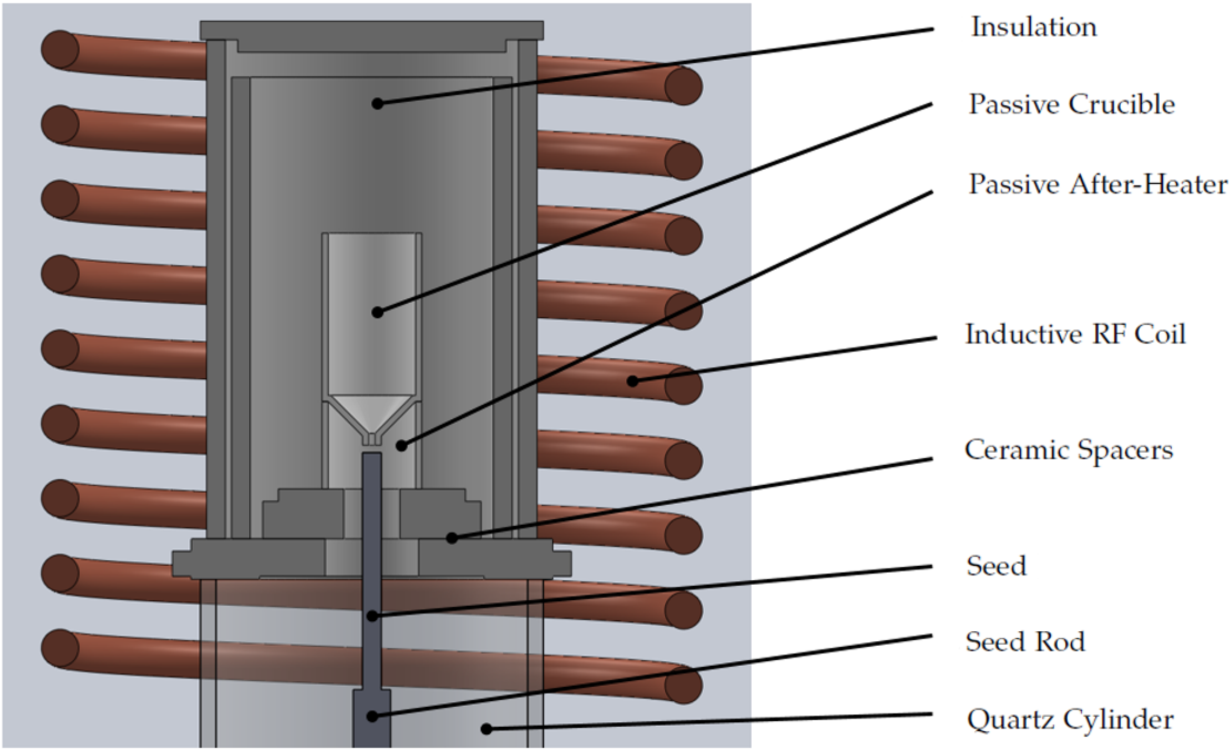

Figure 11: Schematic diagram of μ-PD system with external inductive RF heating.

The μ-PD method works by phase transformation from the liquid melt to a solid crystal. The composition of the melt is directly related to the composition of the produced crystal. It is assumed that when the melt is kept above the liquidus temperature, it homogenizes and further changes in its properties are prevented. The stability and homogenization of melt are influenced by the phase interfaces with the crucible, atmosphere, and crystal.[27]

The majority of growth techniques produce crystals by continuously transporting the seed and the as-grown crystal upwards away from the melt. This is the process used in Czochralski (CZ) and edge-defined-film-fed (EFG) among other applications that are

[27] T. Fukuda and V.I. Chani. *Shaped Crystals: Growth by Micro-Pulling-Down Technique*. Springer-Verlag, first edition, 2007

typically employed to grow commercially produced crystals. Benefits of these processes include better control of system vibrations and temperature fluctuations when compared to the μ-PD method, making these processes inherently more stable than pulling-down.

A major advantage of the μ-PD method over pulling-up applications, however, is that it dramatically reduces the probability of incorporating bubbles into the grown crystal which improves the quality of the grow. These bubbles are drawn to the surface of the melt by convection, away from the forming crystal. Consequently heavier solid particles are also more easily included in the as-grown crystal, such as dopants. This can be beneficial if the melt includes these particles but can also increase the odd of contamination from the crucible as any precipitated crucible material may be grown into the crystal because its relatively higher density when compared to the melt. Another advantage of the μ-PD method is that it has a higher utilization rate, decreasing production costs.[28]

Inductive Heating

The inductive coil heats the conductive crucible and after-heater via eddy currents. The after-heater heats the melt/crystal interface and also supports the rim of the crucible, holding it upright. While system heating may remain constant, its effect on the system is not. This variation is based off the amount of melt within the crucible compared to the amount solidified in the pulled crystal.

While several methods of heating are available for μ-PD chambers this study will focus on internal inductive RF heating. Other heating methodologies such as internal or external resistive heating have also been used. Both the crucible and after-heater are heated from an induction coil surrounding them. This coil is supplied with an AC current which generates a magnetic field that subsequently forms eddy currents (also called Foucault currents) in both the crucible and after-heater. These eddy currents act on these conducting components and transfer heat to the melt and growth interface.

The temperature gradient is critical for establishing the meniscus, across which the melt solidifies into a single crystal. This meniscus is the critical region of crystal growth and in-situ observation of the meniscus are done through a viewing window in the chamber which is aligned with holes drilled in both the insulation and after-heater. Crystal progress can also be measured by a sensitive load cell that weighs the forming crystal.[29]

Inductive heating can also be implemented externally whereby the surrounding cylindrical insulation is constructed of conductive materials, inducing secondary eddy currents separate from the primary eddy currents produced by the crucible and after-heater

[28] X. Xu, K. Lebbou, F. Moretti, K. Pauwels, P. Lecoq, E. Auffray, and C. Dujardin. Ce-doped LuAG single-crystal fibers grown from the melt for high-energy physics. *Acta Materialia*, 67:232–238, April 2014

[29] T. Fukuda and V.I. Chani. *Shaped Crystals: Growth by Micro-Pulling-Down Technique*. Springer-Verlag, first edition, 2007

to heat the melt. These eddy currents are less efficient due to their greater distance from the melt and increase the cost of production.

Crucible and After-Heater

For the purposes of this analysis we will assume that the crucible and after-heater are comprised of the same materials, which is beneficial for high temperature thermal expansion. The selection of this material is critically important to the success of the experiment and its repeatability. The crucible typically has a conical bottom and grow crystals in the μ-PD method in diameters of a few millimeters.

The first requirement of a crucible/after-heater material is that it must have an appreciably larger melting temperature than the melt contained within. Decomposition of the crucible into the melt even in small amounts has extremely detrimental effects on crystal quality and seeding characteristics.

Additionally the mechanical performance of the crucible/after-heater pair is important as they must retain their geometry between RT and high temperatures. Mechanical properties are important at RT where it is fabricated into the desired geometry.

Chemical compatibility must also be established between the crucible, the melt and the surrounding atmosphere. Compatibility also extends to the solvents used to clean them of remaining melt after the experiments are complete. The wetting properties of the melt along the exterior and interior surfaces of the crucible must also be considered.

If the wetting properties are too strong, the melt will adhere aggressively to the exterior of the crucible after it has exited the crucible nozzle rather than seeding correctly. If the wetting properties are too weak the melt will have difficulty traveling down the capillary channel.

Crucible and after-heater materials are often made of pure metals due to diffusion concerns but some compounds have also been implemented. Table 3 shows a list of commonly used crucible materials along with melting temperatures and growth atmospheres.

The crucible nozzle also determines the shape of the subsequent crystal growth. Currently the μ-PD method is primarily limited to cylindrical or rectangular crystal growths as more complex geometries are difficult to machine given the material constraints of the crucible.

Melt

Convection plays an important role at the melt/crystal interface. The main crucible reservoir containing the melt is stirred effec-

Material	Melting Point (°C)	Growth Atmosphere	Reference
C (dense graphite)	3500	Ar, Ar+CF	[80]
Re	3180	Ar+H_2 (3-4%)	[52]
Mo	2617	Ar, Ar+H_2 (2%)	[36]
Ir	2410	Ar, N_2, N_2+O_2 (1%)	[59]
Al_2O_3	2054	Air	[20]
Rh	1966		[20]
Pt	1772	Air, Ar+CF,	[20]
SiO_2	1600		[20]
Au	1064		[20]
Al	660		[34]
Ir+2%Re		Ar	[30]

Table 3: Common μ-PD crucible and after-heater materials, melting temperatures, and growth atmospheres.

tively by thermo-capillary convection. The capillary channel is governed by diffusive Poiseuille flow and the meniscus is subjected to Marangoni convection.[30]

Melt flow in the molten zone is largely the result of Marangoni convection. This convection effects how the steady state of the system is evaluated as the Marangoni velocity is larger than the growth rates, playing an influential role when modeling the μ-PD method computationally.[31]

The melt is further influenced by temperature gradients produced by the induction coil. Numerical studies have been conducted to model these gradients in order to better understand system response.[32]

Another consideration when evaluating the melt flow is segregation at the end of the capillary channel. Single crystals are formed by short distance displacement of particles in the liquid phase and re-ordering in the solid crystal. This ordering process takes place within the meniscus region that occurs between the liquidus melt and the solid crystal. This re-ordering process is made easier when the composition of the melt and crystal are the same. Since this is generally the case in the μ-PD method, relatively fast pull-down rates can be used when compared against other pulling-up methods.

Diameter Control

Diameter control continues to be an area of improvement for the relatively new μ-PD method. This is still primarily done through direct visual examination of the growth process. The growth parameters such as pulling-down rate and chamber temperature are adjusted manually based on these observations. Some automation does exist that uses vision software to relay the appropriate adjustment but these system responses are determined first by observations of meniscus stability.

In addition, sensitive load cells can be used to adjust growth parameters based on the current weight and pull-down distance of

---

[30] B.M. Epelbaum, G. Schierning, and A. Winnacker. Modification of the micro-pulling-down method for high-temperature solution growth of miniature bulk crystals. *Journal of Crystal Growth*, 275(1):867–870, December 2005

[31] T. Fukuda, P. Rudolph, and S. Uda. *Fiber Crystal Growth from the Melt*, volume 6. Springer Berlin Heidelberg, 2004

[32] H.S. Fang, Z.W. Yan, and E.D. Bourret-Courchesne. Numerical study of the micro-pulling-down process for sapphire fiber crystal growth. *Crystal Growth & Design*, 11(1):121–129, 2011

the grown crystal. This second method is less practical as the small diameters of the crystal imply an extremely light weight, requiring a very precise load cell that increases production costs.[33]

Growth Chamber

The growth chamber used for μ-PD is important in establishing the appropriate environment and allowing the operator to evaluate the process. This is especially critical when temperatures need to be adjusted dynamically to compensate for reduction in melt volume. The viewing window is traditionally comprised of CaF_2 which is transparent and can tolerate high temperatures.

X-ray Powder Diffraction

X-ray powder diffraction (XRPD) is a technique employed to analyze fine powder samples. This technique is based off the repeating structure of atoms in a solid material. It is also dependent on the wavelength of x-rays used and the spacing between layers of atoms in the repeating structure to be similar. These repeating structures of atoms are capable of scattering the incoming x-rays. From these x-rays, energy peaks develop in magnitude proportional to the frequency of each lattice plane of the crystal. The size and position of the set of peaks is characteristic of the crystal structure and chemical composition.

X-rays are used because they have high energies and short wavelengths on the order of the atomic spacing of the solids being investigated.

The diffracted x-ray beam is composed of a large number of scattered waves that constructively and destructively interfere with each other. Other phase relationships are a combination of these effects. Together these effects form an x-ray diffraction pattern.

The distance between these parallel lattice planes is defined as, d. Bragg's Law develops a relationship between x-ray wavelength and the d-spacing between lattice planes. This law can be expressed as,

$$n\lambda = 2d\sin\theta \tag{5}$$

where n is a whole number, typically one, λ is the wavelength of x-ray, which is operator defined and θ is the angle between the direction of incoming x-rays and the lattice plane.

XRPD essentially solves this equation for the unknown value of d. Diffraction energies are low when the angle is different for each adjacent crystal plane and is not a whole length. This is due to the emitted wave being out of phase. Consequently if the emitted waves are a whole wavelength then the waves will reinforce each other and produce an energy peak.

[33] T. Fukuda and V.I. Chani. *Shaped Crystals: Growth by Micro-Pulling-Down Technique*. Springer-Verlag, first edition, 2007

A recorder plots the diffracted beam intensity as a function of 2θ. This is called the diffraction angle. This constructed plot displays high-intensity peaks that satisfy the Bragg diffraction condition.

X-ray Luminescence

X-ray luminescence (XRL) testing is used to determine the emission spectra of scintillation crystals. The emission spectra is typically an output of relative intensities over a range of wavelengths. The maximum of this emission curve is considered the peak of the emission band.[34]

Each scintillator has a characteristic emission spectrum that is correlated to the type scintillator mechanism dominant in the material. Knowing the emission spectrum of a particular material is important because it can determine if the emission is in the visible or near-visible range. Also by knowing the specific wavelengths of emission from the scintillator it can then be coupled with an appropriate PMT.

Scanning Electron Microscopy

Scanning electron microscopy (SEM) utilizes a scanning electron microscope that produces images of a sample by scanning in a rastering pattern with a focused beam of electrons. In order to prevent an insulator sample from charging, a thin metal coating is often applied. A more complicated morphology would require thicker coating in order to maintain its continuity.

Another method to prevent charging in a sample is to observe the sample under low accelerating-voltage. Fundamentally, charging occurs in a sample when the electrons entering the sample are different from those exiting. The sample can also be viewed at a tilt, where the electron beam enters a sample obliquely. This methodology is employed when a specimen has less surface irregularities. A non-conductive sample can also be observed under low vacuum. Low-vacuum scanning electron microscopy (LVSEM) ionizes the residual gas molecules, however, this process typically involves pressurizing the chamber.

Energy-Dispersive X-ray Spectroscopy

Energy-dispersive x-ray spectroscopy (EDS) testing utilizes the photoelectric effect to produce a spectrum of counts that can identify elements within a compound. The photoelectric effect is shown in Figure 12. The basic physical process can be described

---

[34] G. Blasse and B.C. Grabmaier. *Luminescent Materials*. Springer-Berlin Heidelberg, first edition, 1994

within the Einstein equation,

$$E_{\mathrm{B}} = hv - E_{\mathrm{K}} \tag{6}$$

where E_{B} is the binding energy, hv is the energy of the x-ray source, which is operator defined, and E_{K} is the kinetic energy of the emitted electron that is then measured by the EDS detector.

This analysis detects elements that are present in the outer 10 nm of the sample. In the case of coated samples the coating may contribute a disproportionately large percentage of the material's identity. The impact of this can be reduced by coating the samples with an element that is not expected to be found with the compound of interest.

For data output, the area underneath the detected peaks is related to the amount of each element present. Percentages of each element present are typically calculated with the expression,

$$I_{ij} = K \cdot T\left(E_{\mathrm{K}}\right) L_{ij}\left(\gamma\right) \sigma_{ij} \int n_i\left(z\right) e^{-z/\lambda\left(E_{\mathrm{K}}\right)\cos\theta} dz \tag{7}$$

where I_{ij} is the area of peak j from element i, K is an instrument constant, $T\left(E_{\mathrm{K}}\right)$ is the transmission function of the analyzer, $L_{ij}\left(\gamma\right)$ is the angular asymmetry factor for orbital j of element i, σ_{ij} is the photoionization cross-section of peak j from element i, $n_i\left(z\right)$ is the concentration of element i at a distance z below the surface, $\lambda\left(E_{\mathrm{K}}\right)$ is the inelastic mean free path length, and θ is the take-off angle of the photoelectrons measured with respect to the surface normal. X-ray flux, area of the irradiated sample and the solid angle of the photoelectrons accepted by the apparatus are contained with the instrument constant K.

From this equation it is also important to note that if a sample is a single crystal, the outgoing electrons can have peak intensities that deviate from the predicted values. This is critically important in our evaluations as it is assumed that we are evaluating single crystals.[35]

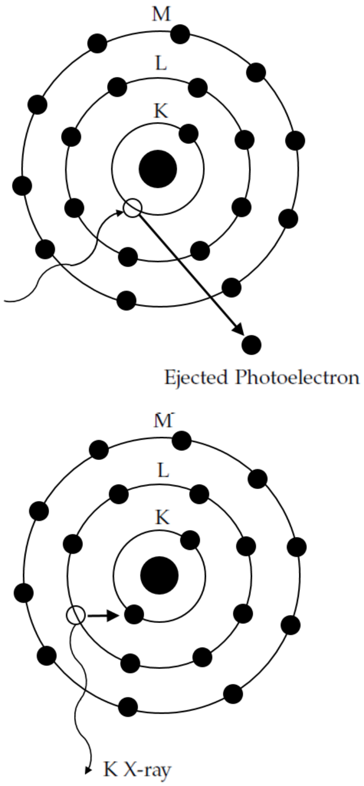

Figure 12: Sequential images of photoelectric effect with photon absorption and photoelectron ejection (top) followed by fluorescent x-ray emission (bottom).

[35] B.D. Ratner and D.G. Castner. *Electron Spectroscopy for Chemical Analysis*, pages 47 – 112. John Wiley and Sons, Ltd, 2009

Experimental Procedures

Powder Synthesis: Ce:LuAG

Lutetium Oxide (Lu_2O_3), aluminum oxide (Al_2O_3), and cerium (IV) oxide (CeO_2) were synthesized to produce $Lu_3Al_5O_{12}$:Ce (Ce:LuAG) as detailed in Table 4.[36] Powdered oxides were purchased from Sigma-Aldrich.

Compound	Mole ratio	Density $\left(\frac{g}{cm^3}\right)$	Mass (mg)	% Purity
Lu_2O_3	0.365	9.42	6894	99.99
Al_2O_3	0.625	3.95	3025	99.997
CeO_2	0.010	7.65	82	99.995
$Lu_3Al_5O_{12}$:Ce	1	6.681	10000	

Table 4: Compound mixture for ten gram sample of Ce:LuAG .

Hydraulically Pressed: Sample 1

The first sample prepared was a hydraulically-pressed (HP) 10 gram powder synthesis. This sample was prepared prior to the beginning of study.

Manually Pressed: Sample 2

The second sample prepared was a manually-pressed (MP) 5 gram powder synthesis. The powder synthesis procedure is detailed below,

1. The three constitutive compounds were weighed on an analytical balance and mixed with a mortar and pestle.
2. Ethanol ($\geq$ 99.5%) was added and the compounds were mixed until the ethanol had evaporated from thorough use of mortar and pestle.
3. The sample was pressed at 6000 psi for 5 minutes. Once removed the sample was inspected for any signs of contamination prior to loading into the crucible for μ-PD experiments.

---

[36] N.G. Nause. Powder x-ray diffraction data for rare earth garnets. Master's thesis, Stephen F. Austin State University, 2003

Powder Synthesis: $MgTa_2O_6$

Magnesium oxide (MgO) and tantalum pentoxide (Ta_2O_5) were mixed at 50/50 mol% to produce $MgTa_2O_6$ as detailed in Table 5. Powdered oxides were purchased from Sigma-Aldrich.

Compound	Mole ratio	Density $\left(\frac{g}{cm^3}\right)$	Mass (mg)	% Purity
Ta_2O_5	0.500	8.2	4582	99.99
MgO	0.500	3.58	418	99.999
$MgTa_2O_6$	1	7.57	5000	

Table 5: Compound mixture for five gram sample of $MgTa_2O_6$.

Loose Powder: Sample 1

The first sample prepared was simply mixed together with a mortar and pestle and not densified in any manner. Powder compounds were measured on an analytical balance and loaded into the crucible in preparation for μ-PD experiments.

Manually Pressed: Sample 2

A five gram sample of $MgTa_2O_6$ was prepared from Ta_2O_5 and MgO compounds as outlined above. The powder synthesis procedure is detailed below,

1. Both powder compounds were weighed out on an analytical balance and mixed together with a mortar and pestle.
2. Both powder compounds were very similar in appearance, both chalky white, because of this it was more difficult to determine when the two compounds had been thoroughly mixed.
3. To better ensure proper mixing, the two compounds were mixed with ethanol ($\geq$ 99.5%). The wetted sample was then mixed thoroughly until the ethanol had evaporated out.
4. The sample was then compressed in the 12 ton manual press at 4000 PSI for 3 minutes. Under pressure, a portion of the sample spilled from the top of the press. It was discovered that the ethanol had not completely dried and sample was lost as it bubbled out.
5. The apparatus was cleaned and the sample was repacked and pressed again at 5000 PSI for 5 minutes.
6. The sample was weighed after compressing, measuring 3982 mg down from the original 5000 mg (20.36% loss).

It was determined that the sample must be remade over concerns that we may have lost the tantalate stoichiometry. The sample prepared is shown in Figure 13.

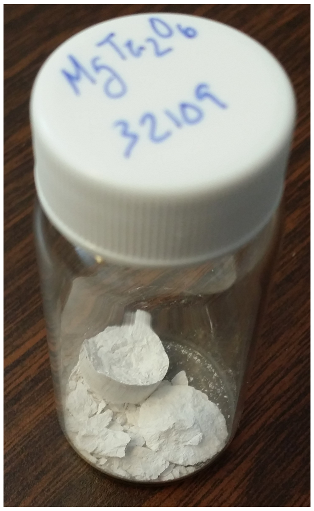

Figure 13: Pressed sample of $MgTa_2O_6$, single press attempt with significant loss in process.

Manually Pressed: Sample 3

A second five gram sample was prepared. The powder synthesis procedure is detailed below,

1. Both powder compounds were weighed out on an analytical balance and mixed with a mortar and pestle.

2. Ethanol ($\geq$ 99.5%) was added and the compounds were mixed until the ethanol had evaporated. The wait time for this process was increased and the amount of ethanol used decreased. This was in an effort to prevent another spill of compound at the press.

3. The sample was divided in half and pressed at 8000 PSI for 5 minutes.

The sample was made slightly larger at 5250 mg and came out to 4977 mg (5.19% loss). The sample prepared is shown in Figure 14.

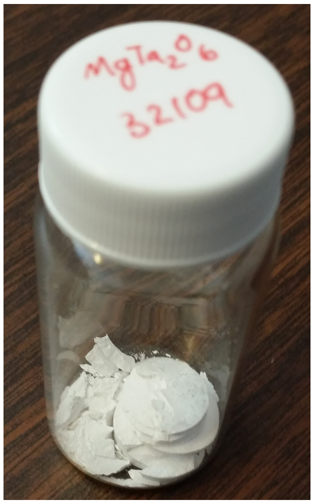

Figure 14: Pressed sample of $MgTa_2O_6$, two different presses were used to break the sample into a more manageable size.

Manually Pressed: Sample 4

A ten gram sample was prepared for testing. Sample was cold-pressed into four separate samples. The powder synthesis procedure is detailed below,

1. Both powder compounds were weighed on an analytical balance and mixed with a mortar and pestle.

2. Ethanol ($\geq$ 99.5%) was added and the compounds were mixed until the ethanol had evaporated. The wait time for this process was increased and the amount of ethanol used decreased. This was an effort to prevent another spill of compound at the press.

3. The sample was divided into fourths and pressed at 8000 psi for 5 minutes. Once the sample was removed, contamination from the press was observed on the perimeter of the sample.

4. Attempts were made to remove this contamination with MgO powder but were unsuccessful.

5. A razor blade was used to remove the contamination from the pellet surface. This dramatically improved the quality of the sample but sacrificed a small portion of the sample.

The sample was weighed after pressing with losses of approximately 5%.

Micro-Pulling-Down Method

The μ-PD test chamber used was constructed by Cyberstar and is shown in Figure 17. The chamber is cooled continuously with a water chiller loop through the chamber walls. In-situ adjustments can be made to the seed rod in the x and y directions. Mitutoyo micrometer heads are used to translate the seed rod with 0.01 mm accuracy markings. Vertical travel could be adjusted manually or could be programmed at a constant rate as shown in Figure 15. The chamber possesses a nine coil induction heater that can heat samples up to approximately 2300°C.

The chamber could also be evacuated and filled with a reducing atmosphere. For our experiments, the reducing atmosphere was argon. This prevented components, specifically the crucible and after-heater, from oxidizing at our ultra-high experimental temperatures. The chamber was connected to a reservoir of argon that was circulated continuously before and during our experiments. This circulation was adjusted with a pair of Key Instruments glass tube flow meters that regulate input and output flow.

A Sylvac indicator is used to measure the vertical translation distance so the crystal can be measured in process. The test chamber also possessed four viewing windows, one of which was equipped with a Sony XCD-SX90 FireWire camera that streamed images to a nearby PC for monitoring at a rate of up to 30 FPS. This camera was aligned to view the crucible nozzle through small holes drilled into the insulators and after-heater.

Double ceramic insulation, made of high purity Al_2O_3, was used for the Ce:LuAG samples due to its higher melting point. A single layer of insulation was used for the $MgTa_2O_6$ experiments. The cylindrical ceramic spacers and lid needed to be cut in half due to thermal expansion during testing. If not separated the components were prone to fracturing under the intense experimental temperatures. An example of these fractures from thermal expansion is shown in Figure 16. Viewing ports were drilled into the ceramic insulator with a diamond tipped bit. This operation was performed at a Dremel workstation that acted as a drill press for this purpose.

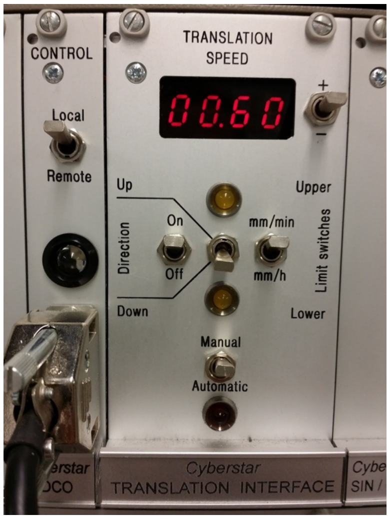

Figure 15: Translation speed controls with local (programmed) and remote (user) adjustment.

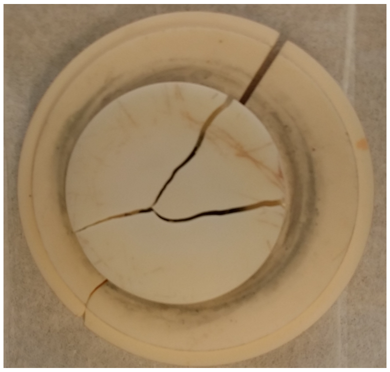

Figure 16: Fractured ceramic insulator cap removed from chamber after high temperature cycling.

Chamber Temperature Curve

A pryometer was used to approximate the temperature at the crucible nozzle. The chamber temperature is adjusted by set-point (SP) on the connected PC. Argon was circulated for an hour prior to the temperature curve being constructed.

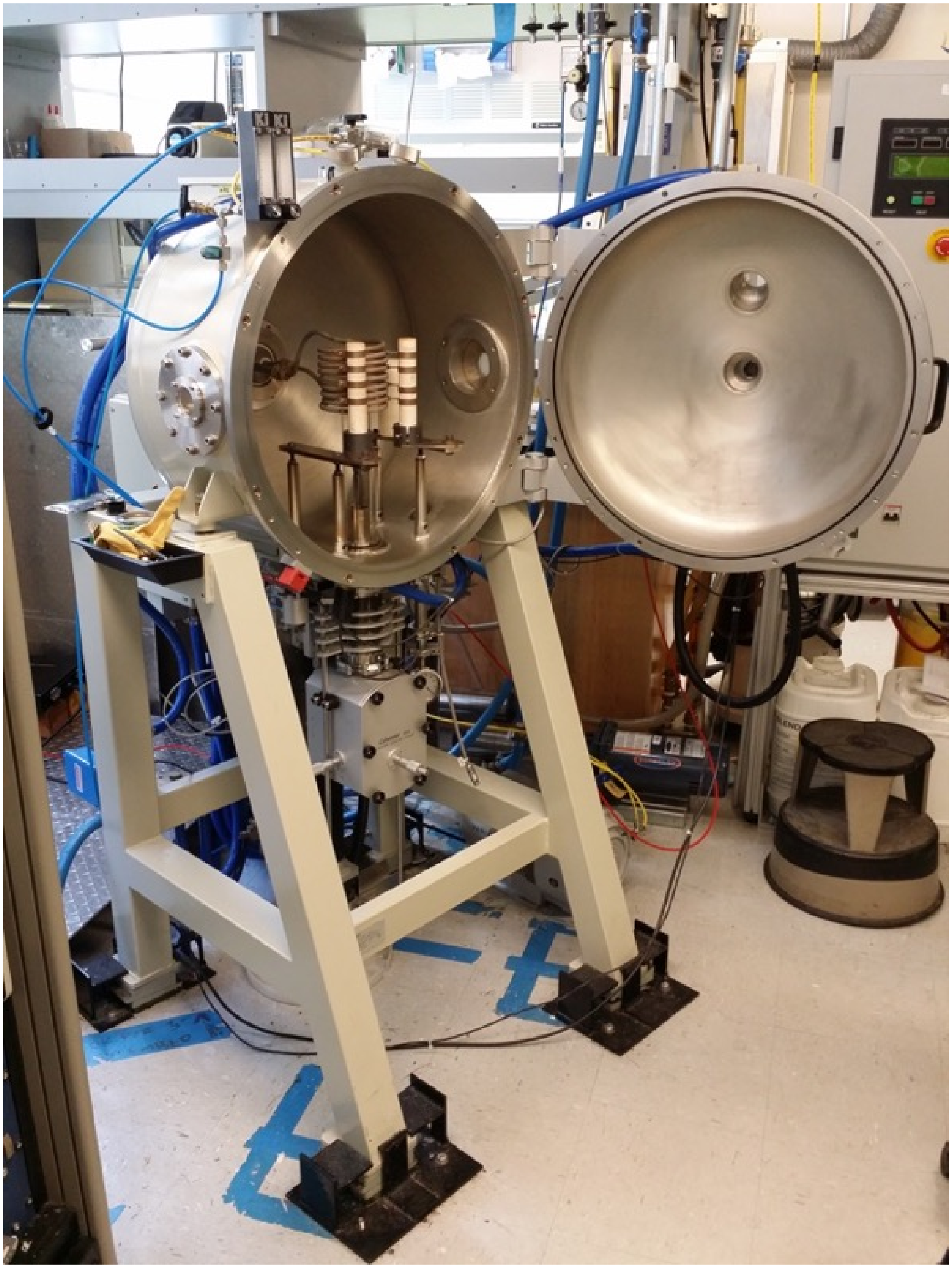

Figure 17: The water-cooled μ-PD test chamber from Cyberstar.

Temperatures were measured with a Marathon MM2MH pyrometer from Raytek with a temperature range of 450-2250°C, spectral response of 1.6 μm and a response time (95% response) of 2 ms. This non-contact IR real-time temperature monitor was used in conjunction with the Raytek DataTemp Multidrop software to evaluate temperature stability for a given SP. The temperature curve collected is shown in Figure 19.

Figure 18: Marathon MM2MH pyrometer.

Offsetting for RT, we are able to approximate this curve accurately for high temperature readings. We can also offset this curve with knowledge that the Ce:LuAG compound has a melting temperature of 2000°C. Melting was achieved at a set-point of 47. The governing SP to temperature relation can be approximated with the expression,

$$\text{temperature} = f(SP) = 1742\,(SP)^{0.1287} - 859 \tag{8}$$

which has an R-squared value of 0.9999.

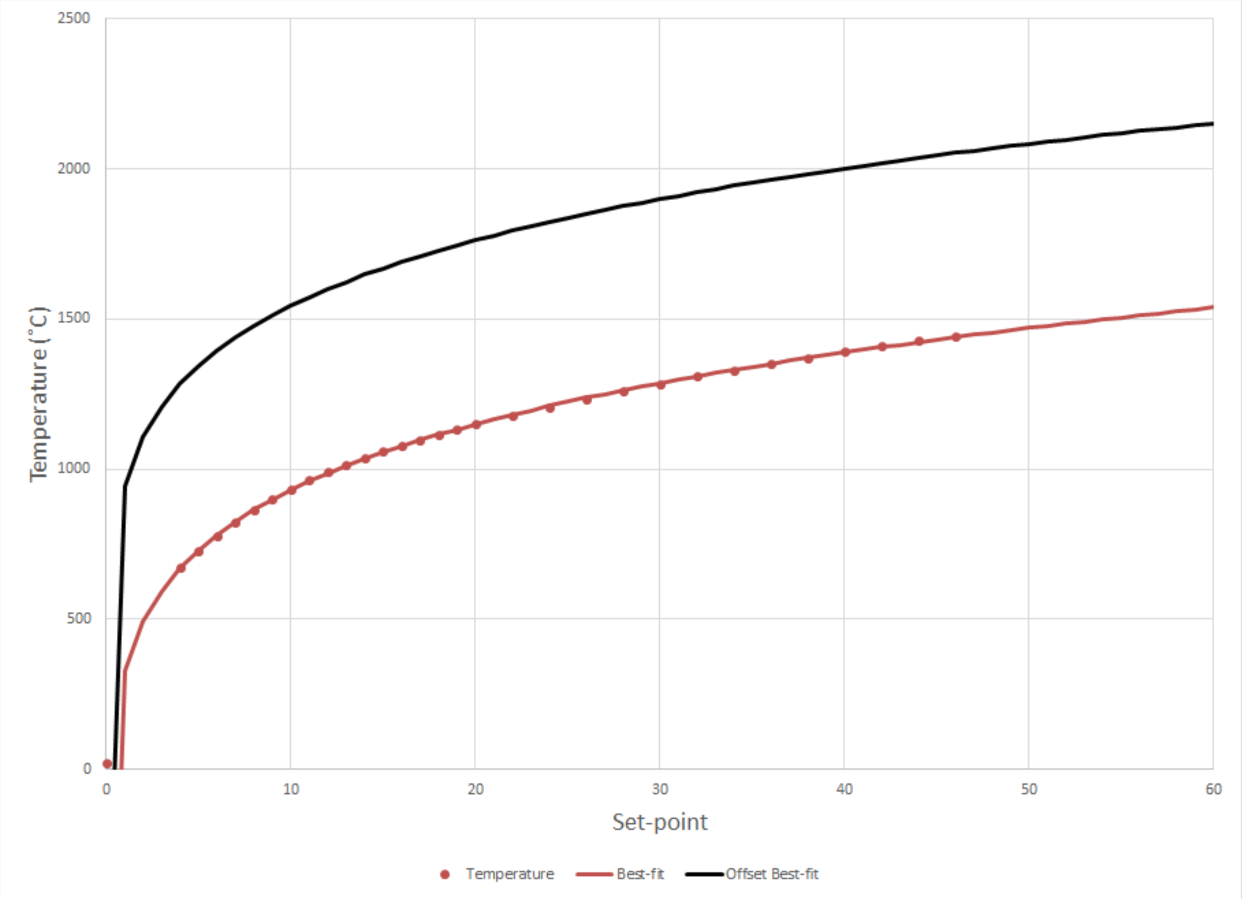

Figure 19: Set-point to temperature calibration curve for double insulated μ-PD experiments at the crucible nozzle.

Software Development

The camera software was capable of saving screenshots and videos for a specific number of frames, however saving these formats during an experiment was found to be prohibitively time consuming. This functionality was greatly improved with software improvements I implemented over the course of the experiments performed.

A Microsoft Windows application was written in VB that streamlined image captures to a single button click. The source code was written in Visual Studio which is an IDE from Microsoft.

Secondary scripts were written in Python to crop and append text to each image, detailing the experimental parameters. The source code was written in IDLE for Python. A sample output from these scripts is shown in Figure 22.

Lastly these images were sequenced and converted into a video file for better presentation. These video files are self contained as each includes the crystal type, time stamp (HH:MM:SS), specific image of total image sequence, production site, date and temperature.

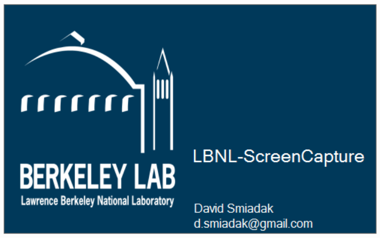

Figure 20: Application splash screen.

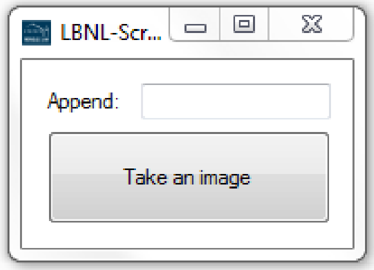

Figure 21: Image capture application written for Windows.

Crystal Synthesis: Ce:LuAG

Double ceramic insulation was used because of the high melting temperature. The Ce:LuAG has a cubic structure and good iridium compatibility with a melting temperature of approximately 2060°C, which is approaching the melting temperature of iridium at 2447°C. Pull rates for this compound have been successful between 0.32-0.75 for CZ growth and 0.25-0.75 mm/min for μ-PD.[37]

Hydraulically Pressed Sample 1, Trial 1

A μ-PD technique crystal growth attempt was conducted. The crucible used had a 1 mm OD capillary nozzle. The μ-PD experimental procedure is described below,

1. Chamber was evacuated to a vacuum of -25 PSI. Argon was then pumped in, to a pressure of +7 PSI, and left circulating for 1 hour prior to initializing the heating profile.

2. Temperature was increased from RT to 2044°C (SP: 45) over 2.75 hours.

   No appreciable change observed.

3. Temperature was increased to 2060°C (SP: 47) and the seed was left in contact.

   Crystal seeded and was pulled down at a rate of 0.60 $\frac{\text{mm}}{\text{min}}$.

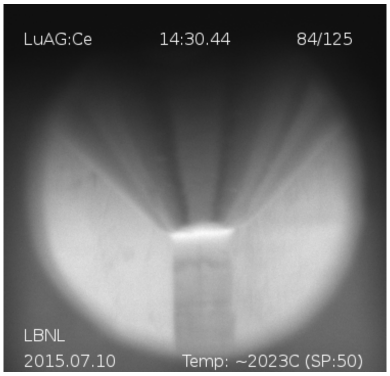

Figure 22: Sample output of a formatted single frame.

---

[37] X. Xu, K. Lebbou, F. Moretti, K. Pauwels, P. Lecoq, E. Auffray, and C. Dujardin. Ce-doped LuAG single-crystal fibers grown from the melt for high-energy physics. *Acta Materialia*, 67:232–238, April 2014

4. After a period of growth it was noted that the melt was slanted and was moving back and forth side-to-side more than expected. The Ce:LuAG crystal no longer seemed to be growing downwards at a constant rate and it was determined that the Ce:LuAG crystal had broken somewhere out of view.
5. Chamber was cooled to RT in 1 hour.

Hydraulically Pressed Sample 1, Trial 2

It was determined that the Ce:LuAG crystal grown previously was too small a sample to perform OE testing. In order to increase this quantity another growth attempt was scheduled. The μ-PD experimental procedure is described below,

1. Chamber was evacuated to a vacuum of -25 PSI. Argon was then pumped in, to a pressure of +7 PSI, and left circulating for 1 hour prior to initializing the heating profile.
2. Temperature was increased from RT to 2044°C (SP: 45) over 2 hours.

   No appreciable change observed.
3. Temperature was increased incrementally to 2068°C (SP: 48) and the seed was left in contact after the melt was observed emerging from the crucible nozzle.

   Crystal seeded and was pulled down at a rate of 0.50 $\frac{\text{mm}}{\text{min}}$.
4. Chamber was cooled to RT in 1 hour.

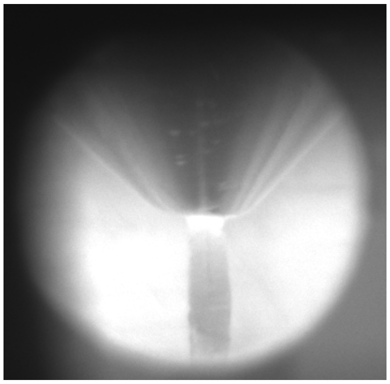

Figure 23: Continuous but uneven Ce:LuAG crystal growth (Sample 1, Trial 2).

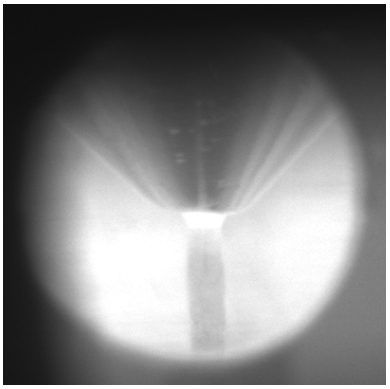

Figure 24: Ce:LuAG crystal growth with large molten region between the crucible and ordered crystal (Sample 1, Trial 2).

Hydraulically Pressed Sample 1, Trial 3

The focus of this growth was to produce a larger and more consistent Ce:LuAG crystal. While the previous attempt was relatively long, it had a significant amount of diameter variability and was overall slightly undersized for the 1 mm diameter capillary opening. The μ-PD experimental procedure is described below,

1. Chamber was evacuated to a vacuum of -25 PSI. Argon was then pumped in, to a pressure of +7 PSI, and left circulating for 1 hour prior to initializing the heating profile.
2. Temperature was increased from RT to 2044°C (SP: 45) over 2 hours.

   No appreciable change observed.
3. Temperature was increased incrementally to 2068°C (SP: 48) and the seed was left in contact after the melt was observed emerging from the crucible nozzle.

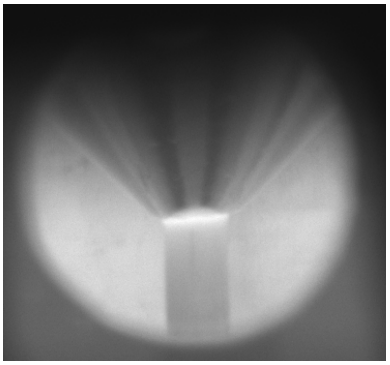

Figure 25: Smooth and stable Ce:LuAG crystal growth (Sample 1, Trail 3).

4. Crystal seeding failed shortly after start.
5. Seed left in contact with the melt for 30 minutes.
6. Crystal seeding failed shortly after start.
7. Temperature was increased to 2076°C (SP: 49) and the seed was left in contact for 30 minutes.
8. Crystal seeding failed shortly after start.
9. Temperature was increased incrementally to 2083°C (SP: 50) and seed was left in contact for 30 minutes.
10. Pulling-down rate was decreased to 0.10 $\frac{\text{mm}}{\text{min}}$.
11. Crystal seeded and was pulled down at reduced speed and increased temperature compared to last growth attempt from this same melt.
12. Chamber was cooled to RT in 1 hour.

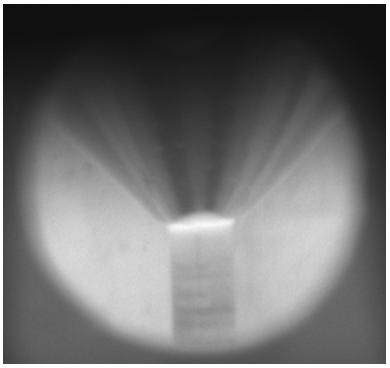

Figure 26: Ce:LuAG crystal growth with horizontal line defects visible (Sample 1, Trail 3).

Hydraulically Pressed Sample 1, Trial 4

The focus of this growth was to produce a crystal with a similar diameter and consistency of the crystal grown in Trial 3. This test is expected to grow overnight due to the slow anticipated growth rate of 0.1 $\frac{\text{mm}}{\text{min}}$. The μ-PD experimental procedure is described below,

1. Chamber was evacuated to a vacuum of -25 PSI. Argon was then pumped in, to a pressure of +7 PSI, and left circulating for 1 hour prior to initializing the heating profile.
2. Temperature was increased from RT to 2044°C (SP: 45) over 2 hours. No appreciable change observed.
3. Temperature was increased incrementally to 2083°C (SP: 50) and the seed was left in contact after the melt was observed emerging from the crucible nozzle.
4. Crystal seeding failed shortly after start.
5. Seed left in contact with the melt for 30 minutes.
6. Crystal seeding was successful but detached from the seed after approximately 1 mm as shown in Figure 27.
7. Temperature was increased to 2098°C (SP: 52) and the melt pulled back into the capillary.
8. Seed left in contact with the melt for 90 minutes at 2090°C (SP: 51).

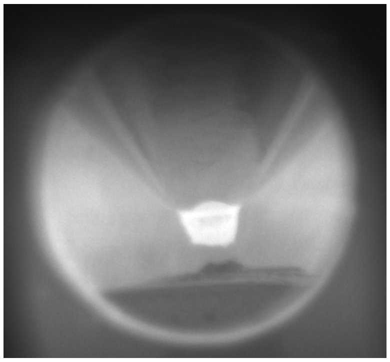

Figure 27: Ce:LuAG growth failure shortly after successful seeding. With an abrupt temperature increase the melt pulled back into the capillary channel (Sample 1, Trial 4).

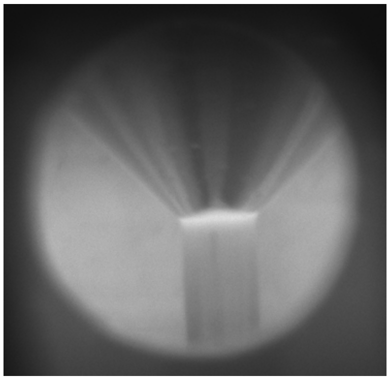

Figure 28: Stable $Ce{:}LuAG$ crystal growth (Sample 1, Trial 4).

9. Temperature reduced to 2083°C (SP: 50) and crystal was successfully seeded as shown in Figure **??**.

10. Chamber was programmed for 14.5 hours at a pull-down rate of 0.1 $\frac{\text{mm}}{\text{min}}$.

11. Chamber was cooled to RT in 1 hour.

Manually Pressed Sample 2, Trial 1

The focus of this growth was to produce a crystal using a wider capillary channel in an effort to grow a larger diameter Ce:LuAG crystal. The μ-PD experimental procedure is described below,

1. Chamber was evacuated to a vacuum of -25 PSI. Argon was then pumped in, to a pressure of +7 PSI, and left circulating for 1 hour prior to initializing the heating profile.

2. Temperature was increased from RT to 2044°C (SP: 45) over 2 hours.

   No appreciable change observed.

3. Temperature was increased incrementally to 2083°C (SP: 50) at a rate of 1 SP every 3 minutes.

   No appreciable change observed.

4. Temperature was left at 2083°C (SP: 50) for 30 minutes.

5. Crystal seeding failed and temperature increased incrementally to 2098°C (SP: 52) where it was then held for 60 minutes. Slight melt show was visible from the end of the capillary channel.

6. Seed was left in contact for 10 minutes then pulled down after the melt was observed spreading across seed interface.

7. Crystal seeding was successful and was pulled at a slower rate of 4 $\frac{\text{mm}}{\text{hr}}$. After approximately 20 minutes there was no discernible retraction of the seed. Retraction was switched over to manual and it was discovered that the seed rod was not sufficiently clamped and now stuck to the melt as shown in Figure 29.

   Efforts were made to try and release the melt but were unsuccessful. The vertical motion of the seed holder could be observed from the viewing window along with the now stationary rod.

8. Chamber was cooled to RT in 2 hours.

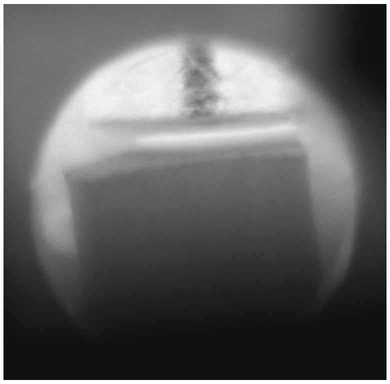

Figure 29: The Ce:LuAG melt attached to the seed, pulling it from the seed rod holder below (Sample 2, Trial 1).

Manually Pressed Sample 2, Trial 2

The focus of this growth was to produce a crystal using a wider capillary channel in an effort to grow a larger diameter Ce:LuAG crystal. The μ-PD experimental procedure is described below,

1. Chamber was evacuated to a vacuum of -25 PSI. Argon was then pumped in, to a pressure of +7 PSI, and left circulating for 1 hour prior to initializing the heating profile.
2. Temperature was increased from RT to 2044°C (SP: 45) over 2 hours.

   No appreciable change observed.
3. Temperature was increased to 2060°C (SP: 47) in 6 minutes.

   No appreciable change observed.
4. Temperature was increased to 2083°C (SP: 50) in 9 minutes.
5. Seed was left in contact with the melt for 30 minutes, after which there was no observable change in the melt.
6. Temperature was increased to 2098°C (SP: 52) in 6 minutes.

   No appreciable change observed.
7. Temperature was increased to 2105°C (SP: 53) in 3 minutes.
8. Seeding attempt failed after less than a millimeter at a rate of 0.1 $\frac{\text{mm}}{\text{min}}$. Seed was left in contact for 30 minutes.
9. Crystal seeding failed.
10. Temperature increased to 2112°C (SP: 54) instantly, seeding failed.
11. Temperature increased to 2119°C (SP: 55) instantly, seeding failed.
12. It was determined that the bottom of the melt had solidified and was preventing crystal seeding. Chamber was cooled to RT in 1 hour.

Manually Pressed Sample 2, Trial 3

The focus of this growth was to produce a crystal using a wider capillary channel in an effort to grow a larger diameter Ce:LuAG crystal. The μ-PD experimental procedure is described below,

1. Chamber was evacuated to a vacuum of -25 PSI. Argon was then pumped in, to a pressure of +7 PSI, and left circulating for 1 hour prior to initializing the heating profile.

2. Temperature was increased from RT to 2068°C (SP: 48) over 2 hours.

   No appreciable change observed.

3. Temperature was increased to 2083°C (SP: 50) in 6 minutes and held for 10 minutes.

   No appreciable change observed.

4. Temperature was increased to 2098°C (SP: 52) in 6 minutes and held for 10 minutes.

   No appreciable change observed.

5. Temperature was increased to 2112°C (SP: 54) in 6 minutes and held for 30 minutes.

   No appreciable change observed.

6. Temperature was increased to 2119°C (SP: 55) in 3 minutes and held for 30 minutes.

7. Seeding attempt failed, with no discernible motion from the melt.

8. Temperature was increased to 2132°C (SP: 57) in 6 minutes and held for 10 minutes.

9. Seeding successful at a pull-down rate of 0.1 $\frac{\text{mm}}{\text{min}}$, temperature was increased to 2142°C (SP: 57.5) to widen diameter.

10. Growth attempt was allowed to run overnight and cooled to RT in 1 hour.

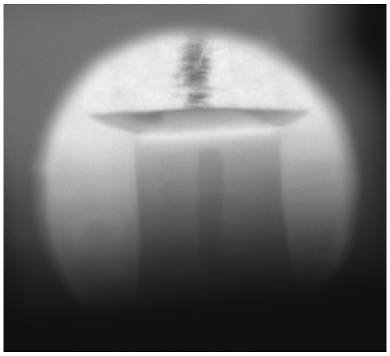

Figure 30: Stable Ce:LuAG crystal growth with larger crucible nozzle (Sample 2, Trial 3).

Crystal Synthesis: $MgTa_2O_6$

Iridium was used as the crucible and after-heater material because of its high resistance to high-temperature oxide melts, this limits the chemical interaction between the liquid and the crucible.

The growth atmosphere was modified and filled with a positive argon pressure of 5 PSI so that the crucible would not oxidize. A single layer of ceramic insulation was used to maintain experimental temperatures around the crucible and after-heater.

Loose Powder Sample 1, Melt Check

Due to the limited amount of literature present for this magnesium tantalate, a melt check was used to answer some initial questions of compatibility. A melt check was performed to confirm crucible compatibility and get an idea of the melt behavior for a given temperature range. This test was completed using a five gram sample. This sample was not densified and filled the crucible with a powder mixture. A sample of the mixed oxide powder was taken for XRPD to confirm that it was forming the correct magnesium tantalate, $MgTa_2O_6$.

Additional precautions were taken because the viscosity of the liquid melt was unknown. If the surface tension of the melt was not sufficient it would simply free-flow from the crucible once it liquefied, moving under the force of gravity. The experimental procedure is listed below,

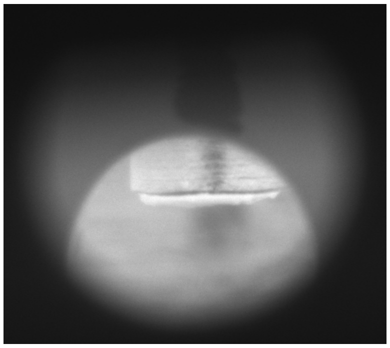

Figure 31: Melt check for $MgTa_2O_6$.

1. Chamber was evacuated to a vacuum of -25 psi then argon was pumped in to a pressure of +7 psi and left circulating for 1 hour prior to the start of the heating profile.
2. Induction heater was programmed to increase from 0 to 27 set-point.
3. Heating profile was stopped at 26.5 set-point when the melt was seen emerging from the crucible nozzle as shown in Figure 31.
4. Chamber was cooled from 26.5 set-point to RT in 1 hour.

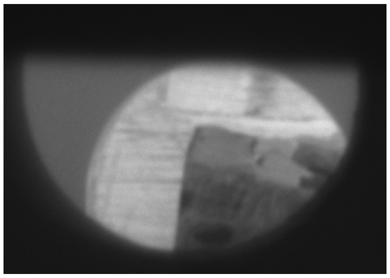

Figure 32: $MgTa_2O_6$ seed attempt (Sample 1, Trial 1).

A second XRPD sample was taken from the crucible after the melt test was completed to confirm that the compound was still present and that a principle compound had evaporated.

Loose Powder Sample 1, Trial 1

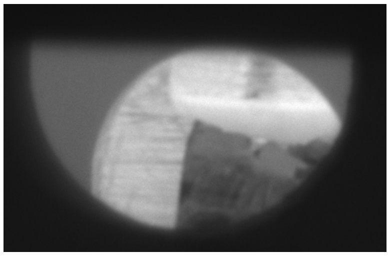

Figure 33: Second $MgTa_2O_6$ seed attempt with more emerging melt (Sample 1, Trail 1).

With compatibility confirmed we installed our seed rod, shown in Figure 34. The μ-PD experimental procedure is described below,

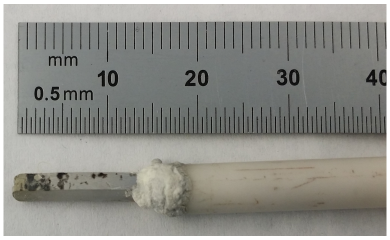

Figure 34: Seed used for $MgTa_2O_6$ growth attempt, glued to ceramic post with thermal adhesive.

1. Chamber was evacuated to a vacuum of -25 PSI. Argon was then pumped in, to a pressure of +7 PSI, and left circulating for 1 hour prior to initializing the heating profile.
2. Temperature was increased from RT to 1876°C (SP: 28) over 2 hours.

   Once complete, the melt was seen emerging from the end of the crucible nozzle.
3. Attempts to contact the melt were unsuccessful even with adjustments to the seed location in the y-direction. The amount of misalignment exceeded the length of travel for this adjustment
4. Temperature was increased incrementally to 1888°C (SP: 29) in 10 minutes.

   Despite the melt protruding more from the crucible nozzle, seed attempts continued to fail due to this misalignment.
5. Chamber was cooled to RT in 1 hour.

Loose Powder Sample 1, Trial 2

We realigned the seed with the crucible and made sure that we had adjustability in x/y directions. Once this was complete we assembled and aligned the fixture and prepared the chamber for our growth attempt. The μ-PD experimental procedure is described below,

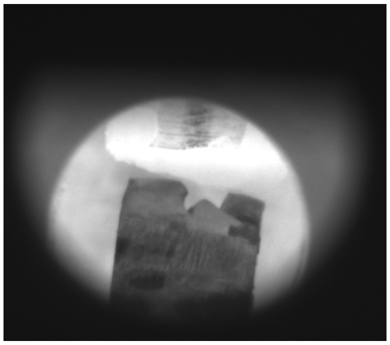

Figure 35: $MgTa_2O_6$ seed attempt (Sample 1, Trial 2).

1. Chamber was evacuated to a vacuum of -25 PSI. Argon was then pumped in, to a pressure of +7 PSI, and left circulating for 1 hour prior to initializing the heating profile.
2. Temperature was increased from RT to 1863°C (SP: 27) over 2 hours.

   No appreciable change observed.
3. Temperature was increased to 1974°C (SP: 37) over 50 minutes.

   Several seed attempts were tried but each time the droplet appeared larger it would shrink away from the seed.
4. We confirmed that the seed was aligned with the capillary channel but despite correct alignment the seed would not catch.
5. After making several more attempts at 1974°C (SP: 37) we determined that the apparatus needed to be cleaned and the experiment retried.
6. Chamber was cooled to RT in 1 hour.

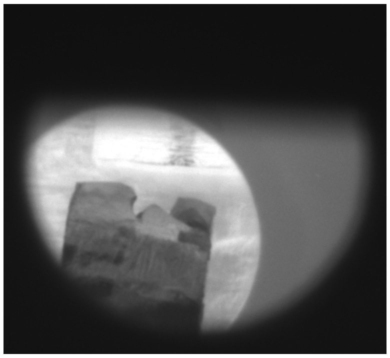

Figure 36: Second $MgTa_2O_6$ seed attempt after seed translation (Sample 1, Trial 2).

Loose Powder Sample 1, Trial 3

We were able to achieve growth during this trial. The μ-PD experimental procedure is described below,

1. Chamber was evacuated to a vacuum of -25 PSI. Argon was then pumped in, to a pressure of +7 PSI, and left circulating for 1 hour prior to initializing the heating profile.
2. Temperature was increased from RT to 1863°C (SP: 27) over 30 minutes.
3. Temperature was increased to 1900°C (SP: 30) in 9 minutes.

   At this time it appeared that a small part of the melt was attached to the seed. We began a controlled pull down at a rate of 0.7 $\frac{\text{mm}}{\text{min}}$. After a small distance the growth failed.
4. Temperature was increased to 1922°C (SP: 32) in 6 minutes.

   We attempted another seeding once the temperature stabilized but the attempt failed sometime shortly after. This growth, while brief, was longer than the first seeding.

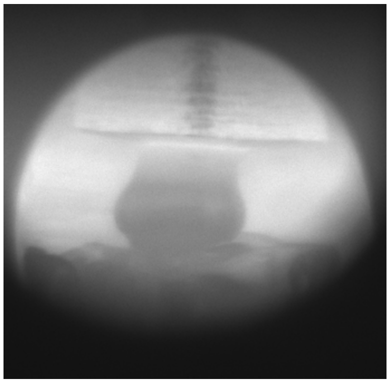

Figure 37: $MgTa_2O_6$ growth initialization (Sample 1, Trail 3).

The melt became transparent and difficult to see in any focus. At some point, contact was lost and the seed was moved back up to establish contact again.

5. Temperature was increased to 1933°C (SP: 33) in 3 minutes.

   No appreciable change in melt shape detected.

6. Temperature was increased to 1944°C (SP: 34) in 3 minutes.

   We began a controlled pull down at a rate of 0.7 $\frac{\text{mm}}{\text{min}}$ and failed quickly.

7. Temperature was increased to 1954°C (SP: 35) in 3 minutes.

   No appreciable change in melt shape detected.

8. Temperature was increased to 1974°C (SP: 37) in 6 minutes.

   We stopped the temperature increase at 1972°C (SP: 36.8) after a large change was observed in the viscosity of the melt.

9. Temperature was decreased to 1954°C (SP: 35) in less than a minute.

   We immediately began to pull at a rate of 0.7 $\frac{\text{mm}}{\text{min}}$ which we found to be too fast and the seed separated from the melt. The melt began to flow rapidly, covering the seed and seed holder.

10. Temperature was increased to 1964°C (SP: 36).

    The melt was re-seeded on top of the flow that had stuck to the seed and seed holder.

11. Crystal seeded successfully and was pulled at a rate of 0.6 $\frac{\text{mm}}{\text{min}}$.
12. Crystal was grown at this rate until separation occurred when the melt in the crucible was exhausted.
13. Chamber was cooled to RT in 1 hour.

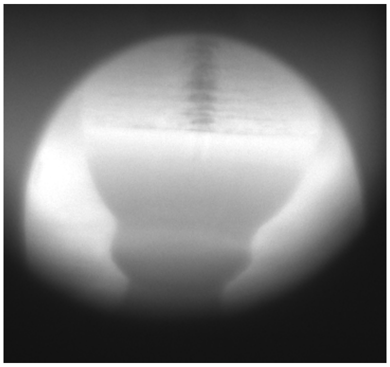

Figure 38: Increasing diameter of $MgTa_2O_6$ growth (Sample 1, Trial 3).

Manually Pressed Sample 3, Trial 1

This attempt was done with the pressed sample. This growth attempt was conducted with a new ceramic insulator as the previous one was contaminated on the inside. The μ-PD experimental procedure is described below,

1. Chamber was evacuated to a vacuum of -25 PSI. Argon was then pumped in, to a pressure of +7 PSI, and left circulating for 1 hour prior to initializing the heating profile.
2. Temperature was increased from RT to 1933°C (SP: 33) in 1 hour.

   Heating profile was stopped at 1917°C (SP: 31.5) when it was observed that the melt was visible from the end of the crucible nozzle. A seed attempt was attempted but failed.

3. Temperature was increased to 1922°C (SP: 32)

   No appreciable change observed.

4. Temperature was increased to 1964°C (SP: 36) over 12 minutes.

   Seeding attempts occurred with each set-point increase at 1933°C, 1944°C, 1954°C and 1964°C. Each attempt failed.

5. Seed was left in contact with the exposed melt for 30 minutes.

   Seed attempt failed.

6. Temperature was increased to 1969°C (SP: 36.5) over 15 minutes.

   Seed attempt failed.

7. Temperature was increased to 1988°C (SP: 38.5) over 15 minutes.

   Seed attempt failed. It was observed that the melt was retreating back into the capillary channel as the seed was placed in contact.

8. Chamber was cooled to RT in 1 hour.

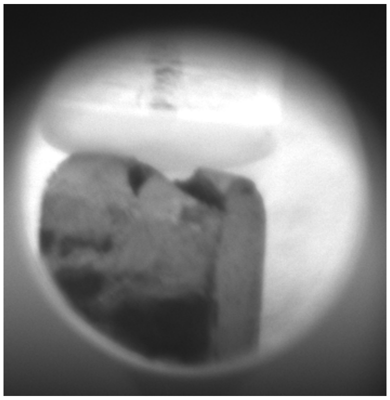

Figure 39: The $MgTa_2O_6$ melt would not adhere to the seed due to poor material compatibility (Sample 3, Trial 1).

Manually Pressed Sample 3, Trial 2

This attempt was done with the pressed sample. The μ-PD experimental procedure is described below,

1. Chamber was evacuated to a vacuum of -25 PSI. Argon was then pumped in, to a pressure of +7 PSI, and left circulating for 1 hour prior to initializing the heating profile.

2. Temperature was increased from RT to 1900°C (SP: 30) in 1 hour.

   No appreciable change observed.

3. Temperature was increased to 1911°C (SP: 31) in 3 minutes.

   No appreciable change observed.

4. Temperature was increased to 1933°C (SP: 33) in 6 minutes.

   Seed attempt failed, melt observed thinly across the bottom of the crucible nozzle.

5. Temperature was increased to 1944°C (SP: 34) in 3 minutes.

   No appreciable change observed.

6. Temperature was increased to 1954°C (SP: 35) in 6 minutes.

   No appreciable change observed.

7. Temperature was increased to 1959°C (SP: 35.5) in 3 minutes.

   No appreciable change observed.

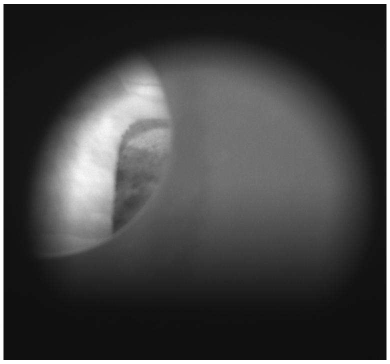

Figure 40: The seed rod pressed against the $MgTa_2O_6$ melt with sufficient force to rotate the after-heater and obstruct viewing (Sample 3, Trial 2).

8. Temperature was increased to 1969°C (SP: 36.5) in 6 minutes.

   No appreciable change observed.

9. Temperature was increased to 1974°C (SP: 37) in 3 minutes.

10. Seed was left in contact with the melt for 30 minutes.

    Seeding attempt failed.

11. Seed was left in contact with melt for another 30 minutes.

    Seeding attempt failed.

12. Temperature was increased to 1983°C (SP: 38) over 30 minutes with seed in contact.

    Seeding attempt failed.

13. Seed was left in contact with melt for 30 minutes.

    Seeding attempt failed.

14. Temperature was increased to 1992°C (SP: 39) in 6 minutes.

15. Seed left in contact for 30 minutes.

    Seeding attempt failed.

16. Chamber was cooled to RT in 1 hour.

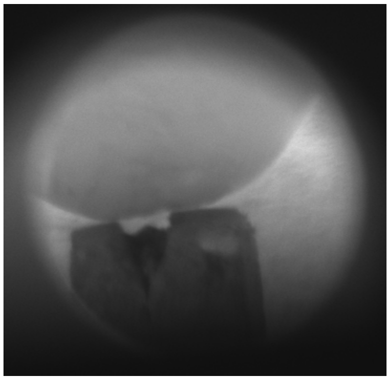

Figure 41: The $MgTa_2O_6$ melt did not attach to the seed but continued to discharge (Sample 3, Trial 3).

Manually Pressed Sample 3, Trial 3

This attempt was done with the pressed sample. The μ-PD experimental procedure is described below,

1. Chamber was evacuated to a vacuum of -25 PSI. Argon was then pumped in, to a pressure of +7 PSI, and left circulating for 1 hour prior to initializing the heating profile.

2. Temperature was increased from RT to 1922°C (SP: 32) over an hour.

   Seed was raised, making contact with the crucible. No melt detected.

3. Temperature was increased incrementally to 1954°C (SP: 35).

4. Seed was left in contact for 30 minutes.

   Seed was drawn downwards and the melt followed downwards but failed to seed.

5. Temperature was increased to 1969°C (SP: 36.5).

   Seed was moved to the right in order to center a defect on the seed with the lowest point in the melt. The seed was left in contact with the melt for 15 minutes. It was hypothesized that the melt would have better success seeding on a rough surface. This however was unsuccessful as well. The seed was moved back to its original position.

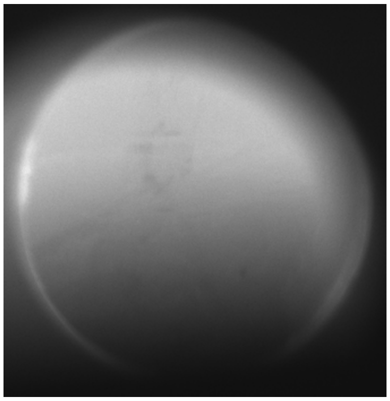

Figure 42: The $MgTa_2O_6$ discharge covered the entire viewing window (Sample 3, Trial 3).

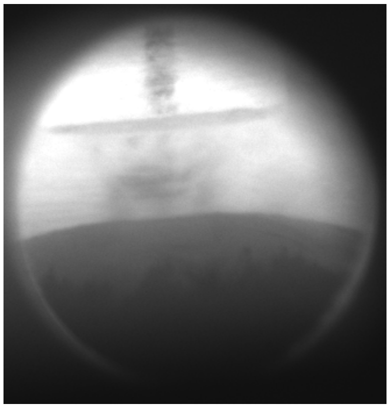

Figure 43: The end of the $MgTa_2O_6$ discharge emptied the crucible (Sample 3, Trial 3).

6. Temperature was increased incrementally to 1992°C (SP: 39).
7. Seed was left in contact for 15 minutes.

   It was observed that the seed was physically supporting the melt. Adjusting the seed in the x/y directions moved the seed and downwards motion let the melt move downwards. Despite this physical support, the melt failed to attach to the seed.

   Melt wet severely along the entire outside of the nozzle, flowing upwards away from the seed while still in contact.
8. Seed was deceased at a rate of 0.50 $\frac{mm}{min}$ and a large mass of material flowed downwards after it but failed to seed.
9. Seed rate was adjusted to 0.10 $\frac{mm}{min}$.
10. The mass of material descended, taking with it melt that had wet on the exterior surface of the crucible.
11. A final seed attempt occurred after the top of the material mass was observed but this failed.
12. Temperature was increased to 2001°C (SP: 40) in 3 minutes.

    Seeding was attempted again but was only minimally successful as the melt seemed to be exhausted.
13. Chamber was cooled to RT in 1 hour.

A seed was prepared from the previous growth. As evidenced from the past growth attempts the $MgTa_2O_6$ melt had a difficult time seeding against the iridium seed. By producing a seed of the same material we eliminate this material compatibility issue. Further experiments with this compatible seed will need to proceed cautiously as the melting temperature of the seed and the melt is now the same. The procedure used to construct a new seed is described below,

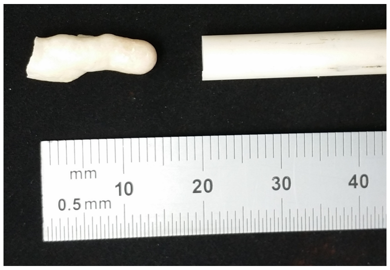

Figure 44: The $MgTa_2O_6$ discharge from the last test made for a compatible seed.

1. Previous growth was broken in half. One half was pulverized for XRPD testing and the other half would be used as a new seed for future growth attempts.
2. The seed portion selected was sanded down so that if would fit within the hollow ceramic seed rod made of high purity Al_2O_3. This was accomplished using 600/P1200 grit grinding paper.
3. Once the growth was able to fit inside the hollow ceramic seed rod the two were adhered together with a Zirconia adhesive produced by Cotronics.
4. The seed and seed rod were placed in a furnace at 60°C overnight to allow time to solidify.

Due to gravity the excess adhesive collected on the one side of the seed while solidifying and required additional sanding so that it could move without obstruction when installed within the μ-PD chamber. The limitation was the diameter of the ceramic support atop the quartz tube. Once this excess adhesive was removed the new seed was ready to use in subsequent μ-PD experiments.

Figure 45: The dried $MgTa_2O_6$ seed needed to be sanded down slightly prior to use.

Manually Pressed Sample 4, Trial 1

This attempt was done with the new ten gram pressed sample. The μ-PD experimental procedure is described below,

1. Chamber was evacuated to a vacuum of -25 PSI. Argon was then pumped in, to a pressure of +7 PSI, and left circulating for 1 hour prior to initializing the heating profile.

2. Temperature was increased from RT to 1900°C (SP: 30) over 2 hours.

   The melt emerged readily from the crucible nozzle.

3. Temperature was decreased to 1876°C (SP: 28).

   With this decrease in temperature the melt stabilized and no longer threatened to free-flow from the crucible nozzle.

4. Temperature was increased back to 1900°C (SP: 30) in 6 minutes.

   Melt began to descend from crucible nozzle and seeding was initiated at a pull down rate of 0.10 $\frac{\text{mm}}{\text{min}}$. Crystal separated shortly after with the diameter of the crystal decreasing until termination.

5. Temperature was increased to 1906°C (SP: 30.5) in 6 minutes.

6. Seed was left in contact for 30 minutes.

   Seeding was re-initialized. Pull-down rate was the same at 0.10 $\frac{\text{mm}}{\text{min}}$. Temperature was increased incrementally to combat the decreasing crystal diameter up to 1910°C (SP: 30.9) where separation finally occurred.

7. Seed was left in contact with the melt for 15 minutes.

   Seed attempt failed.

8. Temperature was increased to 1911°C (SP: 31).

9. Temperature was increased to 1917°C (SP: 31.5) in 6 minutes.

   Seeding attempt was successful but failed after a short distance

10. Chamber was cooled to RT in 1 hour.

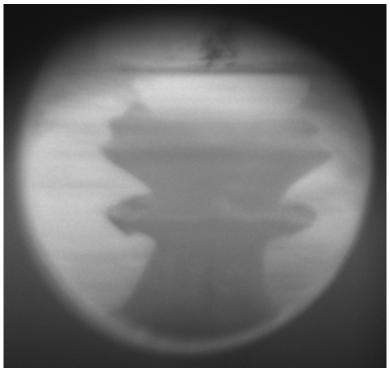

Figure 46: Variable diameter $MgTa_2O_6$ growth seeded on new constructed $MgTa_2O_6$ seed (Sample 4, Trial 1).

Manually Pressed Sample 4, Trial 2

This attempt was done with the ten gram pressed sample. The μ-PD experimental procedure is described below,

1. Chamber was evacuated to a vacuum of -25 PSI. Argon was then pumped in, to a pressure of +7 PSI, and left circulating for 1 hour prior to initializing the heating profile.
2. Temperature was increased from RT to 1876°C (SP: 28) in 2 hours.

   This temperature was then maintained for 2 hours in an attempt to better acclimate the melt.
3. Temperature was increased to 1900°C (SP: 30) in 30 minutes.

   No appreciable change observed.
4. Temperature was increased to 1911°C (SP: 31) in 6 minutes.

   Seeding initialized at a pull down rate of 0.10 $\frac{\text{mm}}{\text{min}}$. Crystal seeded and grew larger in diameter before separating from the melt.

   Contact was reestablished but the existing crystal was pulled into the melt. The bottom side of this was too cold to reseed, preventing further crystal growth.
5. Chamber was cooled to RT in 1 hour.

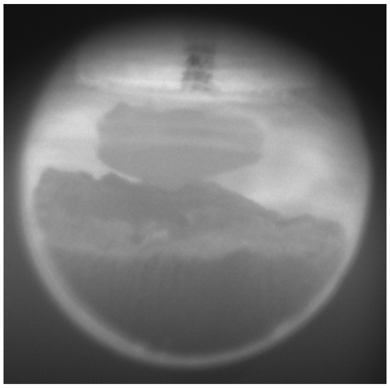

Figure 47: $MgTa_2O_6$ growth initiated at a small diameter before growing larger and cooling quickly (Sample 4, Trial 2).

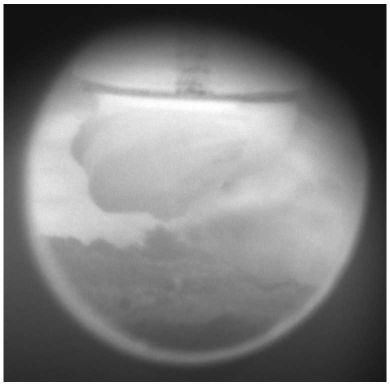

Figure 48: The small initial $MgTa_2O_6$ growth diameter broke once the mass above it was seeded again, plugging the capillary channel with relatively cool $MgTa_2O_6$ (Sample 4, Trial 2).

Manually Pressed Sample 4, Trial 3

This attempt was done with the ten gram pressed sample. The μ-PD experimental procedure is described below,

1. Chamber was evacuated to a vacuum of -25 PSI. Argon was then pumped in, to a pressure of +7 PSI, and left circulating for 1 hour prior to initializing the heating profile.
2. Temperature was increased from RT to 1900°C (SP: 30) in 2 hours.
3. Seed was brought into contact with melt.
4. Temperature was increased to 1906°C (SP: 30.5) in 6 minutes.

   Seeding was initialized with a pull-down rate of 0.10 $\frac{\text{mm}}{\text{min}}$. Diameter decreased on forming crystal.
5. Temperature was increased to 1910°C (SP: 30.9).

   Uncontrollable flow occurred.
6. Temperature was immediately reduced to 1906°C (SP: 30.5) as crystal formation continued.

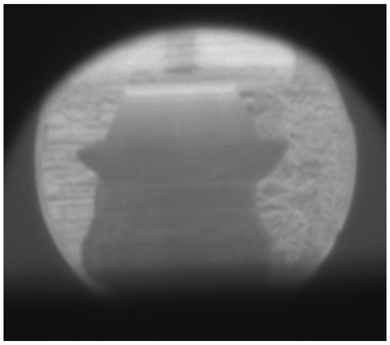

Figure 49: Variable diameter $MgTa_2O_6$ growth (Sample 4, Trial 3).

7. Temperature was increased incrementally to 1911°C (SP: 31).

   The crystal growth terminated several times and was re-seeded after each failure.

8. Chamber was cooled to RT in 1 hour.

The crystal from the previous μ-PD experiment was extracted from the chamber but when an attempt to remove the growth from the seed was made, the seed broke, with a good portion of the seed still stuck to the sample growth as shown in Figure 50. The sample required removal from the seed using a wire saw shown in Figure 53. The separation procedure is described below,

1. Rubber fixture was placed on a hot plate with solid glue. The glue was allowed to melt at the rubber fixture surface.
2. Sample and seed portion to be separated were then placed on the rubber fixture once the glue had begun to melt.
3. Rubber fixture was cooled with the sample adhered to its surface.
4. Sample to be separated was then cut by the wire saw.
5. Rubber fixture was again heated on the hot plate until the seed portion and sample were removed from the melted glue.

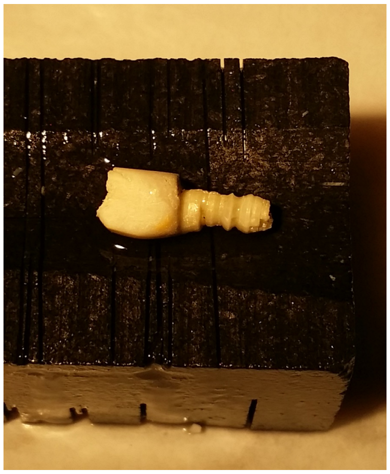

Figure 50: $MgTa_2O_6$ sample to be separated affixed on rubber fixture.

The portion of the seed separated from the sample was discarded and the remaining seed was used for future testing despite being smaller. The smaller seed was still preferable to using the iridium seed.

The temperature gradient across the seed and the crucible nozzle is now more sensitive due to the smaller seed. Since the melt and the seed are both made of the same material it is critical to keep the melt liquefied without liquefying the seed below it.

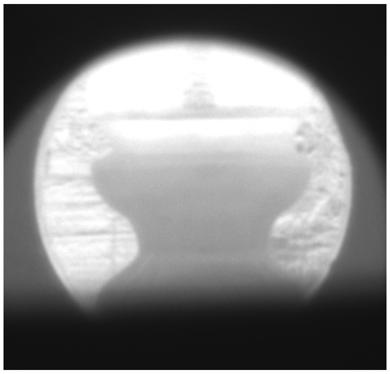

Figure 51: Variable diameter $MgTa_2O_6$ growth (Sample 4, Trial 4).

Manually Pressed Sample 4, Trial 4

This attempt was done with the ten gram pressed sample. The μ-PD experimental procedure is described below,

1. Chamber was evacuated to a vacuum of -25 PSI. Argon was then pumped in, to a pressure of +7 PSI, and left circulating for 1 hour prior to initializing the heating profile.
2. Temperature was increased from RT to 1888°C (SP: 29) set-point in 2 hours.
3. Seed was brought into contact with the emerging melt.
4. Temperature was increased to 1911°C (SP: 31) in 30 minutes.

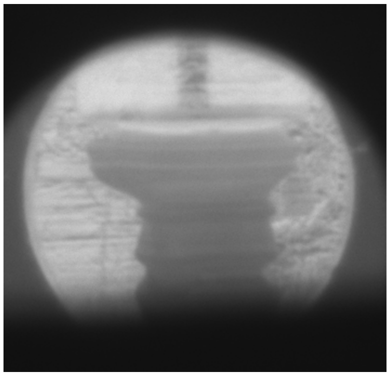

Figure 52: Variable diameter $MgTa_2O_6$ growth after seeding restart (Sample 4, Trial 4).

Figure 53: Wire saw used to separate sample growth from broken seed.

Seeding was initialized with a pull-down rate of 0.50 $\frac{\text{mm}}{\text{min}}$. Soon after the crystal separated from the melt. The crystal was brought back into contact.

5. Temperature was increased to 1954°C (SP: 35).

   Seeding was successfully restarted at the same pull-down rate. Experiment was left to run overnight.

6. Chamber was cooled to RT in 1 hour.

Manually Pressed Sample 4, Trial 5

This attempt was done with the ten gram pressed sample. The μ-PD experimental procedure is described below,

1. Chamber was evacuated to a vacuum of -25 PSI. Argon was then pumped in, to a pressure of +7 PSI, and left circulating for 1 hour prior to initializing the heating profile.

2. Temperature was increased from RT to 1944°C (SP: 34) in 2 hours.

3. Seed was brought into contact with the emerging melt.

4. Temperature was increased incrementally to 1954°C (SP: 35).

   Melt flow was obstructed by seed but wet the outside of the crucible nozzle. Seeding was initialized with a pull-down rate

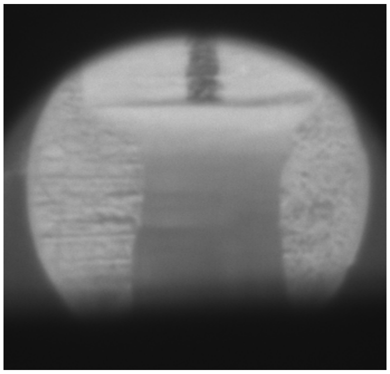

Figure 54: Variable diameter $MgTa_2O_6$ growth (Sample 4, Trial 5).

of 0.50 $\frac{\text{mm}}{\text{min}}$, removing the wetted melt from the exterior of the crucible.

5. Temperature was maintained and pull-down continued but with several required restarts.

6. Chamber was cooled to RT in 1 hour.

X-ray Powder Diffraction

X-ray powder diffraction (XRPD) testing was performed at Lawrence Berkeley National Laboratory (LBNL) using a Siemens SMART-CCD diffractometer equipped with a normal focus, 2.4 kW sealed tube x-ray source (Mo Kα, $\lambda = 0.71073$ Å) operating at 50 kW and 40 mA.

Samples were ground into fine powders with a mortar and pestle and mounted at the center of plastic rings with masking tape. A prepared sample is shown in Figure 55.

An diffraction pattern example is shown in Figure 56. These rings need to be converted into an output spectrum, which is accomplished by in-house software at LBNL. The procedure for this conversion is described below,

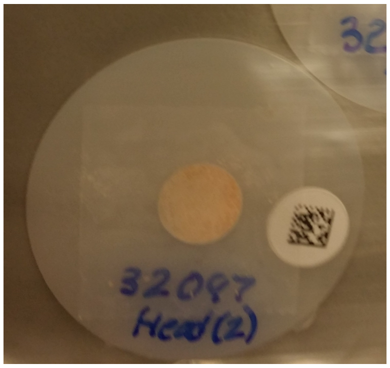

Figure 55: Prepared sample for XRPD analysis.

1. The sample output is calibrated against the sodium chloride (NaCl) sample that that was run that same day.

2. The user selects 5-10 points along the innermost of the NaCl sample. This ring represents the 2θ=32 peak that corresponds to the highest peak of the sample, registering the 200 planes.

3. When this calibration is processed the sample of interest ring pattern is loaded. From this a plot is produced.

4. This plot is then saved off and loaded in Match!, a phase identification program created by Crystal Impact.

5. Here the plot is analyzed and compared against a database of compounds that correctly identify peaks in the sample and give figure of merit values that display the relative confidence of its selections with a value of one being a perfect match to a standard on record.

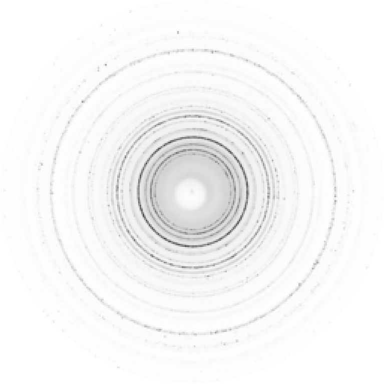

Figure 56: Raw XRPD output, prior to post-processing.

X-ray Luminescence

X-ray luminescence (XRL) testing was performed at Lawrence Berkeley National Laboratory (LBNL) using a SpectraPro-2150i spectrometer made by Princeton Instruments coupled to a thermoelectrically cooled PIXIS:100B charge coupled detector (CCD) also from Princeton Instruments. This measured the relative intensity of the x-ray emission spectra.

Crystal Mounting

Sample mounts were prepared in a Buehler Pneumet I mounting press, shown in Figure 57 with Buehler Konductomet in preparation for SEM testing. Buehler Konductomet is a graphite and silicon dioxide (SiO_2) filled phenolic thermoset used specifically for non-carbon based samples in SEM analysis. This allows the sample mount to be conductive during testing, however, the sample must still be coated. Samples were positioned vertically in the mount with the aid of plastic clips from MetLab Corporation. The procedure for producing these mounts is listed below,


Figure 57: Buehler Pneumet I mounting press.

1. Air supply was turned on and the platform raised on the press.
2. Samples were placed vertically on the press platform with the assistance of plastic clips. The section to be polished was placed facing down against the base. For polishing, this will act as our top surface.
3. The platform was lowered into the cavity and the cavity was filled with Buehler Konductomet thermoset.
4. The platform was lowered further and the sample was confirmed to be vertical before covering it with more thermoset.
5. The top was screwed into place and the heating element was applied around the cavity's external circumference.
6. Once secured and sealed the press was brought to a pressure of 55-60 PSI and maintained for ten minutes.
7. The heater was then removed and pressure was decreased to ATM. The sample was then removed and allowed to cool.
8. Between each mount produced, the apparatus was thoroughly cleaned so that the platform would actuate smoothly.
9. Once samples were completed the apparatus was cleaned and the air supply was turned off. A completed sample is shown in Figure 58.

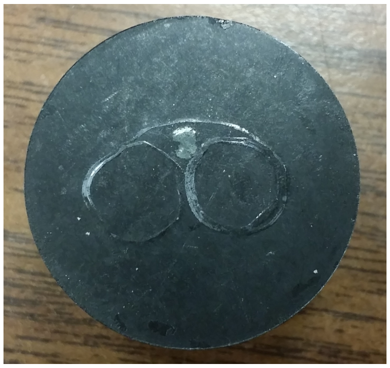
Figure 58: Bottom surface of the mount that will act as the top of the sample to be polished.

Crystal Polishing


Figure 59: Buehler Ecomet IV Polisher/-Grinder.

A quality polished surface must be present in order to effectively conduct SEM imaging. Polishing was performed with a Buehler Ecomet IV Polisher/Grinder shown in Figure 59. Standard grit grinding papers were used along with diamond compound from Metlab in 10 gram dispensing tubes.

The grinding papers used as our abrasive disks are listed in Table 6. Each polished sample required a unique regiment because of crystal fractures. These fractures created portions of loose crystal that needed to be removed. Once removed a more stable surface further into the sample could be used for polishing.

The diamond pastes are characterized by the size of the polycrystalline diamond within the compound. These pastes were applied to a Struers MD-Nap polishing cloth made of short synthetic nap. The diamond pastes used were 6, 3, 1, and 1/4 micron.

Standard ANSI Grit	European (P-Grade)	Diameter (μm)
320	P360	40.5
600	P1200	15.3
800	P2400	6.5
1200	P4000	2.5

Table 6: Grinding papers used for polishing ceramic samples.

With the grinding papers installed, water was used to lubricate and help move removed material away from the sample surface. Between each iteration of polishing the sample was dried along with the grinding paper and apparatus. This additional work extended the life of several of the finer grit grinding papers. If neglected, the papers would absorb the additional water and wrinkle severely, reducing their effectiveness.

The various diamond pastes employed were used on single nap polishing cloth. During process this was lubricated with ethanol and afterwards, cleaned extensively with a brush and water so that the remaining diamond paste was removed. The polishing cloth was then dried and the next diamond paste was applied.

In addition to diamond pastes an oxide polishing suspension (OP-S) was used. OP-S uses a colloidal silica suspension for abrasion. The type used for this testing had an average grain size of 0.05 μ.

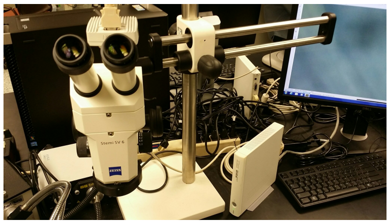

Figure 60: Zeiss Stemi SV-6 stereomicroscope used for observing polished samples.

A low-magnification Zeiss Stemi SV-6 stereomicroscope, shown in Figure 60, was used to observe samples periodically between polishes to evaluate surface quality. Images were streamed from a Nikon DS-Fi2, 5.0-megapixel color CCD camera head and stored with NIS Elements, imaging software from Nikon.

All images and observations were done at a magnification (MAG) of 5.0x. Lighting conditions were changed during testing to improve image clarity by adjusting auto exposure (AE) and analog gain (AG). These are seen most notably as adjusting the amount of light perceived in the images.

A Reichert Jung microscope light from Cambridge Instruments was used as an external light source to further illuminate the polished surface of the samples. This was kept relatively static in position at its full output of 150 W.

LBNL Sample 1468.7M

A new Ce:LuAG sample with reduced cerium content (< 0.5 mol% Ce) was sent from LBNL for analysis. While the initial crystal was smooth and uncracked, there was perimeter damage to the crystal after the mounting process where the clip made contact with the crystal. It appears that the pressure used to create the mounts was too high for the sample.

Speed was varied in an effort to get a better feel of what was appropriate for this material. The polishing procedure is detailed below,

1. 800/P2400 for 2 minutes at 200 RPM.

   Microscope: cracks were visible along the circumference of the crystal with scratches across the top surface parallel to the direction of polish as shown in Figure 61.

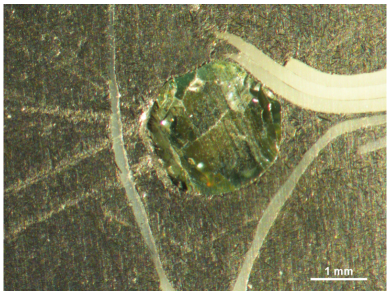

Figure 61: Ce:LuAG (< 0.5 mol% Ce) - 10 mm length crystal after first polish. MAG: 5.0x, AE: 1.5 ms, AG: 4.0x.

2. 800/P2400 for 2 minutes at 300 RPM.

   Microscope: cracks were relatively large and unaffected by the polishing process. The surface scratches were reduced and parallel to the direction of polish.

3. 1200/P4000 for 2 minutes at 100 RPM.

   Microscope: scratches were reduced with the finer polish, changes more subtle.

4. 1200/P4000 for 2 minutes at 100 RPM.

   Microscope: further reduced scratches, portions of the crystal have a completely smooth surface at this low-magnification as shown in Figure 62. With an acceptable surface, diamond pastes of decreasing diameter were used.

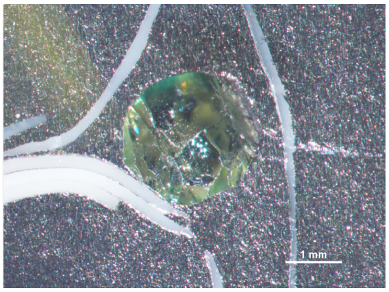

Figure 62: Ce:LuAG (< 0.5 mol% Ce) - 10 mm length crystal prior to diamond paste polishing. MAG: 5.0x, AE: 1 s, AG: 3.9x.

5. 6 μ for 12 minutes at 200 RPM.

6. 1 μ for 5 minutes at 200 RPM.

7. 0.05 μ OP-S for 5 minutes at 200 RPM.

   Microscope: OP-S was not completely removed and worked into the cracks of the crystal, this should not be detrimental to studying the polished surface but it will not be used in further polishing for this reason.

Ce:LuAG Sample 2, Trial 3

The procedure for polishing was separated into two phases: (1) remove material until a flat, relatively unfractured surface is reached; (2) polish the flat surface. The mounting process created fractures in the crystal due to the clip that was holding the sample vertical as shown in Figure 63. The fractured crystal needed to be removed prior to polishing an acceptable surface. The polishing procedure is detailed below,

1. 1200/P4000 for 5 minutes at 200 RPM.

   Microscope: crystal fractures increased in spread. It is apparent that they are separated from the main crystal below and need to be removed to establish a solid surface for SEM.

2. 800/P2400 for 5 minutes at 200 RPM.

   Microscope: noticeable improvement in polish, however the crystal remains fractured as shown in Figure 64.

3. 600/P1200 for 2 minutes at 200 RPM.

   Microscope: pieces of crystal have been removed, however more crystal debris is present.

4. 600/P1200 for 5 minutes at 200 RPM.

   Microscope: slight improvement but a significant about of debris remains.

5. 800/P2400 for 5 minutes at 200 RPM.

   Microscope: little to no improvement observed.

6. 320/P360 for 1 minute at 200 RPM.

   Microscope: some removal of loose crystal.

7. 800/P2400 for 2 minutes at 200 RPM.

   Microscope: no significant change, coarser grits will be used until the surface improves.

8. 320/P360 for 1 minute at 200 RPM.

9. 320/P360 for 1 additional minute at 200 RPM.

10. 320/P360 for 2 minutes at 200 RPM.

    Microscope: significant improvement, flat solid surface emerged and accounted for half of the crystal diameter. Proceeded more cautiously, with more visual checks during polishing.

11. 600/P1200 for 2 minutes at 200 RPM.

12. 800/P2400 for 2 minutes at 200 RPM.

    A new sandpaper was used as the other was wrinkled from water absorption.

13. 1200/P4000 for 2 minutes at 200 RPM.

    Microscope: solid surface showed improved polish.

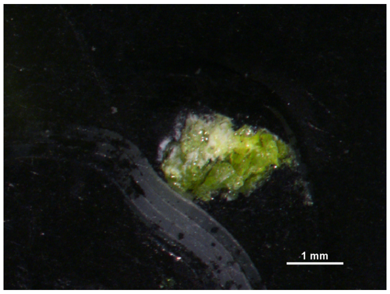

Figure 63: Ce:LuAG (1 mol% Ce) from 3 mm OD crucible nozzle. Initial crystal state after mounting. MAG: 5.0x, AE: 300 ms, AG: 2.8x

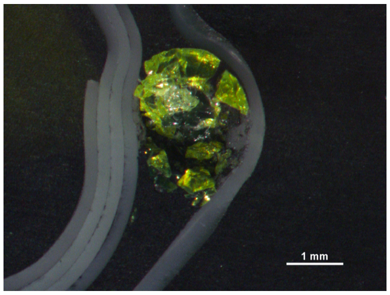

Figure 64: Ce:LuAG (1 mol% Ce) from 3 mm OD crucible nozzle. Crystal state after polish with 2400 grit sandpaper for 5 minutes at 200 rpm. MAG: 5.0x, AE: 150 ms, AG: 4.0x

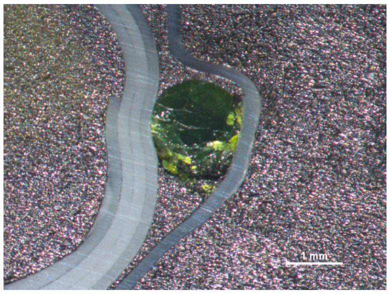

Figure 65: Ce:LuAG (1 mol% Ce) from 3 mm OD crucible nozzle. Crystal after diamond paste polishing. MAG: 5.0x, AE: 300 ms, AG: 4.8x

14. 1200/P4000 for 2 minutes at 200 RPM.

    Polish was perpendicular to the previous polish to ensure that the scratches in the previous direction were removed from the sample. With the majority of the surface scratches removed the diamond polishing process could begin.

15. 6 μ for 12 minutes at 200 RPM.

16. 3 μ for 5 minutes at 200 RPM.

17. 1 μ for 5 minutes at 200 RPM.

    Microscope: Surface is noticeably more transparent as shown in Figure 65.

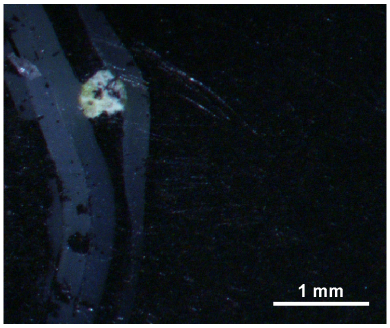

Figure 66: Ce:LuAG (1 mol% Ce) from 1 mm OD crucible nozzle. Crystal prior to polishing. MAG: 5.0x, AE: 30 ms, AG: 4.0x.

Ce:LuAG Sample 1, Trial 2

The sample tested was extremely small with a diameter of < 0.5 mm and viewing under a microscope revealed surface fractures and thermoset along the top surface that needed to be removed as shown in Figure 66. The polishing procedure is detailed below,

1. 320/P360 for 20 seconds at 200 RPM.

    Microscope: surface had been partially concealed by the thermoset, after this polish a fractured surface emerged.

2. 320/P360 for 1 minute at 200 RPM.

    Microscope: some fractured crystal removed as shown in Figure 67.

3. 600/P1200 for 1 minute at 200 RPM.

    Microscope: incremental improvement in surface quality specifically at the center of the crystal.

4. 600/P1200 for 2 minute at 200 RPM.

    Microscope: further progress on the crystal is difficult to observe due to the small diameter. A significant reduction of scratches was observed on the mount itself. It is assumed that the crystal surface is now level with the surface of the surrounding mount and clip.

5. 800/P2400 for 2 minutes at 200 RPM.

6. 1200/P4000 for 2 minutes at 200 RPM.

    Microscope: little observable change at low-MAG.

7. 6 μ for 12 minutes at 200 RPM.

8. 3 μ for 5 minutes at 200 RPM.

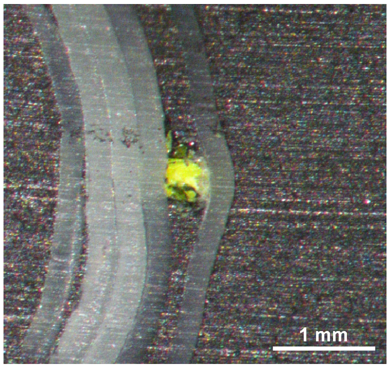

Figure 67: Ce:LuAG (1 mol% Ce) from 1 mm OD crucible nozzle. Crystal after 320 grit sandpaper. MAG: 5.0x, AE: 200 ms, AG: 5.6x.

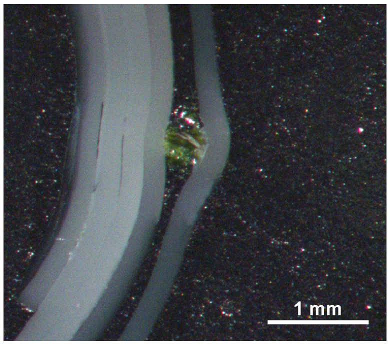

Figure 68: Ce:LuAG (1 mol% Ce) from 1 mm OD crucible nozzle. Crystal after diamond paste polishing. MAG: 5.0x, AE: 200 ms, AG: 5.6x

9. 1/4 μ for 5 minutes at 200 RPM.

   Microscope: solid surface near center of crystal is noticeably improved with respect to its transparency as shown in Figure 68.

$MgTa_2O_6$ Sample 4, Trial 5

This crystal presented a few challenges because of its irregular geometry and the fractures created in the mounting process. The first task was to create an acceptable surface as much of the crystal was submerged in thermoset as shown in Figure 69.

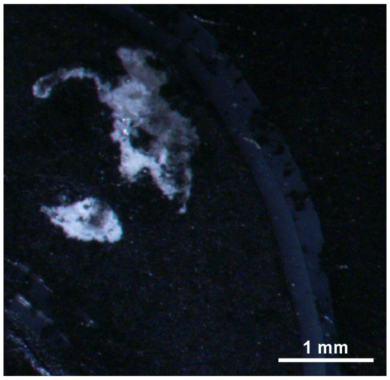

Figure 69: $MgTa_2O_6$ from 1 mm OD crucible nozzle. Initial crystal condition after mounting. MAG: 5.0x, AE: 30 ms, AG: 4.0x.

1. 320/P360 for 3 1/2 minutes at 200 RPM.

   Microscope: flat surface emerged, the center of the irregularly shaped surface is filled with thermoset. More material was removed after this in anticipation of the surface coming together underneath the thermoset.

2. 320/P360 for 6 minutes at 200 RPM.

   Microscope: flat surface filled in at its center, the top of the crystal was broken off with thermoset in the gap, implying that the crack occurred during the mounting process.

3. 800/P2400 for 2 minutes at 200 RPM.

4. 1200/P4000 for 2 minutes at 200 RPM.

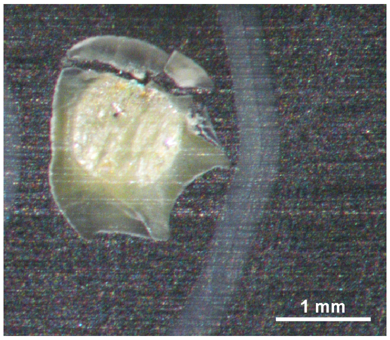

Figure 70: $MgTa_2O_6$ from 1 mm OD crucible nozzle. Crystal after second perpendicular polish with 4000 grit paper. MAG: 5.0x, AE: 200 ms, AG: 5.6x.

5. 1200/P4000 for 2 minutes at 200 RPM.

   Polish was performed perpendicular to the previous polish so that scratches could be removed. Scratches remained as shown in Figure 70.

6. 800/P2400 for 5 minutes at 200 RPM.

   Despite these polishes being perpendicular to the other polishes, they were unable to remove many of the scratches. At this time a coarser grit was used to flatten the surface.

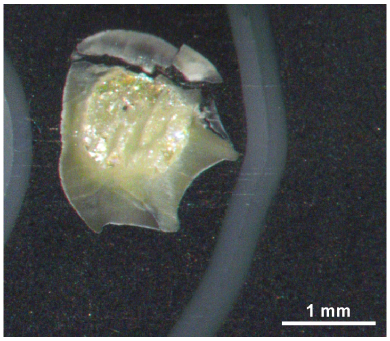

Figure 71: $MgTa_2O_6$ from 1 mm OD crucible nozzle. Crystal after repeated perpendicular polishes. MAG: 5.0x, AE: 200 ms, AG: 5.6x.

7. 800/P2400 for 6 minutes at 200 RPM.

   Polish had finally removed the major scratches observed at low-MAG as shown in Figure 71.

8. 1200/P4000 for 2 minutes at 200 RPM.

9. 6 μ for 12 minutes at 200 RPM.

10. 3 μ for 5 minutes at 200 RPM.

11. 1/4 μ for 5 minutes at 200 RPM.

Crystal Coating

The polished samples were then coated with a thin layer of tungsten (W). This was accomplished with a Leica EM MED020 modular high vacuum coater shown in Figure 73. The procedure used to coat these samples is outlined below,

1. The argon tank valve was opened and full speed vacuum was activated on the Leica control panel. Pump down continued to $< 10^{-4}$ bar.
2. Coater was programmed to deposit a thin 1 nm layer of tungsten on the surface of the samples. The chamber was large enough to accommodate all four of the samples in the same cycle.
3. Once at vacuum SP the coater was placed in standby and the shutter opened.
4. Argon was activated and the vacuum was confirmed to be stable.
5. Coater process was activated and the sputter rate was set to 0.1 nm/s.
6. Once coated to the desired thickness, argon was stopped and the shutter closed. The chamber was then brought back to ATM and the coated samples were removed.

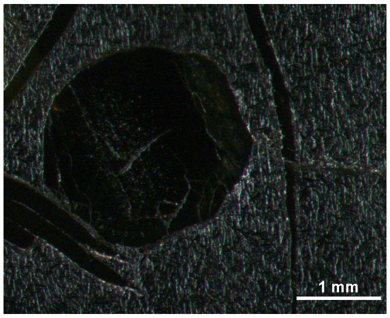

Figure 72: Ce:LuAG (< 0.5 mol% Ce) - 10mm length crystal after coating, 1 nm thickness tungsten coating. MAG: 5.0x, AE: 200 ms, AG: 5.6x.

Scanning Electron Microscopy

Performing SEM on insulators presents unique challenges as the electron-beam radiation produced induces a strong electric field. This electric field is due to the trapping of electrons within the specimen. This field alters the trajectories of the beam of electrons entering the specimen which severely limits the penetration depth. Additionally, this trapping leads to secondary electrons (SE) contrast dependence on the charged sample.[38]

[38] M. Belhaj, O. Jbara, S. Odof, K. Msellak, E.I. Rau, and M.V. Andrianov. An anomalous contrast in scanning electron microscopy of insulators: The pseudo-mirror effect. *Scanning*, 22(6):352–356, 2000

Figure 73: Leica EM MED020 modular high vacuum coater (Image from Leica).

Due to these effects the ceramic crystal samples were coated in a conductor to properly ground them. This conductive layer required a conductive mount and a mirror-finish polished sample.

SEM measurements were performed on a Mira 3 XMH electron microscope, which is a high vacuum model ($< 9\times10^{-3}$ Pa) for larger conductive samples. It is equipped with a Schottky Field Emission electron gun.

The procedure for acquiring images is described below,

1. Samples are loaded onto the fully motorized stage and moved into the chamber.
2. Chamber is sealed and pumped down to vacuum. The electron gun is turned on and the sample is located by adjusting the stage position and viewing through wide field.
3. Once the desired position is navigated to the electron gun is changed to resolution mode.
4. The sample is brought into focus by making fine adjustments to the working distance.
5. Images are captured at various magnifications after focus is achieved.

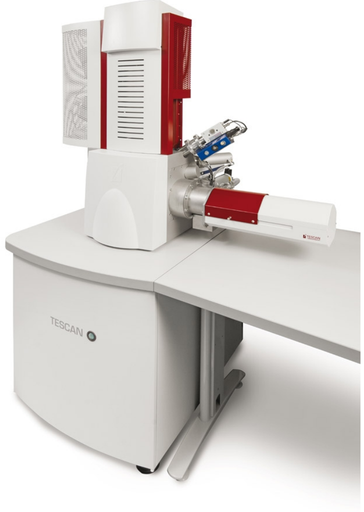

Figure 74: Mira XMH electron microscope (Image from Tescan).

6. Once complete, the chamber is brought back to ATM and the samples removed.

Energy-dispersive X-ray Spectroscopy

Energy-dispersive x-ray spectroscopy (EDS) testing was performed within the Mira 3 XMH microscope from an Apollo X module with an active area of 10 mm^2. Images were collected and processed through the Texture and Elemental Analytical Microscopy (TEAM) software package. Samples were measured in three different locations to reduce the odds of a false reading.

Surface charging is also a concern for insulators. For this reasons the samples tested were coated in tungsten and set in conductive mounts. The surface potential can rise quickly on un-coated samples due to the input of positive change and the emission of secondary electrons.

The characteristic K, L, and M x-ray line energies are listed in Table 7 for the elements of interest in our Ce:LuAG and $MgTa_2O_6$ samples.[39]

The values listed are only the strongest lines. The wavelength, λ, of the emission can be obtained from the expression,

$$\lambda = \frac{12398}{E} \tag{9}$$

where E is the energy of the emission in eV. The binding energies for the selected elements are shown in Table 8. A brief description of the procedure is listed,

1. Samples are loaded into the Mira 3 XMH microscope, pumped to vacuum and the microscope focused on the region of interest.
2. The Apollo X module was activated and the view scanned with the TEAM software. The remaining analysis was also performed through this application.
3. From this scanned image, areas were highlighted to perform EDS testing.
4. Energy-dispersive x-ray spectroscopy was performed on the area of interest and the output counts were compared against the eZAF standardless model algorithm for peak identification in the TEAM software.
5. Testing was repeated three times on different regions of the same sample to ensure a representative result.

[39] J.B. Kortright and A.C. Thompson. *X-ray data booklet*, chapter 1, pages 8–13. Lawrence Berkeley National Laboratory, 2009

Element	K α_1	K α_2	K β_1	L α_1	L α_2	L β_1	L β_2	L γ_1	M α_1
8 O	**0.5249**								
12 Mg	**1.25360**	**1.25360**	**1.3022**						
13 Al	**1.48670**	**1.48627**	**1.55745**						
58 Ce	34.7197	34.2789	39.2573	**4.8402**	**4.8230**	**5.2622**	**5.6134**	**6.052**	**0.883**
71 Lu	54.0698	52.9650	61.283	**7.6555**	**7.6049**	**8.7090**	**9.0489**	**10.1434**	1.5813
73 Ta	57.532	56.277	65.223	81.461	**8.0879**	**9.3431**	**9.6518**	**10.8952**	**1.710**
74 W	59.31824	57.9817	67.2443	**8.3976**	**8.3352**	**9.67235**	**9.9615**	**11.2859**	**1.7754**
77 Ir	64.8956	63.2867	73.5608	9.1751	9.0995	10.7083	10.9203	12.5126	1.9799

Table 7: Photon energies (keV), of principal K-, L-, and M-shell emission lines. Bold values are within our detector range.[35]

Element	K 1s	L$_1$ 2s	L$_2$ 2p$_{1/2}$	L$_3$ 2p$_{3/2}$	M$_2$ 3s	M$_2$ 3p$_{1/2}$	M$_3$ 3p$_{3/2}$	M$_4$ 3d$_{3/2}$	M$_5$ 3d$_{5/2}$	N$_1$ 4s	N$_2$ 4p$_{1/2}$	N$_3$ 4p$_{3/2}$
8 O	543.1	41.6										
12 Mg	1303.0	88.7	49.78	49.50								
13 Al	1559.6	117.8	72.95	72.55								
58 Ce	40443	6549	6164	5723	1436	1274	1187	902.4	883.8	291.0	223.2	206.5
71 Lu	63314	10870	10349	9244	2491	2264	2024	1639	1589	506.8	412.4	359.2
73 Ta	67416	11682	11136	9881	2708	2469	2194	1793	1735	563.4	463.4	359.2
74 W	69525	12100	11544	10207	2820	2575	2281	1872	1809	594.1	490.4	423.6
77 Ir	76111	13419	12824	11215	3174	2909	2551	2116	2040	691.1	577.8	495.8

Element	N$_4$ 4d$_{3/2}$	N$_5$ 4d$_{5/2}$	N$_6$ 4f$_{5/2}$	N$_7$ 4f$_{7/2}$	O$_1$ 5s	O$_2$ 5p$_{1/2}$	O$_3$ 5p$_{3/2}$	O$_4$ 5d$_{3/2}$	O$_5$ 5d$_{5/2}$	P$_1$ 6s	P$_2$ 6p$_{1/2}$	P$_3$ 6p$_{3/2}$
58 Ce	109	–	0.1	0.1	37.8	19.8	17.0					
71 Lu	206.1	196.3	8.9	7.5	57.3	33.6	26.7					
73 Ta	237.9	226.4	23.5	21.6	69.7	42.2	32.7					
74 W	255.9	243.5	33.6	31.4	75.6	45.3	36.8					
77 Ir	311.9	296.3	63.8	60.8	95.2	63.0	48.0					

Table 8: Electron binding energies, in electron volts, of selected elements.[35]

Results and Discussion

This section outlines the growth results of both the Ce:LuAG and $MgTa_2O_6$ compounds. The $MgTa_2O_6$ growth composition was confirmed through multiple x-ray powder diffraction tests. Both compounds were tested using x-ray luminescence to determine their emission spectra and potential as a scintillator. Samples of both compounds were then mounted, polished and coated in preparation for scanning electron microscopy and energy-dispersive x-ray spectroscopy analysis. These results are shown and discussed.

Group	Sample	Length (mm)
1	1460.3B	5
	1460.7M	5
	1460.10E	5
2	1468.3B	5
	1468.7M	5
3	1482.3E	5
	1482.10B	5
	1482.7M	10

Table 9: Additional Ce:LuAG samples sent from LBNL for testing.

Crystal Results: Ce:LuAG

The growth results of the Ce:LuAG crystals are summarized individually in this section along with details and additional observations. Results are summarized in Table 10. Experiments 1-4 were completed on a sample that was initially 10 grams while experiments 5-7 were completed on a sample that was 5 grams. Experiments proceeded sequentially with the last experiment having the smallest starting melt. This steady reduction in head pressure required slightly different adjustments from experiment to experiment.

Experiment	Sample Type	Sample/Trial	Result	Length (mm)
1	HP	1 / 1	+	25
2	HP	1 / 2	+	100
3	HP	1 / 3	+	13
4	HP	1 / 4	+	102
5	MP	2 / 1	-	–
6	MP	2 / 2	-	–
7	MP	2 / 3	+	23

Table 10: Results summary for Ce:LuAG μ-PD growths. Sample type is the method of preparation which was either hydraulically-pressed (HP) or manually-pressed (MP).

Additional samples were also received from LBNL for further testing. These samples are listed in Table 9. The amount of dopant in these samples was less than 0.5 mol%, which is less than half of the cerium content as the experimentally grown samples. The most obvious discrepancy, outside of the quality, is the relatively paler color yellow compared to the intense yellow of the experimentally grown crystals. All of the 5 mm crystals sent from LBNL are shown in Figure 75 along with their internally designated sample numbers.

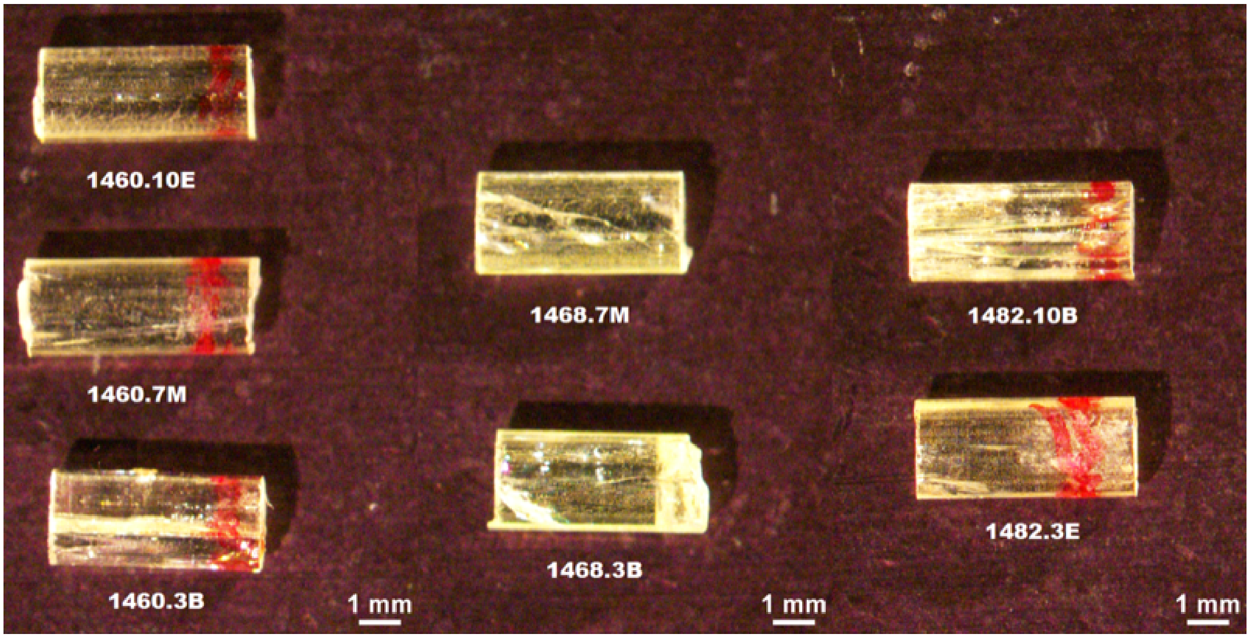

Figure 75: Composite image of the 5 mm Ce:LuAG samples sent from LBNL for further testing.

Pressed Powder: Sample 1, Trial 1

A 25 mm long Ce:LuAG crystal was successfully grown and pulled-down at a rate of 0.60 $\frac{\text{mm}}{\text{min}}$. During this crystal growth the crystal separated at a position outside of the viewing area, ending the experiment. Once the system was vented it was discovered that the crystal had separated approximately 2-3 mm from the bottom of the crucible as shown in Figure 76 with the majority of the crystal still attached to the $Lu_3Al_5O_{12}$ seed.

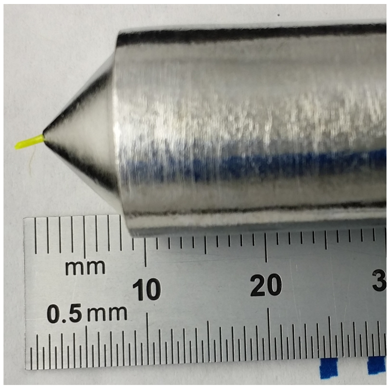

Figure 76: Position of Ce:LuAG crystal separation that occurred just out of the viewing window of the μ-PD chamber (Sample 1, Trial 1).

The crystal was removed by hand from the seed and is shown in Figure 77. A small portion of the crystal attached to the crucible was recovered with the remaining crystal removed with grinding paper.

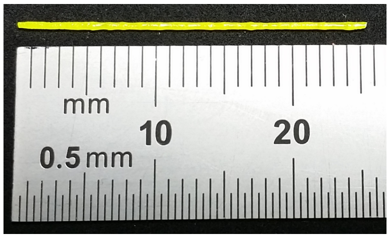

Figure 77: A 25 mm long Ce:LuAG crystal with an approximate diameter of 1 mm (Sample 1, Trial 1).

The crystal removed from the seed measures approximately 25 mm. Small variations in diameter were observed along the growth axis. The pulses of material could be a result of system vibration or inconsistency in the melt itself that effected the flow of the compound through the thin capillary channel of the crucible.

Vibrations are hypothesized to be the primary source because they could be felt subtly along the weldment of the μ-PD chamber base and there was a slight vibration of the camera position which was mounted to the chamber lid.

The melt still contained within the crucible was also inspected and is shown in Figure 78. A large crystal had formed in the crucible and shows evidence of homogeneous mixing. From this we are able to conclude that our experimental temperature was appropriate for the compound. The yellow/green appearance was dramatically different from the white powders the experiment started with. A small portion of iridium also appeared to have precipitated onto the surface of the melt.

Pressed Powder: Sample 1, Trial 2

A 100 mm long Ce:LuAG crystal was grown at a rate of 0.5 $\frac{\text{mm}}{\text{min}}$ and is shown still attached to the seed in Figure 80. Discrepancies of the crystal diameter can be observed, similar to those observed in Trial 1. These undulations appear to come in at nearly regular intervals, smoothing out between each pulse of crystal.

The Ce:LuAG crystal was initiated on the same portion of the $Lu_3Al_5O_{12}$ seed as Trial 1. The top portion of the Ce:LuAG crystal separated from the crucible during cool-down, making removal easier.

Temperature was held steady for the entirety of the growth with the exception of the very end so any variability along its length is most likely not due to differences in temperature.

The left over melt is shown in Figure 79. The Ce:LuAG crystal formed within the crucible is smoother than after Trail 1 and appears to be homogeneously mixed.

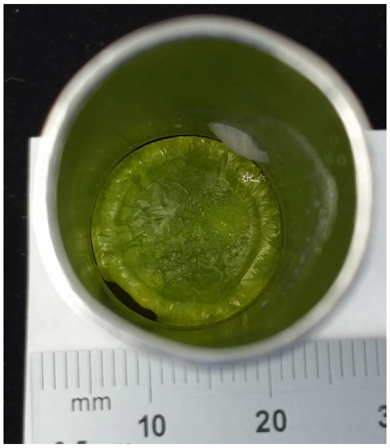

Figure 78: Remaining Ce:LuAG melt contained in the crucible (Sample 1, Trial 1).

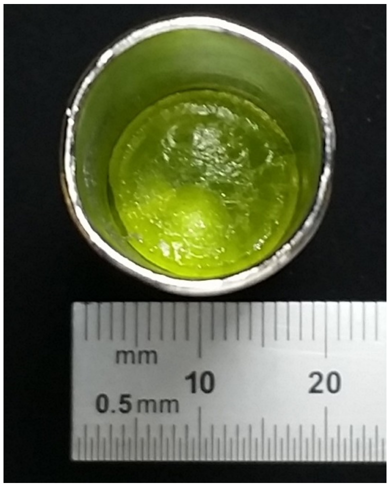

Figure 79: Smooth molten Ce:LuAG within crucible remaining after crystal growth (Sample 1, Trial 2).

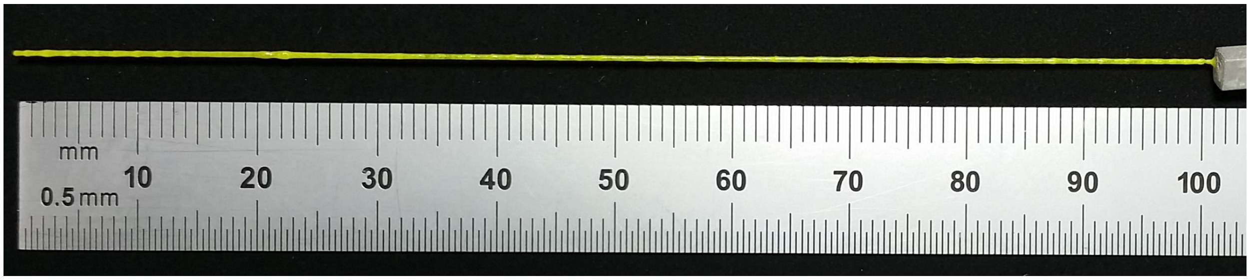

Figure 80: A 100 mm long Ce:LuAG crystal with an approximate diameter of 1 mm (Sample 1, Trial 2).

Pressed Powder: Sample 1, Trial 3

A 13 mm long Ce:LuAG crystal was grown at a rate of 0.1 $\frac{\text{mm}}{\text{min}}$ and is shown still attached to the seed in Figure 81. The most significant process change was a reduction in pull-down rate from 0.5-0.6 $\frac{\text{mm}}{\text{min}}$ of previous growths.

It is immediately apparent that the diameter of the slower drawn crystal is larger and more consistent. Another factor that may have attributed to this discrepancy in growth was a slight increase in temperature from 2068°C (SP: 48) to 2083°C (SP: 50).

Vibrations in the apparatus were also observed. This was evident in the slight movement of the seed and seed rod during the μ-PD experiment. Once the experiment was completed the seed holder collar that clamps the seed rod into place was cleaned thoroughly. This cleaning, however, was only slightly beneficial as the clamping resistance was still insufficient at preventing rotation of the rod in the holder.

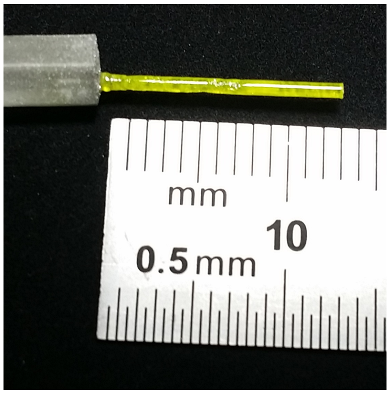

Figure 81: A 13 mm long Ce:LuAG crystal with an approximate diameter of 1 mm (Sample 1, Trial 3).

Pressed Powder: Sample 1, Trial 4

A 102 mm long Ce:LuAG crystal was grown at a rate of 0.1 $\frac{\text{mm}}{\text{min}}$. We were not able to exhaust the melt supply. It was also observed that the melt was contaminated with what appears to be iridium that precipitated from the crucible walls. The melt height only decreased by approximately 1 mm so it is assumed that the melt within the crucible contains bubble or is possibly hollow. The left over melt is shown in 82.

It was also observed that the previously stained quartz holder was now clean after approximately 16.5 hours at temperatures greater than 2000°C. This prolonged experiment along with the previous ones conducted with this melt and crucible caused the iridium to contaminate the melt in significant quantities. For this reason this crucible was abandoned for future growths. It was cycled again at higher temperatures upside-down in an effort to remove the crystal prior to chemical cleaning.

Figure 82: The Ce:LuAG crucible melt after crystal growth, contamination is observed on the top surface from the iridium crucible (Sample 1, Trial 4).

Pressed Powder: Sample 2, Trial 1

This crystal attempt was conducted on a new crucible with a larger capillary channel, measuring 3 mm OD at the nozzle with the capillary channel measuring 1.5 mm. This crystal had a much more difficult time seeding with the larger nozzle, likely due to the temperature gradient across the increased diameter of the attempted growth. The crystal was momentarily grown at a slower pull-down rate of 4 $\frac{\text{mm}}{\text{hr}}$ before the liquid melt pulled the seed rod out of the holder.

Figure 83: Crystallized Ce:LuAG melt within the crucible after growth attempt (Sample 2, Trial 1).

Once cooled back to RT the seed was successfully separated from the crucible. The seed had initiated at a much larger diameter than the previous growths. The melt had crystallized within the crucible as shown in Figure 83. The new iridium crucible was also slightly deformed after the experiment.

Pressed Powder: Sample 2, Trial 3

A 23 mm Ce:LuAG crystal was successfully grown at a rate of 0.1 $\frac{\mathrm{mm}}{\mathrm{min}}$ and is shown in Figure 85. The second experiment conducted on this sample was unsuccessful due to the bottom of the melt solidifying prior to initiating the seed. This third attempt was the first successful Ce:LuAG crystal growth with the larger diameter capillary channel. The larger size had presented challenges because the temperature gradient across the thick sample was more difficult to control, leaving less time to seed and a greater risk to separate from the melt prematurely.

Crystal discoloration was observed in all but near the initial seeding surface. This discoloration is not present in the other samples and is considered to be contamination introduced somewhere in process. This contamination is highlighted in Figure 84. It is hypothesized that the contamination occurred during the manual pressing of the sample and that the dark discoloration is due to carbon inclusion that was compacted into the sample under the high pressure of the press.

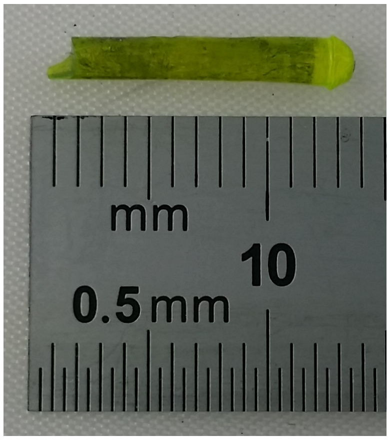

Figure 84: Initialization of the Ce:LuAG crystal at the right with contamination appearing as dark discoloration along the crystal exterior (Sample 2, Trial 3).

Due to the high temperatures and the repeated cycling on the after-heater and crucible, the two components were difficult to separate after the experiment. This was largely due to the deformation induced by the high temperatures where the iridium was not able to properly maintain its geometry. The crucible and after-heater were separated but broke suddenly apart with the after-heater striking the crystal still attached to the bottom of the crucible. The crystal broke but the other portion of crystal was recovered and is shown in Figure 85.

Future crystal growths with this larger diameter capillary channel will need to be controlled carefully. The temperature of the chamber was also higher for this crystal when compared to the smaller diameter crystals grown.

The temperature had to be increased further once the crystal began to grow because the diameter was steadily decreasing. The compensation seemed to stabilize the growth as observations from the finished crystal show a very consistent diameter thereafter. While difficult to grow, these crystals may be above a critical diameter where they are able to remain unaffected by the vibrations due to their additional mass.

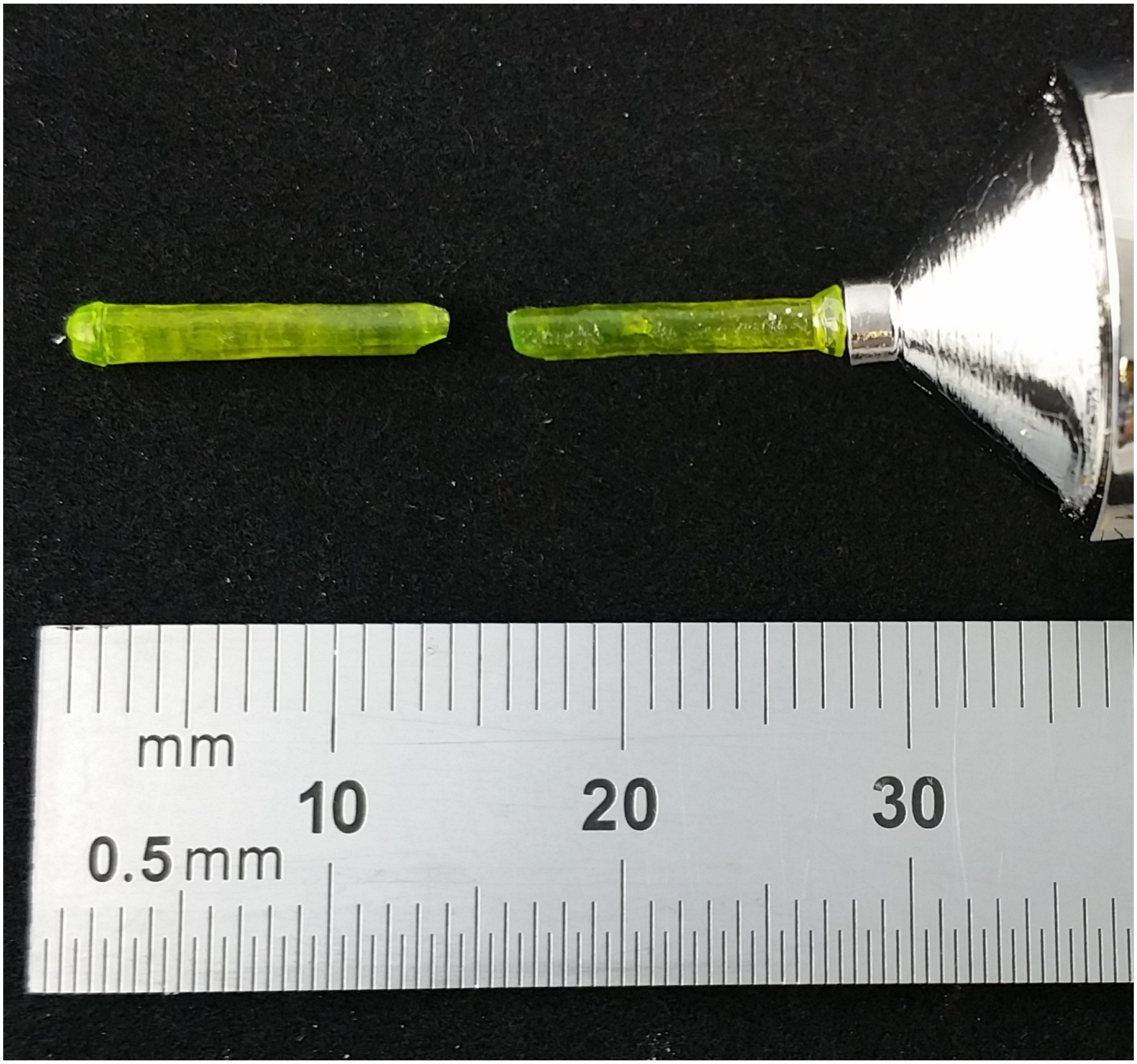

Figure 85: Ce:LuAG crystal growth was approximately 23 mm in length and was broken during after-heater removal (Sample 2, Trial 3).

Ce:LuAG Crystal Discussion

The lengths and weights of each Ce:LuAG crystal growth from Sample 1 are compared in Table 11.

Crystal	Pull-down Rate ($\frac{\text{mm}}{\text{min}}$)	Length (mm)	Weight (mg)	Ratio
Trial 1	0.60	25	31.4	0.80
Trial 2	0.50	100	114.1	0.88
Trial 3	0.10	13	37.7	0.34
Trial 4	0.10	102	330.0	0.31

Table 11: Ce:LuAG Sample 1 crystal comparison with length-to-weight ratio.

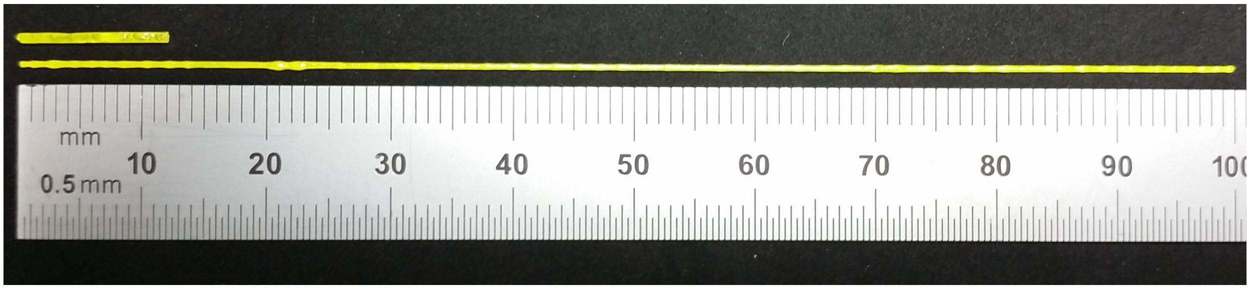

Figure 86: The 100 mm long Ce:LuAG crystal pulled at a rate of 0.5 $\frac{\text{mm}}{\text{min}}$ (Sample 1, Trial 2) compared to the shorter Ce:LuAG crystal grown at a rate of 0.1 $\frac{\text{mm}}{\text{min}}$ (Sample 1, Trial 3).

All four of these samples were drawn from the same melt and crucible/after-heater pair. While head pressure of remaining melt undoubtedly played a role in how easily the melt is seeded, the pull-down rate was found to be the most influential parameter to adjust to improve crystal quality. While the sample had been hydraulically pressed prior to the growths the sample could have benefited from possible sintering at higher temperature below the melting temperature. This type of sintering has been outlined in previous studies.[40]

The discrepancy in relative thickness is evident in Figure 86. The two Ce:LuAG crystals in the image were grown back-to-back under similar temperatures. The shorter Ce:LuAG crystal has a significantly larger diameter and is more consistent with its diameter than the longer, thinner Ce:LuAG crystal.

The longest Ce:LuAG crystals grown at fast and slow pull-down rates are compared in Figure 87. The slower pull-down rate grew a larger diameter crystal that was relatively consistent when compared to the faster grown crystal. The slow pull-down rate crystal from Trial 4 displayed what appeared to be a bubble after approximately 75 mm of growth. Bubbles are typically rare in μ-PD experiments because they tend to rise to the top of the melt. This was the first example of a bubble in any of our growths and they were not seen in our larger diameter grows with Sample 2 using the larger crucible nozzle diameter.

[40] B.C. Grabmaier, W. Rossner, and J. Leppert. Ceramic scintillators for x-ray computed tomography. *Physica Status Solidi (a)*, 130(2):K183–K187, April 1992

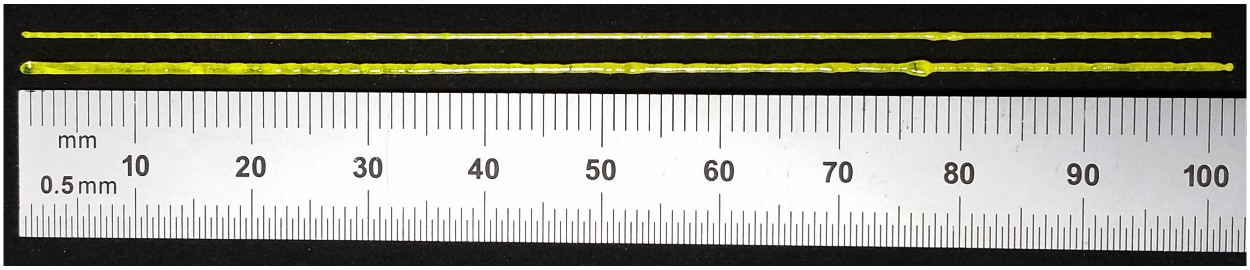

Figure 87: A 103 mm long Ce:LuAG crystal grown at 0.1 $\frac{\text{mm}}{\text{min}}$ (Sample 1, Trial 4) compared to a 100 mm long Ce:LuAG crystal grown at 0.5 $\frac{\text{mm}}{\text{min}}$ (Sample 1, Trial 2).

Crystal Results: $MgTa_2O_6$

The growth results of the $MgTa_2O_6$ crystals are summarized individually in this section along with details and additional observations. Results are summarized in Table 12.

Experiment	Sample Type	Sample/Trial	Initial Size	Length (mm)
1	NP	1 / –	5 g	–
2	NP	1 / 1		–
3	NP	1 / 2		–
4	NP	1 / 3		15
–	MP	2 / –	$\ll 5$ g	–
5	MP	3 / 1	5 g	–
6	MP	3 / 2		–
7	MP	3 / 3		32
8	MP	4 / 1	10 g	8
9	MP	4 / 2		–
10	MP	4 / 3		12
11	MP	4 / 4		136
12	MP	4 / 5		47

Table 12: Results summary for $MgTa_2O_6$ μ-PD growths. Sample type is the method of preparation which was either non-pressed (NP) or manually-pressed (MP).

No experiments were conducted with Sample 2 because of concerns over excessive sample loss while manually pressing the sample. Sample 3 was made shortly after and the powder procedure was adjusted to prevent excessive sample loss again. This sample retained much of its mass and was used in subsequent μ-PD experiments. Trial

Loose Powder: Melt Check

A melt check was performed on the $MgTa_2O_6$ compound before attempting any μ-PD experiments. This check was to ensure that the compound was relatively compatible with the iridium crucible.

This compatibility is critical at the capillary channel leading down to the crucible nozzle. If the melt resists the iridium sufficiently it will not travel down the channel, if the channel is too wide we risked free flow of the melt from the crucible once it liquefies.

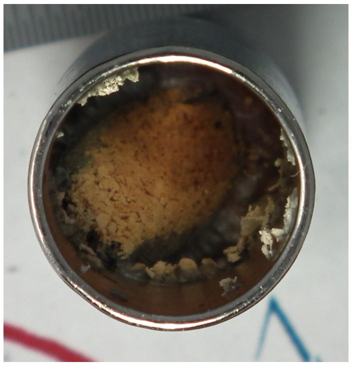

Figure 88: Top of crucible, melt test for $MgTa_2O_6$ (Sample 1).

From the melt check we were able to confirm that the melt flowed down the capillary channel and emerged from the nozzle where it was held in place for a period of time without interaction from the seed. Once the melt compound was confirmed to be stable in this position the chamber was cooled to RT. After the check was complete the remaining melt in the crucible was inspected and is shown in Figure 88. The powder sample used was uncompressed and the top of the melt within the crucible appeared to be not completely melted and appeared orange-brown in color. The melt that had emerged from the crucible nozzle slightly was white and smooth in appearance. This change in color implies a significant temperature gradient across the sample and will be monitored in future growth attempts.

Loose Powder: Sample 1, Trial 1

This first μ-PD experiment failed due to a misalignment between the seed and the crucible nozzle. Despite the lack of growth attempt several observations were made post-experiment.

After the μ-PD experiment was performed it was observed that the quartz pedestal had a blue discoloration. This was believed to be from the not completely dried alumina adhesive that was used to construct the seed rod. This discoloration is shown in Figure 90.

Another possible source of this discoloration could have been from the MgO evaporating off of the melt and falling as precipitate onto the quartz tube. This phenomena has been observed in similar μ-PD experiments when magnesia ceramics are used instead of alumina.[41] The alumina paste seems more likely as the melting temperature of MgO is significantly higher than our desired compound and the constitutive compound.

The melt left inside the crucible after the μ-PD experiment was inspected. No single crystals formed in the melt and the melt appeared to take two different colors, its chalky white appearance was similar to that of the powder entering the chamber and the orange portions of the sample seemed to have changed color due to excessive heat. it did show improvements over the still powdery surface of the melt after the melt check.

Loose Powder: Sample 1, Trial 2

This second μ-PD experiment was properly aligned but did not produce any growth. The melt had difficulty interacting with the seed and would not attach to initiate growth.

After the experiment it was observed that the entirety of the compound had been more uniformly heated and appeared molten as shown in Figure 91.

The seed was removed and sanded with 600/P1200 grit grind-

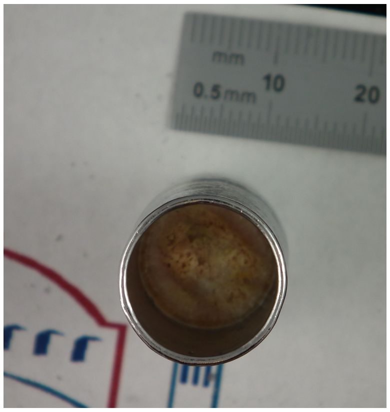

Figure 89: Semi-smooth molten $MgTa_2O_6$ within crucible after the μ-PD experiment (Sample 1, Trial 1).

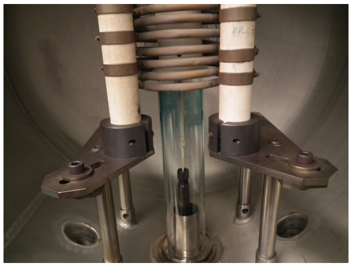

Figure 90: Blue discoloration on quartz pedestal after seed attempt (Sample 1, Trial 1).

---

[41] T. Fukuda and V.I. Chani. *Shaped Crystals: Growth by Micro-Pulling-Down Technique*. Springer-Verlag, first edition, 2007

ing paper to create a more uniform tip, however the groove in the middle of the seed was deep and was only partially compensated. This was done in an effort to improve the interactions between the emerging melt and seed surface.

The crucible was also sanded with 600/P1200 grit grinding paper so that all excess compound directly outside of the capillary channel was removed. The crucible nozzle was sanded such that the iridium circumference was visible. Some of the melt was also removed from the outside of the capillary channel.

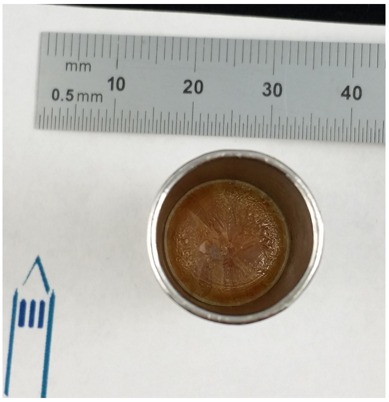

Figure 91: Smooth molten $MgTa_2O_6$ melt within crucible (Sample 1, Trial 2).

Loose Powder: Sample 1, Trial 3

This attempt marked the first successful growth of $MgTa_2O_6$. The $MgTa_2O_6$ crystal within the μ-PD chamber is shown in Figure 92.

The temperature gradient is largely responsible for the color gradient. A critical scintillator property is transparency and while the majority of this growth ranged in color from dark brown to light orange the very end of the growth was white and slightly transparent. It was the goal of subsequent μ-PD experiments to reproduce the transparent white portion of the crystal.

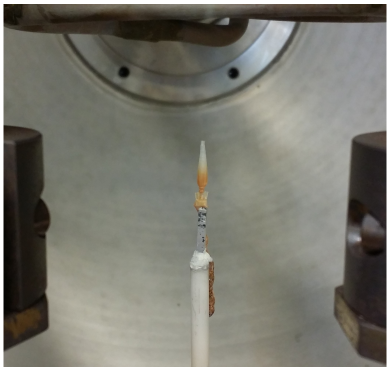

Figure 92: Lowered $MgTa_2O_6$ crystal within test chamber, below induction coil (Sample 1, Trial 3).

This growth marked the third and final test from the five gram, powder sample. This sample was not pressed and was placed within the crucible in its powdered form. The previous growth attempts with this sample failed to seed.

The crystal was successfully removed from the apparatus and is shown in Figure 94. This portion of the growth was the focus of further testing as it possessed a more uniform and ordered growth when compared to other experiments to follow.

The initial discharge of the melt free flowed from the capillary channel and was of a darker color which correlated to the higher experimental temperatures. This large mass free flowed from the crucible at a temperature of 1972°C (SP: 36.8). The temperature of the chamber was reduced and the color lightened to white. This yellow-brown color was also observed on the melt surface that was still within the crucible after the experiment.

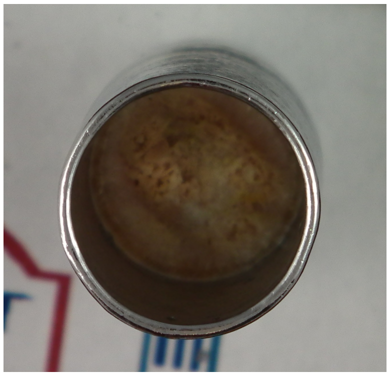

Figure 93: The $MgTa_2O_6$ melt within crucible after the μ-PD experiment (Sample 1, Trial 3).

While some sample remained within the crucible no further testing was completed using this sample. In the interest of time another sample was prepared that was pellet pressed with the thought that this would improve the bonds in the powder prior to μ-PD, leading to a more organized and improved growth when compared to these trials of simply experimenting with loose powder.

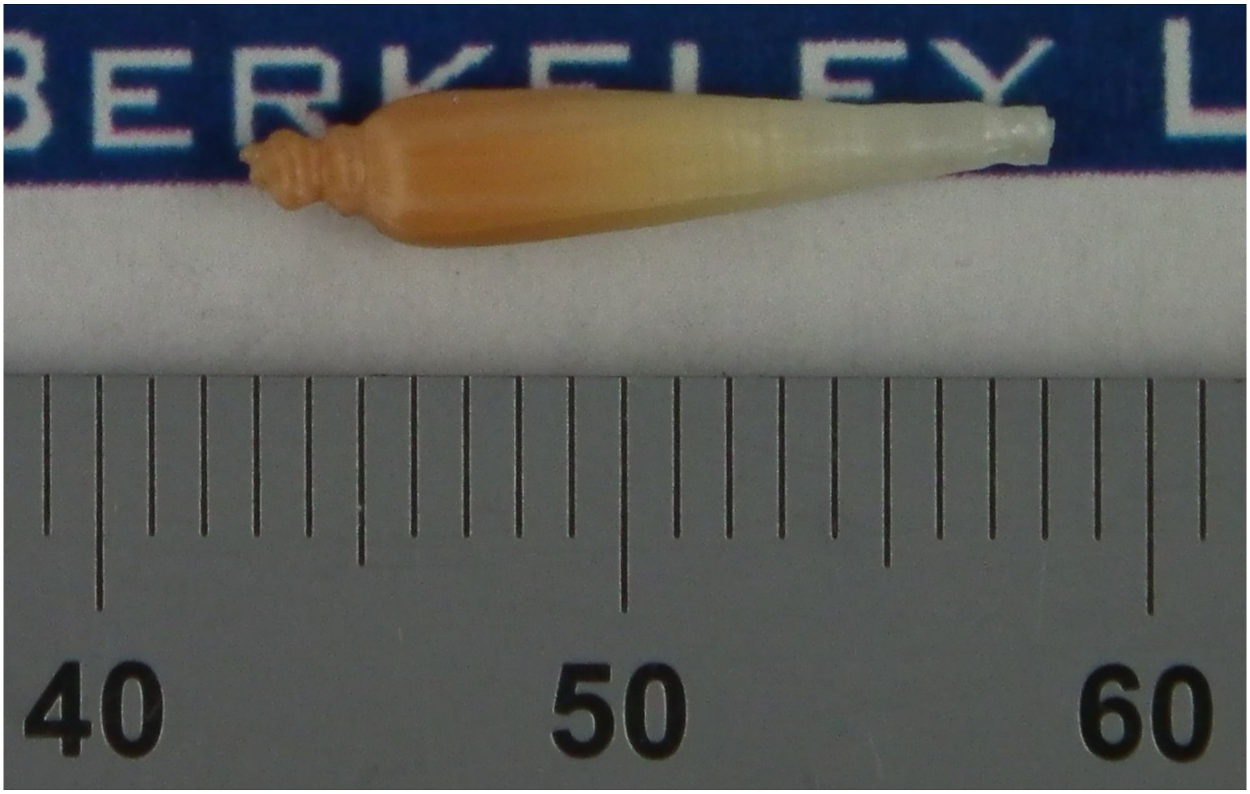

Figure 94: $MgTa_2O_6$ crystal growth (Sample 1, Trial 3).

Pressed Powder: Sample 3, Trial 3

Sample 2 was not used for μ-PD experiments due to a significant loss of compound during the manually press process. For this reason μ-PD began again with Sample 3. Trial 1 and 2 with this sample continued to have the compatibility issues we have seen previously between the seed and the emerging melt. Trial 3 with this sample did produce a growth that was largely uncontrolled but could be used as a seed in subsequent μ-PD experiments.

The $MgTa_2O_6$ growth is shown in Figure 95. This discharge was largely unorganized and free flowed from the capillary channel. This growth, as with the last, did not seed easily with the iridium seed. Instead, the melt avoided contact and grew around it after solidification initiated on the ceramic seed rod below. Both Trial 1 and 2 with this sample failed to seed and this was the first actionable growth achieved from this sample.

This free flow also exhausted the melt and was therefore the last trial with this sample. Since the growth was not orderly and arranged stoichiometrically it is not being characterized as a single crystal, also lacking the anticipated transparency that was visible slightly at the end of our μ-PD experiment on Sample 1, Trail 3. It was also observed that the ceramic insulator and lid were darkened after the experiment, implying that one of the

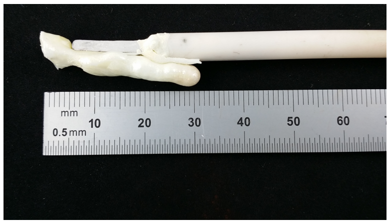

Figure 95: $MgTa_2O_6$ discharge attached to the seed rod, avoiding contact with the seed (Sample 3, Trial 3).

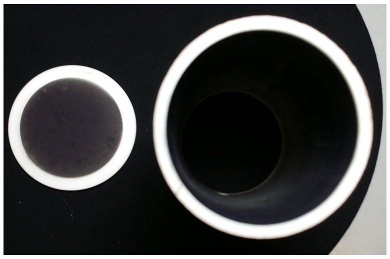

Figure 96: Compound deposit on surrounding ceramic insulator and lid (Sample 3, Trial 3).

compounds may have evaporated off during the growth attempt. With the sample exhausted there is no concern of this effecting the quality of subsequent crystal growths.

The crucible and after-heater were subjected to 2 hours at experimental temperatures in an effort to clean the pair of any residual compound. These blackened ceramics were also added with the lid slightly askew with the hope that the compound would burn off similar to what we saw with the blue discoloration of the quartz tube. This effort did not yield an appreciable improvement and new ceramic insulators were used in subsequent μ-PD experiments as a precaution.

Pressed Powder: Sample 4, Trial 1

A new ten gram pressed powder sample was prepared and used for the first time in this μ-PD experiment. A new seed had been constructed from the previous growth and dramatically improved compatibility over its iridium counterpart used previously.

The larger sample and the fact that it was densified prior to the experiment seemed to make growth easier than previous attempts. The remaining melt in the crucible was white at the center and discolored yellow along the perimeter as shown in Figure 97. This appearance was different from the darker discoloration we had observed with the loose powder sample.

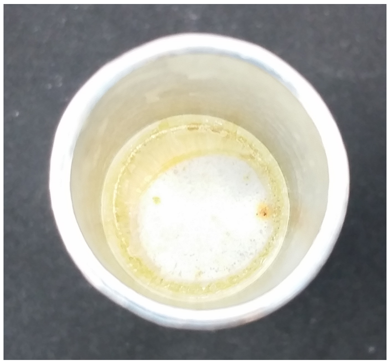
Figure 97: The $MgTa_2O_6$ melt within crucible after the μ-PD experiment (Sample 4, Trial 1).

Another improvement was using $MgTa_2O_6$ as the seed material rather than pure iridium. The only growth that was completed with the iridium seed was free flow that fortunately enough attached itself to the seed rod and Zirconia adhesive. This growth marked the first that seeded correctly to the seed and proceeded to form on that surface largely due to this improved compatibility. The growth is shown in Figure 98.

The 8 mm long growth did not appear to be overheated and was evenly white throughout, however, the growth formation was rather unorganized and required restart at several points where the diameter of the crystal reduced until separation occurred. The temperature had been increased to compensate but this risked free flow of the compound from the capillary channel.

To avoid this, we began to hold the seed against the crucible nozzle and let the two acclimate for an extended period of time before the seed was brought down. This allowed us to increase the temperature further and ensure that the capillary channel was filled with compound prior to pull-down. A drawback of this was that the surface of the seed was visibly melting at times, being the same material, it was subject to the same temperatures.

Another source of the diameter fluctuations was the vibrations from the system. This compound was much more fluid than the Ce:LuAG crystals tested so the impact on the solidifying crystal was most likely more significant. This coupled with temperature adjustments while the crystal was growing compounded more diameter variability.

Pressed Powder: Sample 4, Trial 3

This attempt marked the third μ-PD experiment on this sample. Trial 1, had produced a small growth measuring approximately 8 mm and Trial 2 had seeded at a very small diameter and quickly expanded. When the growth required reseeding the melt pulled the small already formed growth from the seed. Due to the low temperature of the underside of this growth reseeding failed.

On this attempt a slightly larger growth was achieved and is shown in Figure 100. This growth measured approximately 12 mm, slightly longer than the first growth. This growth experienced moments of free flow from the crucible nozzle that coated the seed and seed rod. These free flow events were corrected with reduction in temperatures.

Temperature adjustment were also needed while growth was in progress and the resulting growth shows the same variable diameter that Trial 1 displayed. The temperatures were nearly identical with many of the same problems contributing to variability in both experiments.

Pull-down rates were kept relatively slow at 0.10 $\frac{\text{mm}}{\text{min}}$, adjustment from this value in either direction was met with difficulty. If the rate of pull-down was slowed further the growth would solidify after a shorter and shorter distance below the crucible nozzle resulting in eventual termination of the growth. If the rate was increased, the seed would outpace the emerging melt, the meniscus would be extended and would eventually separate. Due to process sensitivity any adjustment in pull-down rate needed to be coupled with an adjustment in temperature to maintain an appropriately large meniscus.

The melt remaining in the crucible is shown in Figure 99. The appearance is similar to that of Trial 1 with the interior the white color of the original powders and the perimeter discolored yellow. Two spots in the melt were a darker orange and may have been precipitated contamination from the experimental apparatus.

Figure 98: The 8 mm $MgTa_2O_6$ growth attached to the newly constructed $MgTa_2O_6$ seed (Sample 4, Trial 1).

Figure 99: The $MgTa_2O_6$ melt inside the crucible (Sample 4, Trial 3).

Figure 100: The 12 mm $MgTa_2O_6$ growth attached to the newly constructed $MgTa_2O_6$ seed (Sample 4, Trial 3).

Pressed Powder: Sample 4, Trial 4

This μ-PD experiment produced the longest single growth of any experiment, measuring 136 mm. The growth in its entirety is shown in Figure 101 prior to removal. This growth had been left to run overnight at a pull-down rate of 0.50 $\frac{\text{mm}}{\text{min}}$.

Several points along the growth length were extremely small and the growth was broken up prior to removing it from the chamber as it was unlikely the growth could tolerate any handling in its full form. Despite this controlled breakup, another portion of the growth broke free and fractured into several pieces. These pieces were collected and are shown in Figure 102.

This experiment marked an important step forward in the process. A majority of the growth grew unsupervised and consequently grew without parameter adjustment. This μ-PD experiment differed from previous attempts by running at a higher temperature and a higher pull down rate. The majority of this growth experiment was run at a temperature of 1954°C (SP: 35) where the other experiments were run at a maximum temperature of 1911°C (SP: 31). This increase in temperature needed to be coupled with an increase in pull-down rate. The pull-down rate was increased to 0.50 $\frac{\text{mm}}{\text{min}}$ while previous attempts used a rate of 0.10 $\frac{\text{mm}}{\text{min}}$.

The growth experienced diameter fluctuations similar to previous growth attempts despite the parameter adjustments. This lends more evidence to the μ-PD chamber experiencing vibration issues that have been seen in both $MgTa_2O_6$ and Ce:LuAG experiments.

Prior growths had required several temperature adjustments during the growing process making it difficult to determine what events were causing the changes in diameter and in color. For this growth the temperature was kept constant and this is evident by the more uniform color of the growth. There was a gradient across the diameter of the growth where parts of the growth had broke the color appeared whiter on the interior. This implies a temperature gradient across the diameter of the growth where the exterior temperatures of the growth were hotter than the interior. While this makes intuitive sense it is a concern at the apparent severity of this gradient, implying that growth of this compound could remain difficult with the current capillary channel diameter, which is already small (> 1 mm).

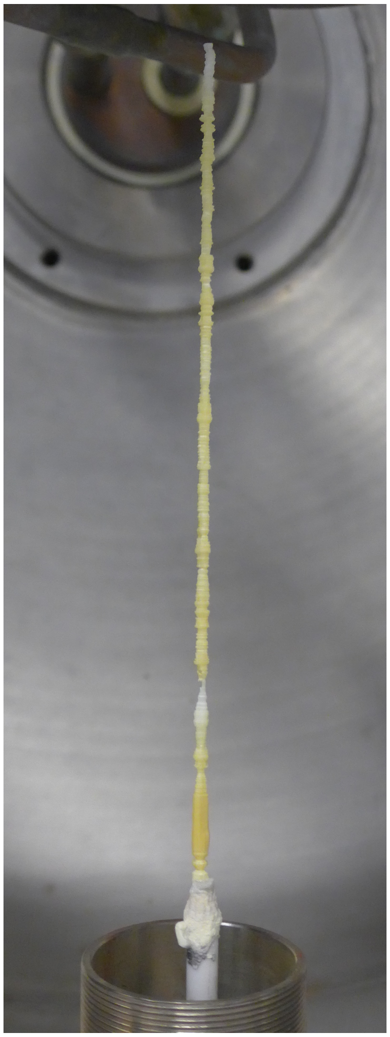
Figure 101: The 136 mm $MgTa_2O_6$ growth attached to the seed still in the μ-PD chamber (Sample 4, Trial 4).

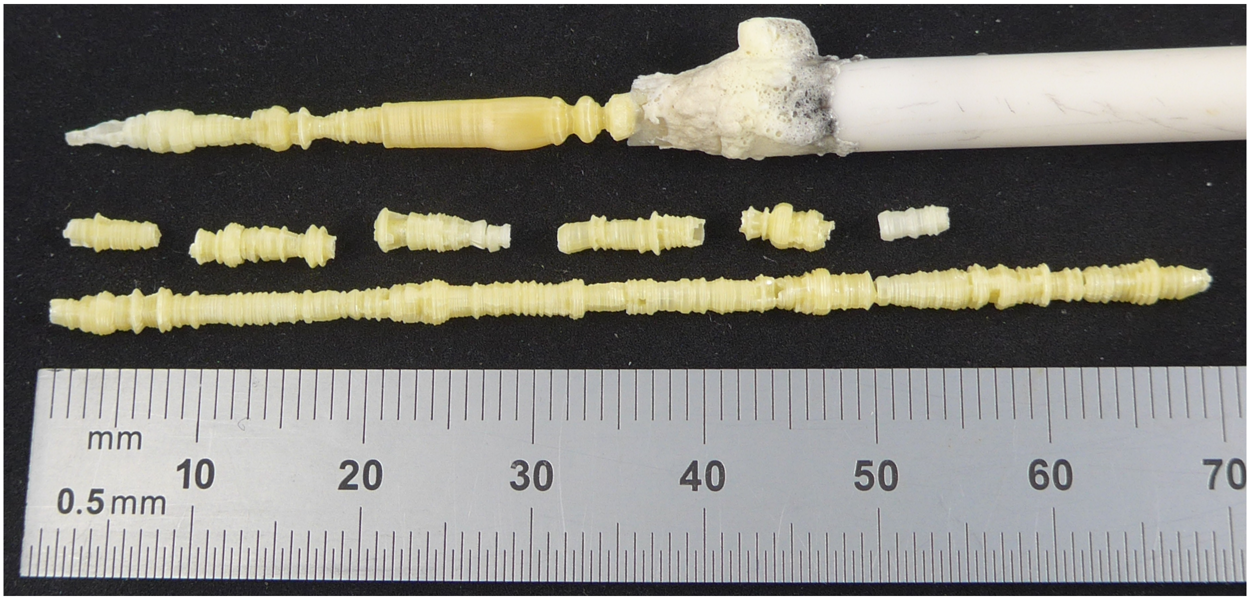

Figure 102: Broken up $MgTa_2O_6$ growth, measuring 136 mm total (Sample 4, Trial 4).

Pressed Powder: Sample 4, Trial 5

This μ-PD experiment produced a growth of 47 mm. The growth in its entirety is shown in Figure 105. Like the previous attempt the chamber temperature was increased to 1954°C (SP: 35) and the pull-down rate was set to 0.50 $\frac{\mathrm{mm}}{\mathrm{min}}$. One important experimental difference was that these two experiments were conducted from the same sample. This growth had the least amount of head pressure of any of the experiments on this sample for that reason. The growth is measured and shown in greater detail in Figure 105.

A similar growth strategy of obstructing the crucible nozzle with the seed was employed for this experiment. Some difficulty was encountered when the melt began to wet severely on the exterior of the crucible nozzle, this was followed by a period of free flow that removed the melt from the exterior of the nozzle completely and resulted in a large mass depositing around and over the $MgTa_2O_6$ seed. It was on this new surface that the growth began which provided a large smooth surface in which to initiate growth. As with the previous growth the beginning was noticeably larger in diameter before tapering off. Upon removal the sample appeared noticeably whiter than our previous growth at this temperature and pull-down rate which may be a product of the slightly undersized average diameter.

The melt remaining in the crucible is shown in Figure 103. Here it is observed what appears to be iridium contamination from the crucible itself which appears as silver spots on the top surface of the melt. This along with the generally changed appearance of the crucible exterior implies that the crucible may have contaminated the crystal formation.

Due to the numerous experimental cycles and extended time at elevated temperatures the grain structure of the iridium crucible became more pronounced and is shown in Figure 104. In addition to the grain structure observations one can also observe the wetting properties of the $MgTa_2O_6$ compound on the exterior of the crucible, where the melt has traveled upwards along the crucible exterior. This remained even after the majority of this wetted compound had joined the growth once the pull-down program was initiated.

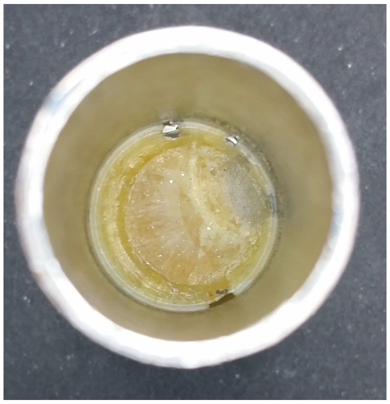

Figure 103: $MgTa_2O_6$ melt within the crucible, suspected contamination from the iridium crucible (Sample 4, Trial 5).

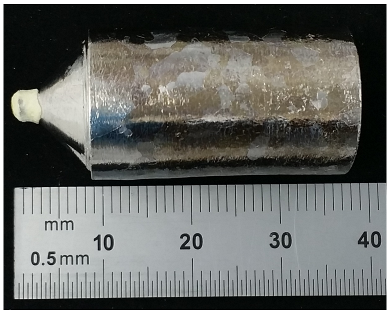

Figure 104: The exterior of the crucible after the μ-PD experiment, grain boundaries prominent after high temperature cycling (Sample 4, Trial 5).

Figure 105: Broken up $MgTa_2O_6$ growth (Sample 4, Trial 5).

X-ray Powder Diffraction

Multiple $MgTa_2O_6$ samples were prepared periodically during testing to ensure that we were working with the correct phase of the compound. No Ce:LuAG samples were tested using this method, instead XRL was used to characterize and compare the crystals to published values. XRPD testing was performed on the loose $MgTa_2O_6$ powder, after the melt check, and on subsequent growths. These results are outlined below and compared against the $MgTa_2O_6$ standard peaks provided by the Match!, a phase identification program created by Crystal Impact.

$MgTa_2O_6$: Sample 1, Powder

In order ensure that we were starting with the correct compound a sample of the loose powder was taken to perform XRPD. This test was done prior to running the melt check with the synthesized compound. The results of this test are shown in Figure 106, against the standard $MgTa_2O_6$ sample peaks.

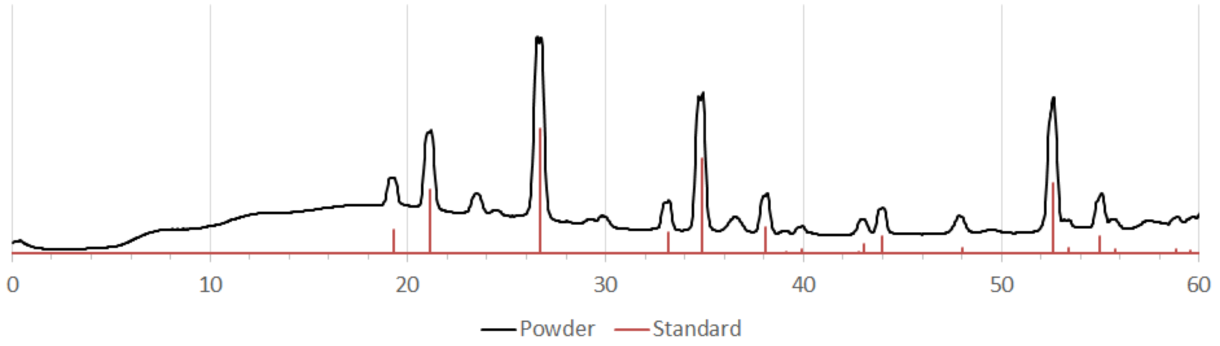

Figure 106: Diffraction pattern taken from the $MgTa_2O_6$ powder sample prior to running the melt check compared against the peak standard (Sample 1).

The sample peaks show good correlation to the standard and we can conclude that our powder synthesis was successful. The results did have a significant amount of noise for the lower values. After some investigation it was determined that the sample simply used a different type of tape to adhere the powder to when compared against the NaCl standard used to calibrate the resulting diffraction pattern. This was corrected in subsequent XRPD tests.

$MgTa_2O_6$: Sample 1, Melt Check

A melt check was performed to ensure that the iridium crucible and the $MgTa_2O_6$ compound were compatible enough to produce conditions in which a crystal could be formed. From in-situ observations we were able to confirm this capability as melt emerged from the end of the crucible nozzle. After the test, a sample of the powder was taken from the crucible and tested. The results of this test are shown in Figure 107.

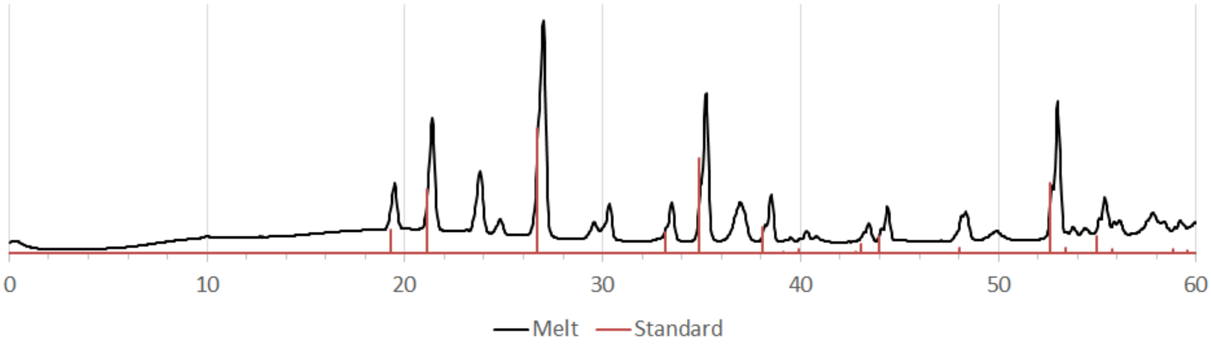

Figure 107: Diffraction pattern taken from the $MgTa_2O_6$ melt after completing the melt check, compared against the peak standard (Sample 1).

The compound has good correlation to the standard peaks and the noise from the lower values has been reduced by running a more appropriate calibration.

$MgTa_2O_6$: *Sample 1, Trial 3*

Two samples were taken and pulverized for XRPD testing on Sample 1, Trial 3. These regions are highlighted in Figure 108. Two samples were take because the color of the melt changed significantly as it solidified and the temperature gradient stabilized to a lower temperature. The dark brown mass, labeled the head region because it was first to exit the crucible, was of interest because of its color. We needed to ensure that multiple phases did not exist in the sample and that we were not loosing a constitutive compound at high temperature. The second region, labeled the tail was lighter in appearance and transparent at the end. This sample was not taken from the ordered growth at the far left of Figure 108 because this would be tested later with XRL.

These output profiles are shown in Figure 109 and Figure 110. Once photographed the two components were separated and ground for x-ray diffraction testing.

Each of the sampled diffraction match closely with that of the standard sample pattern.

Figure 108: Highlighted regions of $MgTa_2O_6$ growth where XRPD samples were taken (Sample 1, Trial 3).

$MgTa_2O_6$: *Sample 3, Trial 3*

After Sample 3, Trial 3 a free flow growth of consist white appearance was formed. This discharge was large enough to produce a new seed out of and a XRPD was taken from the unused portion to confirm that the seed used in subsequent experiments was in fact identical to the compound we were wishing to grow. This would ensure compatibility with the melt in future growths.

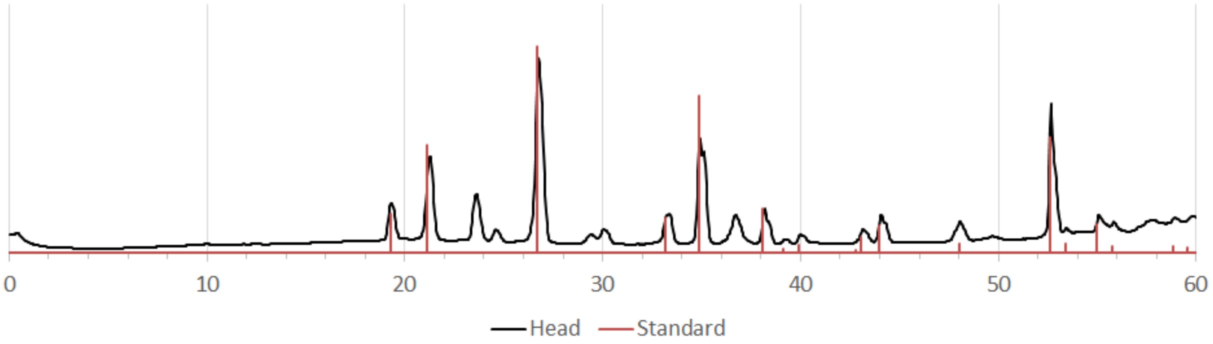

Figure 109: Diffraction pattern taken from the $MgTa_2O_6$ head region compared against the peak standard (Sample 1, Trial 3).

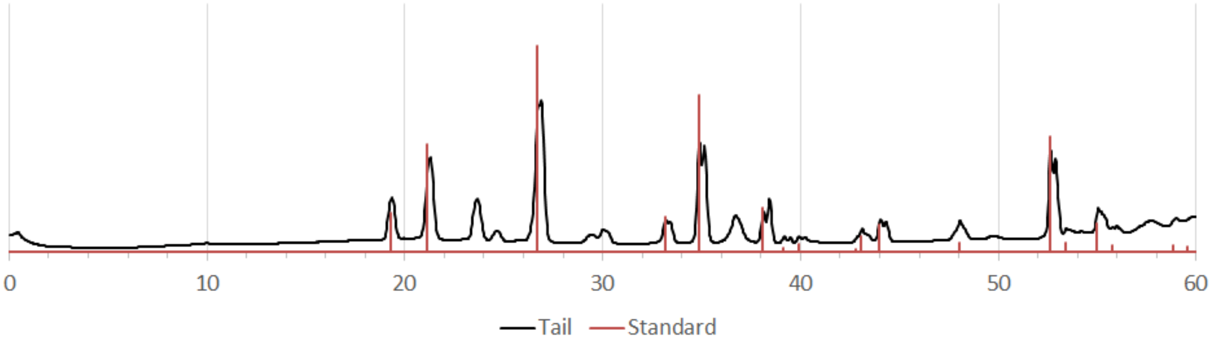

Figure 110: Diffraction pattern taken from the $MgTa_2O_6$ tail region compared against the peak standard (Sample 1, Trial 3).

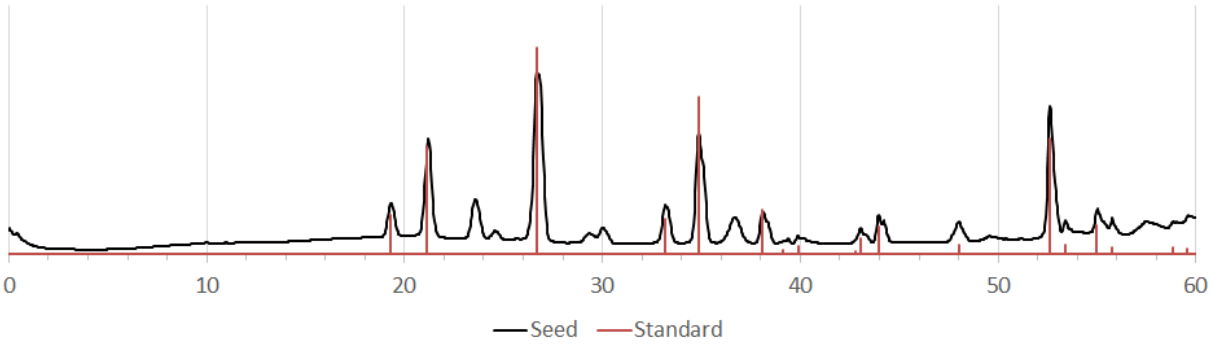

Figure 111: Diffraction patterns taken from the $MgTa_2O_6$ growth used for as a seed compared against the peak standard. (Sample 3, Trial 3).

The seed showed good correlation with the standard $MgTa_2O_6$ peaks and we concluded that we had a seed made of the desired compound. With this confirmation we moved forward with other μ-PD experiments.

X-ray Luminescence

X-ray luminescence (XRL) testing was performed on both the Ce:LuAG and $MgTa_2O_6$ growths. This test required larger sample sizes to be broken up and stacked in glass vials so like growths were combined for testing the Ce:LuAG samples. The $MgTa_2O_6$ growths were also combined in one case and the tail growth highlighted in Sample 1, Trial 3 was tested by itself.

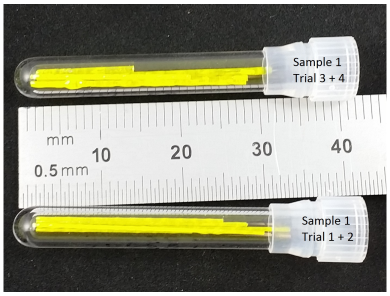

Figure 112: Ce:LuAG crystals prepared for XRL testing, Sample 1, Trial 3+4 (top) and Sample 1, Trial 1+2 (bottom).

Ce:LuAG : Sample 1, Trial 1 + 2

The samples prepared for XRL testing are shown in Figure 112. Trial 1 and 2 were combined because they were grown at similar pull-down rates of 0.6 $\frac{\text{mm}}{\text{min}}$ and 0.5 $\frac{\text{mm}}{\text{min}}$ respectively. These two crystal growths were significantly different lengths, there general structure and diameters were nearly identical. For this reason these samples were combined to perform x-ray luminescence testing. The resulting output spectrum is shown for these smaller diameter growths in Figure 113. These values for the peak emission spectra match published values for this compound.[42]

The peak emission of this combined sample was at 547 nm, well into the visible range and would be green-yellow in appearance. These growths were also characterized by relatively fast pull-down rates in the range of 0.5-0.7 $\frac{\text{mm}}{\text{min}}$. It was determined that this was the most influential factor that determined overall crystal growth diameter. The relatively faster pull-down rate resulted in smaller diameter crystals when compared to a slower pull-down rate.

Ce:LuAG : Sample 1, Trial 3 + 4

Due to the relatively small sizes and similar appearance of Trial 3 and 4, these samples were combined to perform XRL testing. These two crystals were grow to significantly different lengths but shared similar diameters and appearance due to their identically slower pull-down rates of 0.1 $\frac{\text{mm}}{\text{min}}$. The resulting output spectrum is shown in Figure 114.

The peak emission of this combined sample was at 547 nm, well into the visible range and would be green-yellow in appearance. The relative intensities taken from each test group are compared in Figure 115.

[42] T. Yanagida, Y. Fujimoto, Y. Yokota, K. Kamada, S. Yanagida, A. Yoshikawa, H. Yagi, and T. Yanagitani. Comparative study of transparent ceramic and single crystal Ce doped LuAG scintillators. *Radiation Measurements*, 46(12):1503–1505, 2011

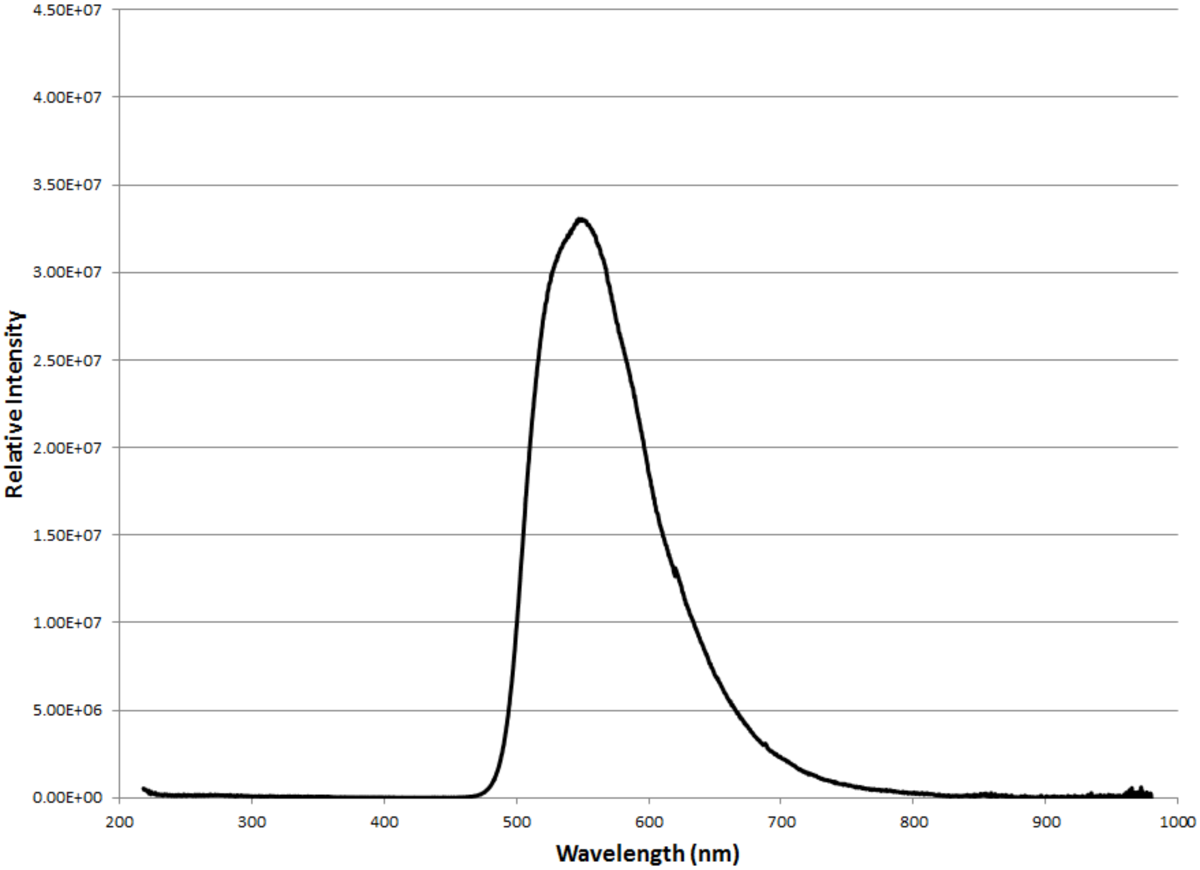

Figure 113: XRL intensity for the combination of Ce:LuAG crystal growths from Sample 1, Trial 1+2.

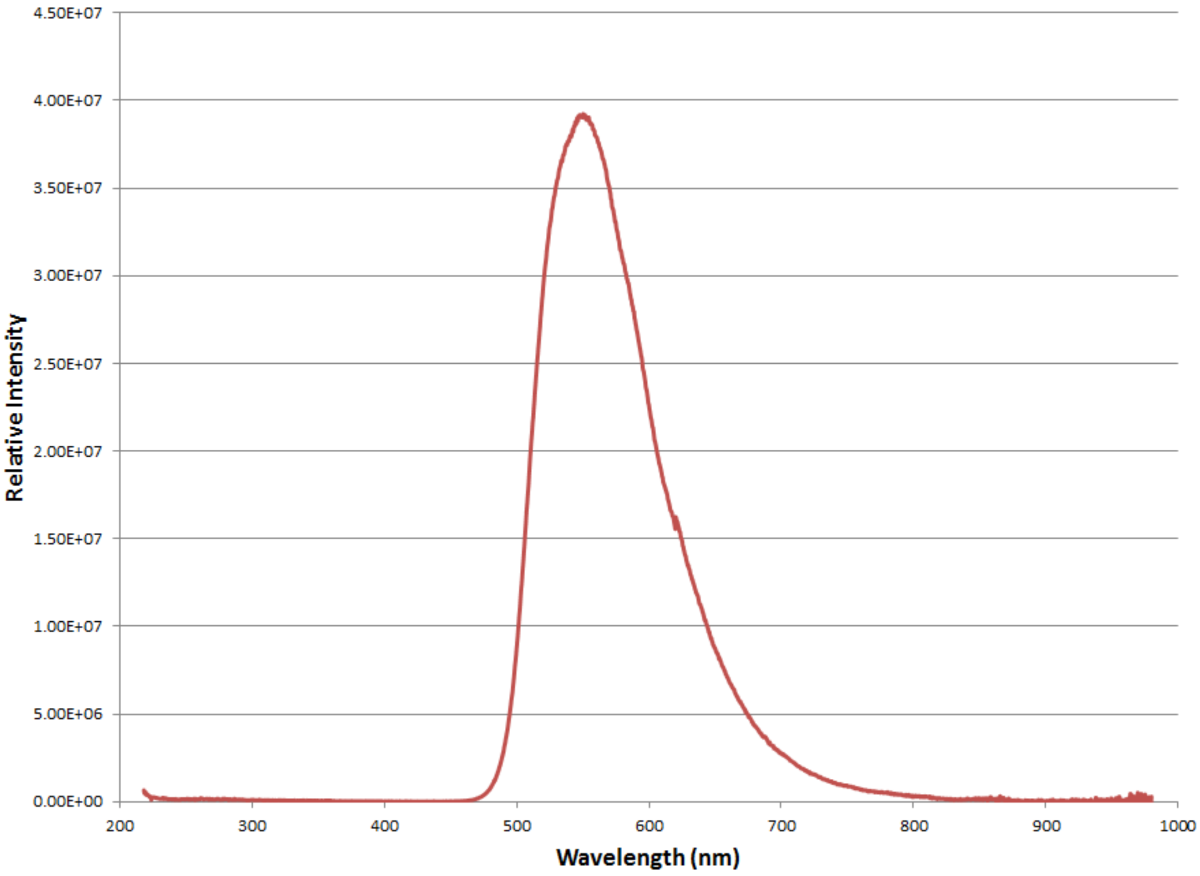

Figure 114: XRL intensity for the combination of Ce:LuAG crystal growths from Sample 1, Trial 3+4.

As expected the relative intensity peaks around the same wavelength. The thicker diameter samples had a stronger intensity when compared to the thinner diameters samples. This most likely has more to due with the larger crystal volume used in the test rather than the density of the individual crystals being significantly different. The peak emission values from both sample groups are then compared to published values in Table 13.

Publication values either explicitly stated the dopant, Ce, concentration at 1 mol% or omitted the concentration entirely. The measured values are on the high end of the spectrum for Ce:LuAG but they are within the expected visible range.

Source	Peak Emission (nm)
[38]	520
[56]	500-550
[65]	520
[71]	510
[73]	530
Trial 1+2	547
Trial 3+4	550

Table 13: Peak emission values from publications compared to the experimentally grown Ce:LuAG crystals.

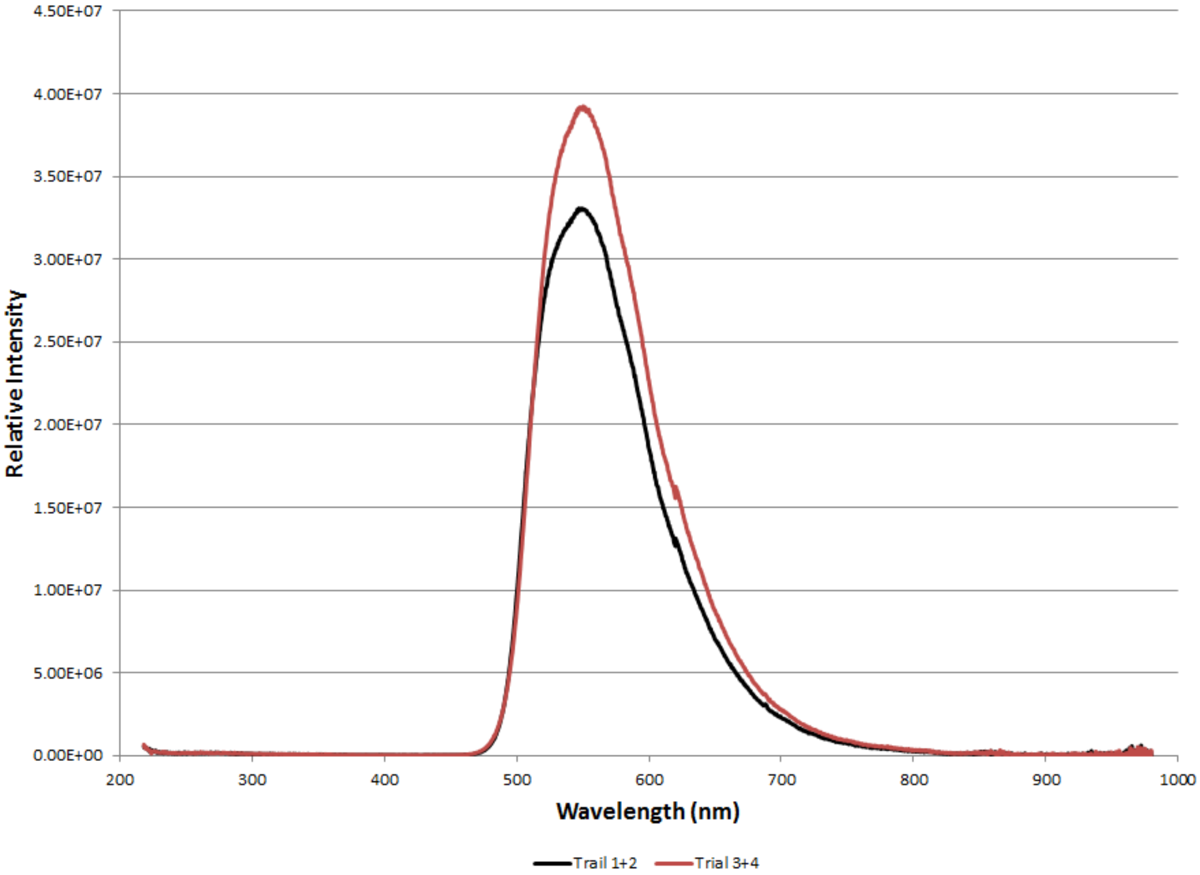

Figure 115: XRL intensity comparison for the combination of Ce:LuAG crystal growths from Sample 1, Trial 1+2 and Sample 1, Trial 3+4.

$MgTa_2O_6$: Sample 1, Trial 3

The tail portion of the $MgTa_2O_6$ growth from Sample 1, Trial 3 was analyzed because of its ordered appearance and was not mixed with any other XRL samples. The XRL results are shown in Figure 116.

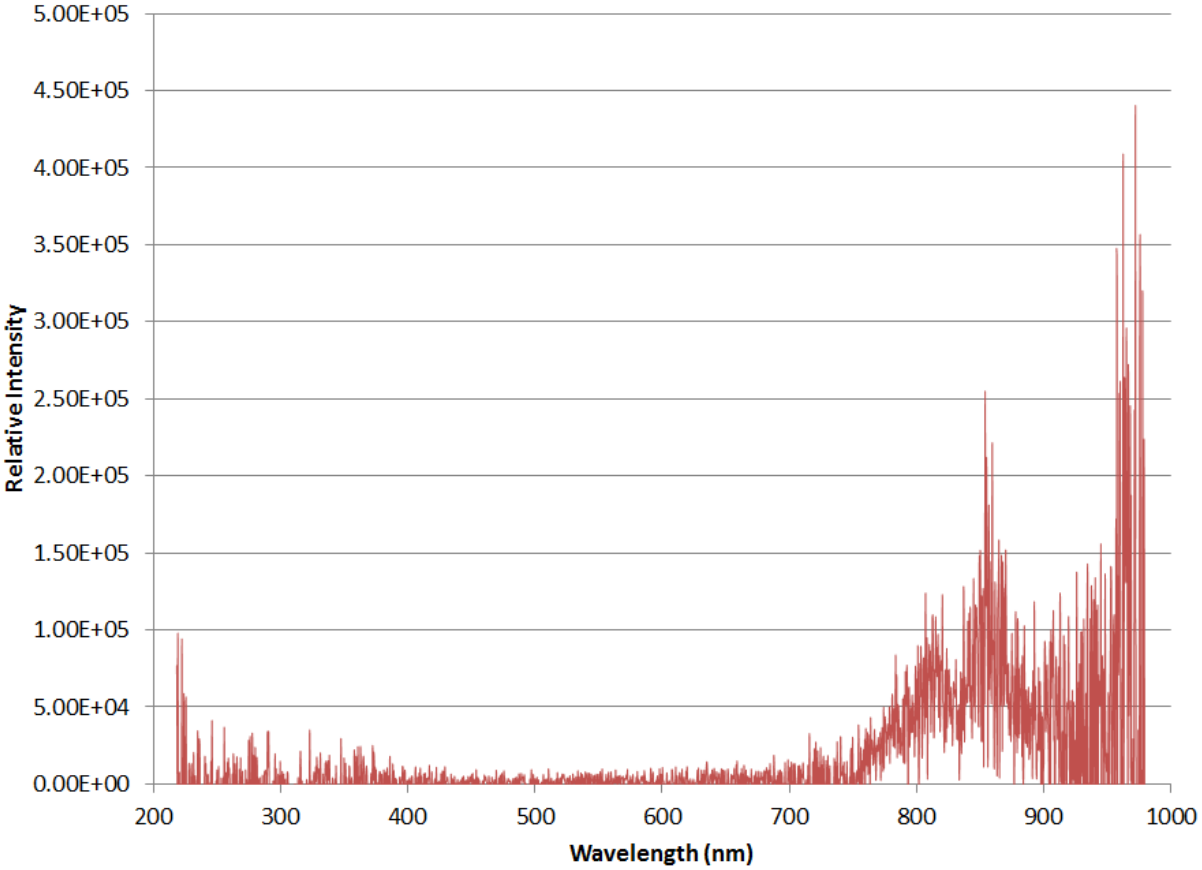

Figure 116: XRL intensity for the tail portion of the $MgTa_2O_6$ growth (Sample 1, Trial 3).

The relative intensity values from this sample are extremely low. While there appears to be an emission peak around 850 nm and 980 nm, both in the infrared spectrum, the intensity counts are not above the level of background noise of the apparatus.

$MgTa_2O_6$: Sample 4, Trail 1+3

From Sample 4, two trials were combined to test in XRL because of their similar disordered appearance, pull-down rate and μ-PD experimental temperature. The XRL results from this test are shown in Figure 117.

Again the relative intensity values from this sample are extremely low. While there appears to be an emission peak around 850 nm and 980 nm, both in the infrared spectrum, the intensity

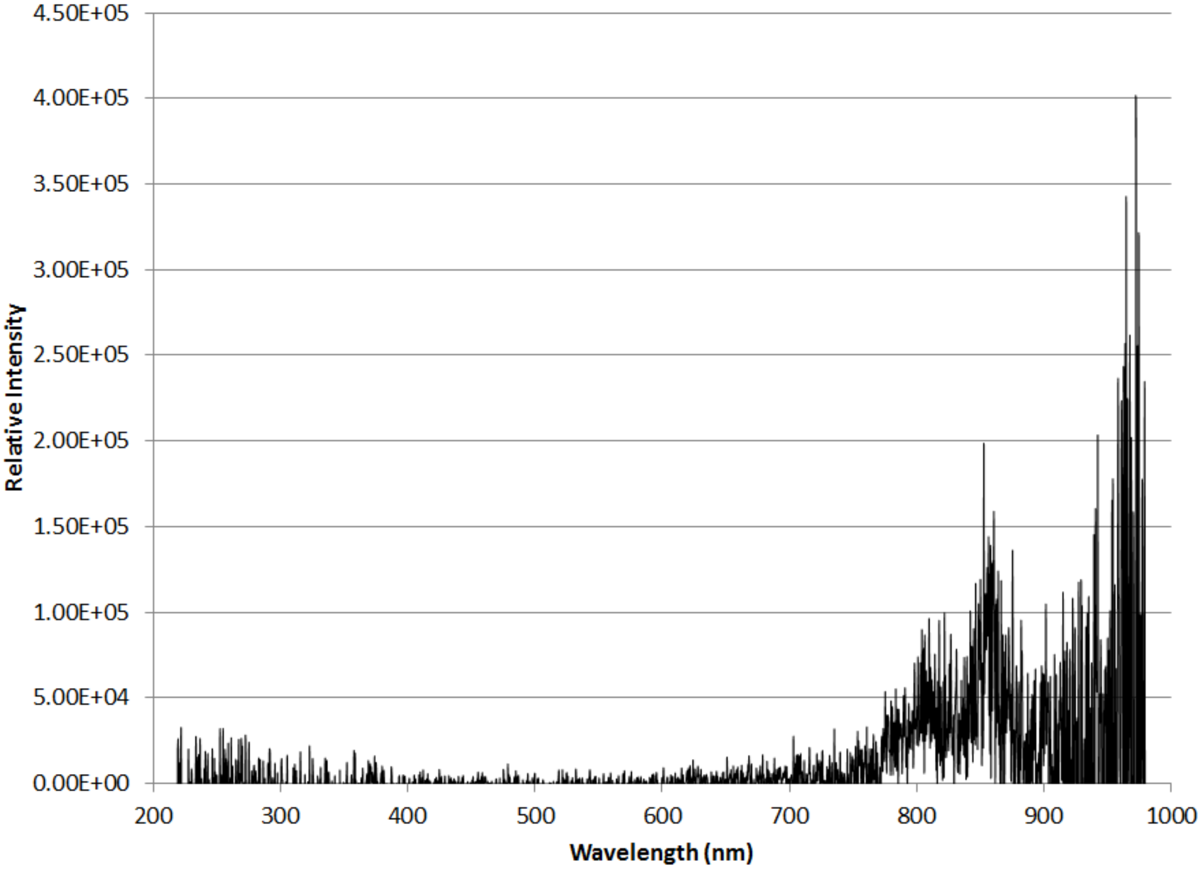

Figure 117: XRL intensity for the combination of $MgTa_2O_6$ growths from Sample 1, Trial 1+3.

counts are not above the level of background noise of the apparatus.

While the $MgTa_2O_6$ emission results may look encouraging with there repeatable emission peaks they are nothing above background noise when compared to the relative intensity of the Ce:LuAG samples. This comparison is shown in Figure 118.

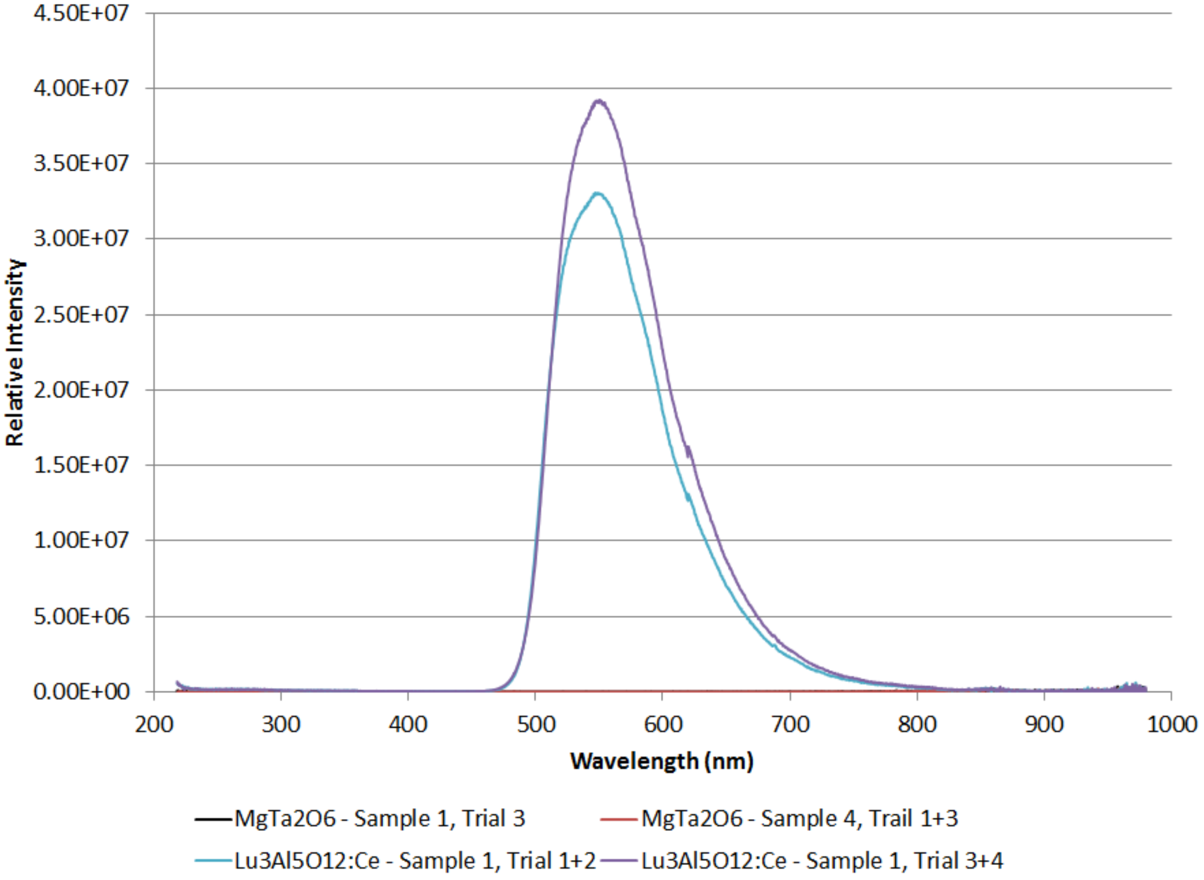

Figure 118: Four-way comparison of XRL results. The $MgTa_2O_6$ test results are barely discernible along the x-axis while the Ce:LuAG relative intensities dominate.

Scanning Electron Microscopy

Scanning electron microscopy (SEM) was performed on four Ce:LuAG and a single $MgTa_2O_6$ growth. All of the samples with the exception of LBNL Sample 1468.7M were coated with tungsten prior to analysis because of the insulating properties of the growths. This coated grounded the samples properly and allowed imaging to occur at greater magnification. LBNL Sample 1468.7M was left uncoated to determine the relative effectiveness of SEM on an insulating sample.

Ce:LuAG : LBNL Sample 1482.7M

A new Ce:LuAG sample with reduced cerium content (< 0.5 mol% Ce) was sent from LBNL for analysis, measuring 10 *mm* in length. This sample was coated in tungsten prior to SEM testing.

This crystal, prior to coating, was noticeably more transparent than the higher cerium content crystals grown experimentally in this study. Its uniform transparency implied that it was a single crystal, SEM analysis was conducted to confirm this. Images were taken at 200, 400, 800, 1600 and 2000x magnification at 20 kV accelerating voltage.

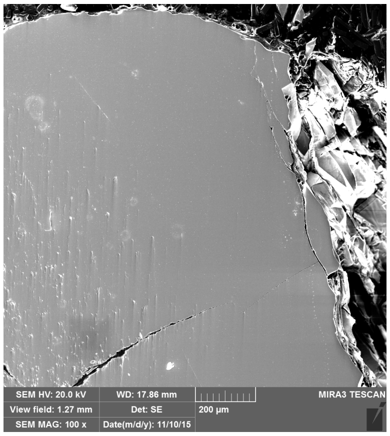

Figure 119: Ce:LuAG crystal (LBNL Sample 1482.7M).

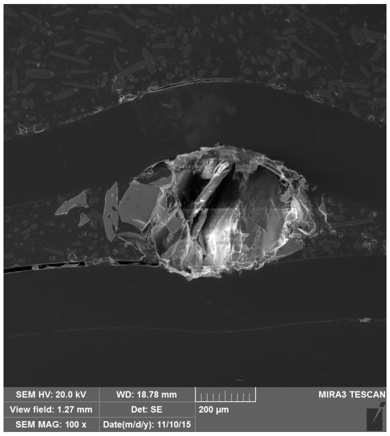

Figure 120: Ce:LuAG crystal, MAG: 100x (Sample 1, Trial 2).

The crystal did not possess any grain structure at any of the magnifications or locations investigated at the sample surface. The surface was cracked severely in some regions due to the high pressure mounting procedure. At higher magnifications the surface remained featureless from a grain boundary perspective as shown in Figure 121. Additional SEM images of this Ce:LuAG crystal can be found in the Appendix.

Ce:LuAG : Sample 1, Trial 2

This Ce:LuAG crystal was produced from the 1 mm OD crucible nozzle. It was the smallest sample investigated as there were concerns about perimeter damage from the mounting process. This damage was evident when the sample was examined under low magnification as shown in Figure . Images were taken at 100, 200, 400, 600, 800 and 1000x magnification at 20 kV accelerating voltage.

A small flat surface existed on the left side of the crystal. This area was investigated for grain boundaries but none were found. Additional SEM images of this Ce:LuAG crystal can be found in the Appendix.

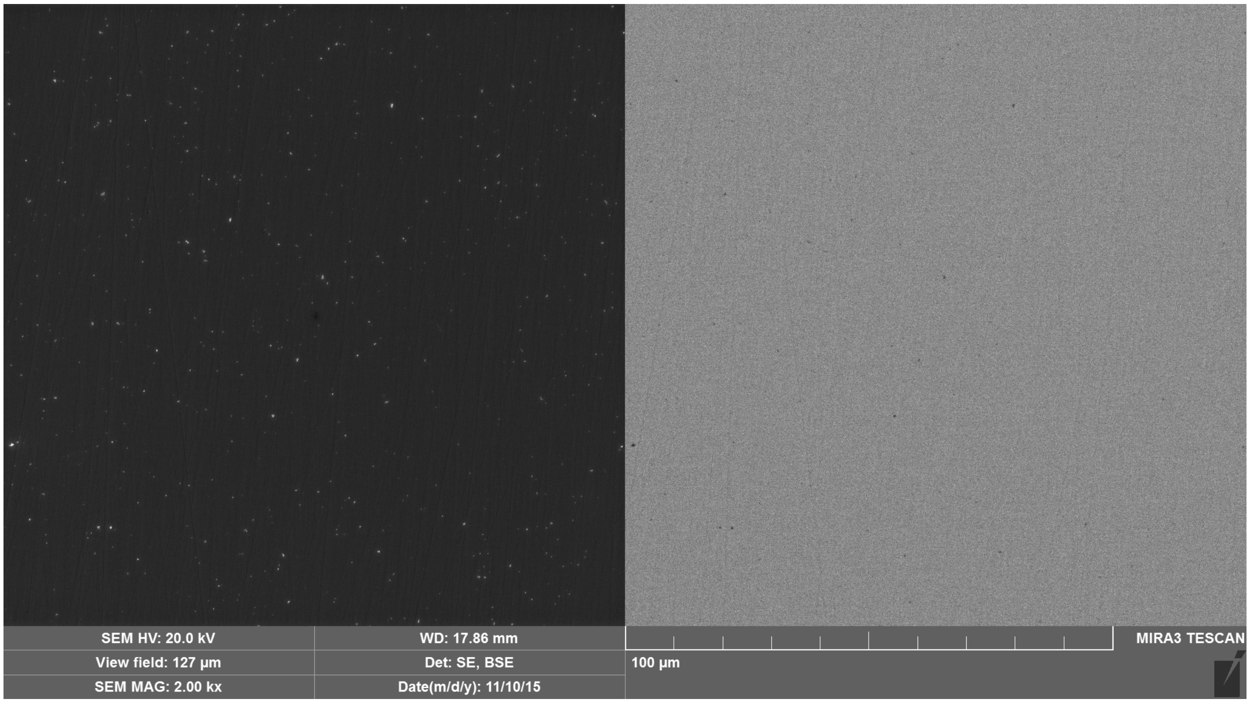

Figure 121: Ce:LuAG crystal under secondary electrons (left) and backscatter detection (right), MAG: 2000x (LBNL Sample 1482.7M). Both images are featureless outside of some dust particles.

Ce:LuAG : Sample 2, Trial 3

This Ce:LuAG crystal was produced from the 3 mm OD crucible nozzle. It was a larger diameter sample than the Ce:LuAG crystal analyzed in Sample 1, Trial 2. Due to the larger diameter and mass this crystal was not damaged as severely in the mounting process as shown in Figure 122.

Images were taken at 100, 200, 400, 800, 1600 and 2000x magnification at 20 kV accelerating voltage. Additional SEM images of this Ce:LuAG crystal can be found in the Appendix.

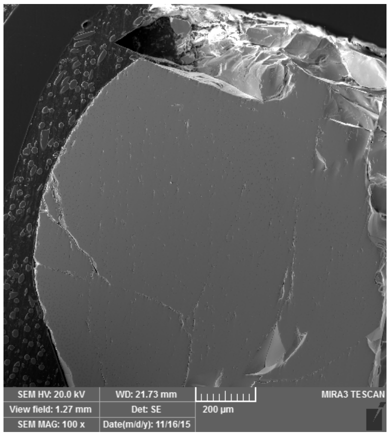

Figure 122: Ce:LuAG crystal, MAG: 100x (Sample 2, Trial 3).

Ce:LuAG : LBNL Sample 1468.7M

This Ce:LuAG sample was left uncoated and taped to the platform with carbon tape so it would not be moved when vacuum was applied to the chamber. This was done to determine if detailed images could be acquired on an insulating material when provided with a sufficiently low accelerating voltage.

Lower magnifications of less than 200x appeared to be displaying properly with accelerating voltages lowered to between 3-5 kV. At higher magnifications the images became severely distorted, changing appearance in waves even at lower voltages, an example of this distortion is shown in Figure 123.

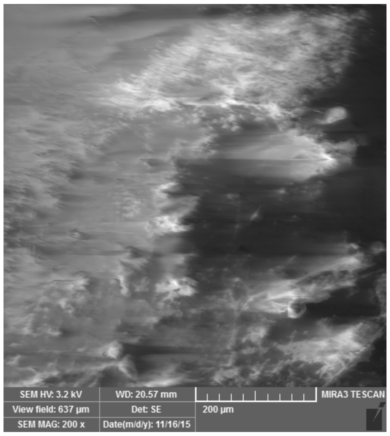

Figure 123: Uncoated Ce:LuAG crystal (LBNL Sample 1468.7M).

As the investigation of the sample continued the results steadily decreased in quality. It was discovered that the microscope was not capable of accelerating voltages lower than 3 kV, later increasing to 3.5 kV. Below these values the detector would simply return static that could not be focused or adjusted meaningfully. At higher accelerating voltages charges could be seen coursing through the sample, distorting the image when focused on. Adjusting the working distance resulted in severe local distortion. For these reasons it was determined that future samples will need to be coated for high magnification work but low magnification work coupled with a lower accelerating voltage may provide sufficient results. Additional SEM images of this Ce:LuAG crystal can be found in the Appendix.

$MgTa_2O_6$: Sample 4, Trial 5

This $MgTa_2O_6$ crystal was produced from the 3 mm OD crucible nozzle and like all of the growths produced on top of the $MgTa_2O_6$ seed it possessed poor diameter control and no transparency.

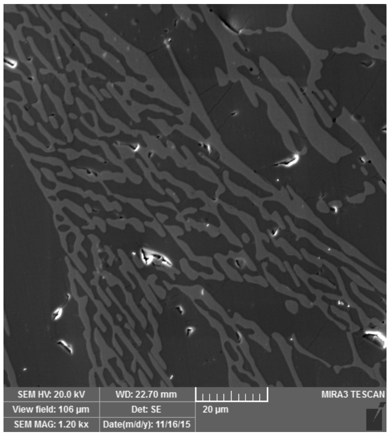

Figure 124: $MgTa_2O_6$ two-phase growth (Sample 4, Trial 5).

While the Ce:LuAG crystal grown experimentally and those analyzed from LBNL had been featureless with respect to grain boundaries the $MgTa_2O_6$ showed clear evidence of at least two phases present. These phases are shown in detail in Figure 124. Additional SEM images of this $MgTa_2O_6$ crystal can be found in the Appendix.

Energy-dispersive X-ray Spectroscopy

The EDS spectrum outputs for the tested samples are listed below. Each plot displays the number of counts against the specified energy range. These counts are shown in red. The testing automatically applies background determination and peak deconvolution before determining the elements. Elements are compared against database entries and labeled with their element and K, L or M energy lines by the software.

The spectrum background noise is outlined in blue, consequently the peak deconvolution calculation is plot in cyan, following the profile of the collected spectrum.

Ce:LuAG : Sample 2, Trial 3

The investigated sample of Ce:LuAG growth had been previously coated with a thin layer of tungsten and had already undergone SEM testing. The EDS testing was conducted on three different locations along the sample surface in regions devoid of visible surface defects or debris at a magnification of 4000x. The first location analyzed is shown in Figure 125 where the highlighted region was the area analyzed.

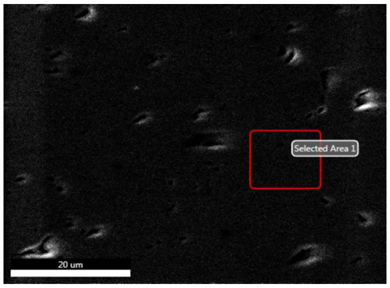

Figure 125: Highlighted area of EDS analysis. Area 1 of Ce:LuAG Sample 2, Trial 3 growth.

The three spectrum outputs showed good correlation, the first is displayed in Figure 128. Iridium contamination was detected with the crucible being the likely source. This iridium precipitation in the melt was observed in post-experiment imagery and with a higher density than the melt it would reason that it would fall down into the crystal's formation. The magnesium peak detected may have been from the chamber or ceramic supports used in the $MgTa_2O_6$ growth attempts. The second and third location and spectrum outputs are shown in the Appendix.

Spectrum analysis occurred at an accelerating voltage of 20 kV, MAG: 2000, live time of 30 s, amp time of 0.8 μs and a resolution of 133.7 eV. Summary statistics for this analysis are shown in Table 15.

Element	Weight %	Atomic %	Net Intensity	Net Intensity Error
O K	20.43	57.97	1440.24	0.01
Mg K	0.25	0.47	67.11	0.16
Al L	14.92	25.11	4788.83	0.00
Ce L	0.24	0.08	16.22	0.53
Lu L	50.69	13.15	1976.04	0.01
W L	3.09	0.76	81.2	0.26
Ir L	10.38	2.45	212.96	0.14

Table 14: eZAF Smart Quantitative Results from TEAM software. Area 1 of Ce:LuAG Sample 2, Trial 3 growth.

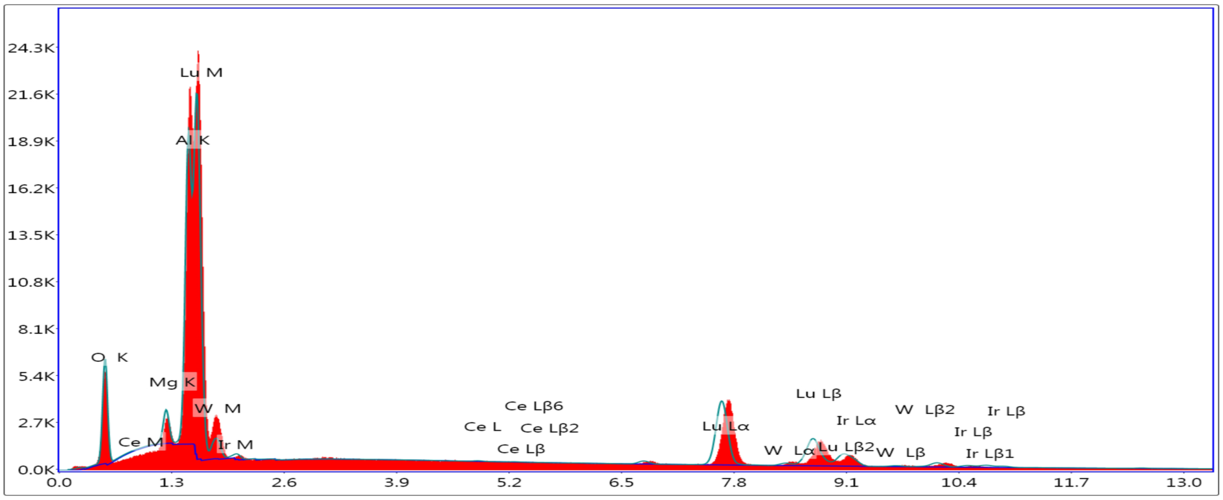

Figure 126: EDS output spectrum of Area 1 of Ce:LuAG Sample 2, Trial 3 growth.

Ce:LuAG : LBNL Sample 1482.7M

The investigated sample of Ce:LuAG growth had been previously coated with a thin layer of tungsten and had already undergone SEM testing. The EDS testing was conducted on three different locations along the sample surface in regions devoid of visible surface defects or debris at a magnification of 4000x. The first location analyzed is shown in Figure 127 where the highlighted region was the area analyzed.

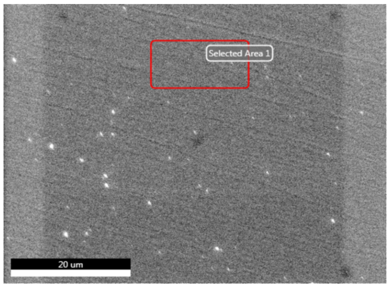

Figure 127: Highlighted area of EDS analysis. Area 1 of LBNL Ce:LuAG Sample 1482.7M growth.

The three spectrum outputs showed good correlation, the first is displayed in Figure 128. Iridium contamination was detected with the crucible being the likely source. This iridium precipitation in the melt was observed in post-experiment imagery and with a higher density than the melt it would reason that it would fall down into the crystal's formation. The magnesium peak detected may have been from the chamber or ceramic supports used in the $MgTa_2O_6$ growth attempts. The second and third location and spectrum outputs are shown in the appendix.

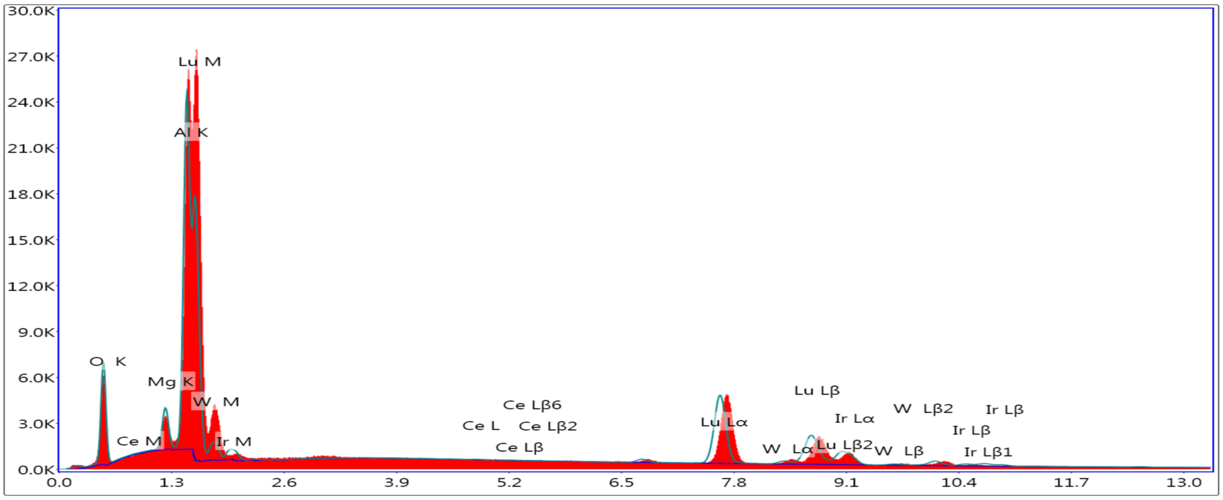

Figure 128: EDS analysis of Area 1 of LBNL Ce:LuAG Sample 1482.7M growth.

Element	Weight %	Atomic %	Net Intensity	Net Intensity Error
O K	18.74	55.34	1553.58	0.01
Mg K	0.52	1.02	170.36	0.06
Al L	14.94	26.17	5740.85	0.00
Ce L	0.14	0.05	11.00	0.53
Lu L	51.04	13.78	2389.97	0.01
W L	3.59	0.92	113.27	0.22
Ir L	11.03	2.71	271.97	0.12

Table 15: eZAF Smart Quantitative Results from TEAM software. Area 1 of LBNL Ce:LuAG Sample 1482.7M.

$MgTa_2O_6$: Sample 4, Trial 5

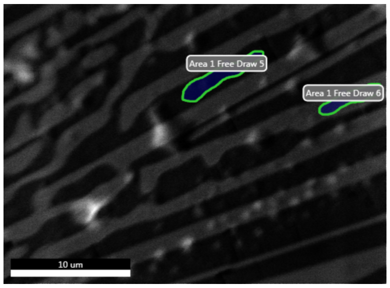

Figure 129: Highlighted area of EDS analysis. Area 1 of $MgTa_2O_6$ Sample 4, Trial 5 Growth.

The investigated sample of $MgTa_2O_6$ growth had been previously coated with a thin layer of tungsten. The two phases were investigated and compared. Due to the irregular shape of the phases formed a free draw region was created for analysis as shown in Figure 129.

Each phase was then analyzed using EDS. The results for the dark and light phases are shown in Figure 130. When the dark phases are analyzed across the sample they show a significant increase in Mg content. To ensure that these readings were accurate, three different regions of the crystal were selected at random where these two phases existed next to each other. Each dark phase measured significantly higher magnesium content. The second and third location and spectrum outputs are shown in the appendix.

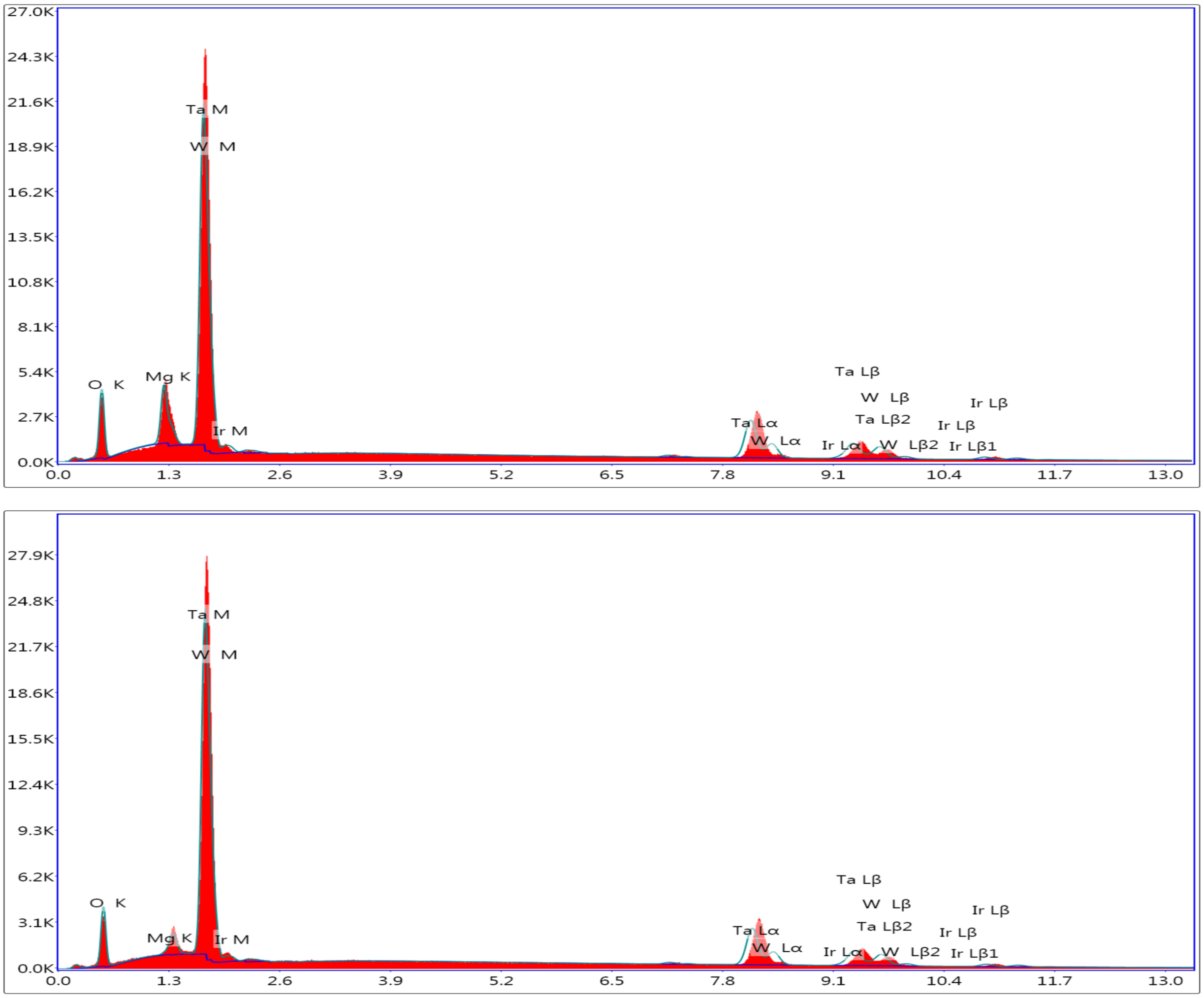

Figure 130: EDS analysis of light phase (top) and dark phase (bottom), note the discrepancy in the Mg K peaks.

Element	Weight %	Atomic %	Net Intensity	Net Intensity Error
O K	19.00	65.28	964.98	0.01
Mg K	5.24	11.84	979.28	0.01
Ta L	51.15	15.53	1244.69	0.02
W L	24.37	7.28	491.61	0.05
Ir L	0.24	0.07	3.76	0.53

Table 16: Dark phase eZAF Smart Quantitative Results from TEAM software. Area 1 of $MgTa_2O_6$ Sample 4, Trial 5 growth.

Element	Weight %	Atomic %	Net Intensity	Net Intensity Error
O K	18.80	72.02	928.26	0.01
Mg K	0.28	0.70	50.96	0.16
Ta L	55.53	18.81	1364.13	0.02
W L	25.31	8.44	515.86	0.05
Ir L	0.08	0.03	1.33	0.55

Table 17: Light phase eZAF Smart Quantitative Results from TEAM software. Area 1 of $MgTa_2O_6$ Sample 4, Trial 5 growth.

Conclusions

Single crystal Ce:LuAG and multi-phase $MgTa_2O_6$ growths were synthesized using the μ-PD method and were prepared from powder oxides. Sample preparation techniques and μ-PD methods were outlined and refined.

The single crystal Ce:LuAG matched publication imagery and was confirmed to be correctly synthesized when x-ray luminescence was performed where the emission peak was within the published emission range. Scanning electron microscopy imagery also confirmed the absence of grain boundaries within the grown crystals as well as those sent later from LBNL. Energy-dispersive x-ray spectroscopy was performed, confirming the appropriate compounds of the crystal but also contamination from both magnesium and iridium. It was hypothesized that the magnesium was from some of the ceramic insulation but the quantity in which it was detected was surprising high. Iridium inclusion was the result of the breakdown of the iridium crucible containing the molten melt. This was supported with post-experimental imagery of iridium precipitated on the top surface of the melt, with a higher density than the melt it undoubtedly moved downwards and into the crystal.

After an extensive literature search there was no evidence of $MgTa_2O_6$ growths from μ-PD. X-ray powder diffraction analysis showed successful formation of the $MgTa_2O_6$ compound from the μ-PD experiments. X-ray luminescence testing showed no emissions above background noise, from this it was concluded that the compound could not be used as a scintillator in its present formation. Scanning electron microscopy revealed a detailed two-phase structure that was undoubtedly a factor in its poor scintillation properties. These two phases were compared using EDS. Here it was discovered that the darker phase from the SEM imagery had a statistically significant higher magnesium content. This was true across all sample areas.

APPENDIX

SEM Results: LBNL Ce:LuAG Sample 1482.7M

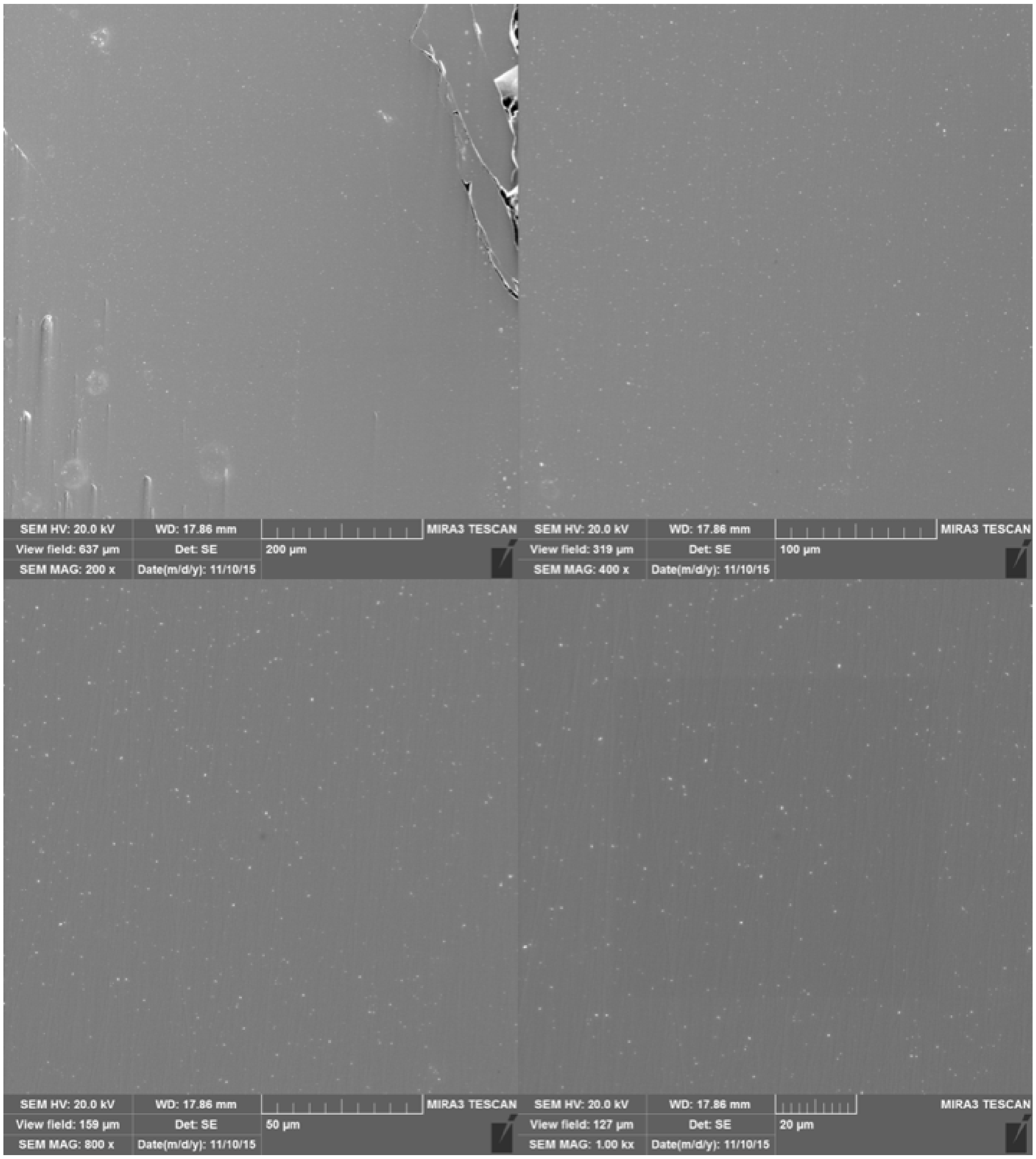

Figure 131: Ce:LuAG crystal, under various magnifications (LBNL Sample 1482.7M).

SEM Results: Ce:LuAG Sample 1, Trial 2

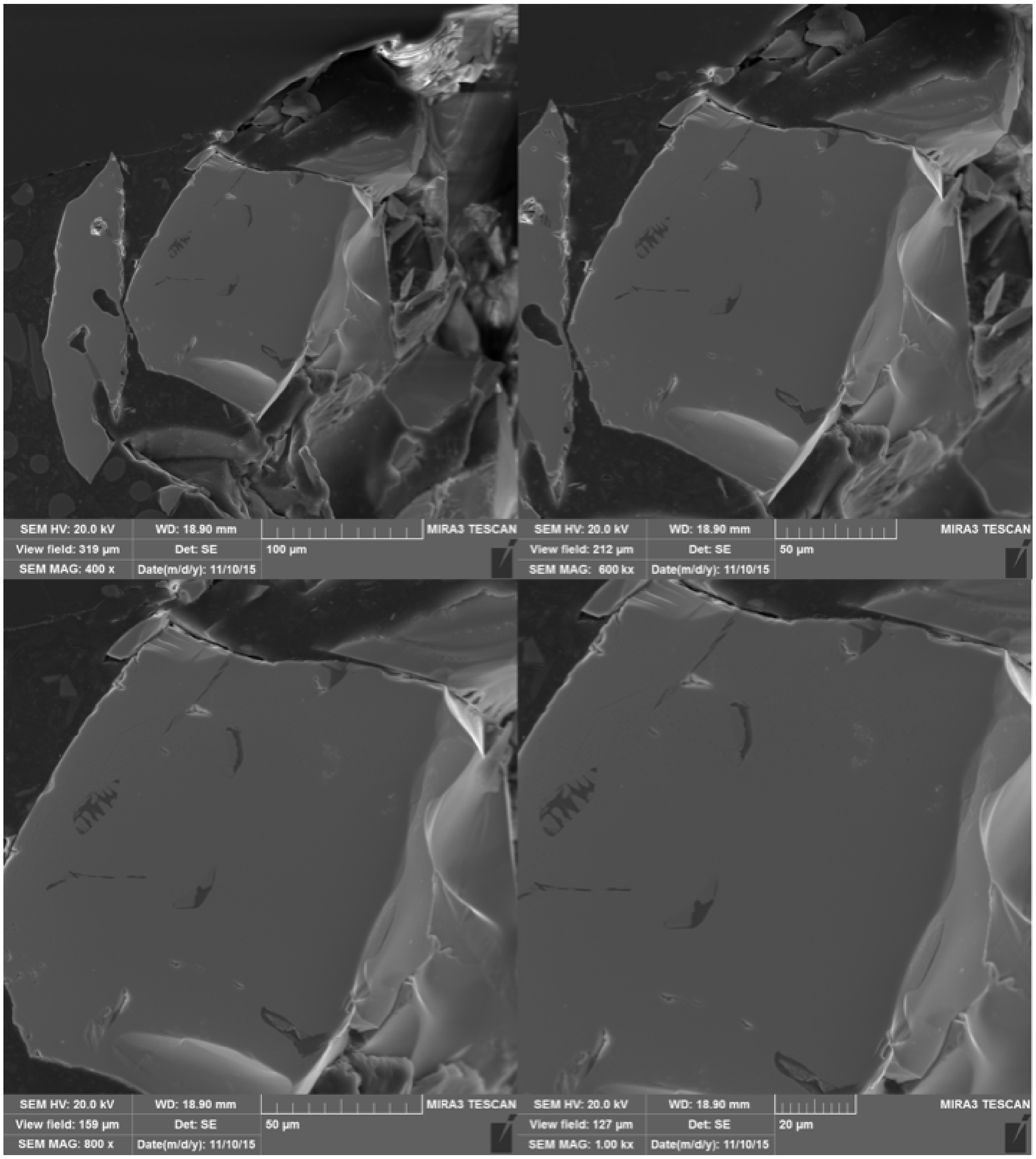

Figure 132: Ce:LuAG crystal, under various magnifications (Sample 1, Trial 2).

SEM Results: Ce:LuAG Sample 2, Trial 3

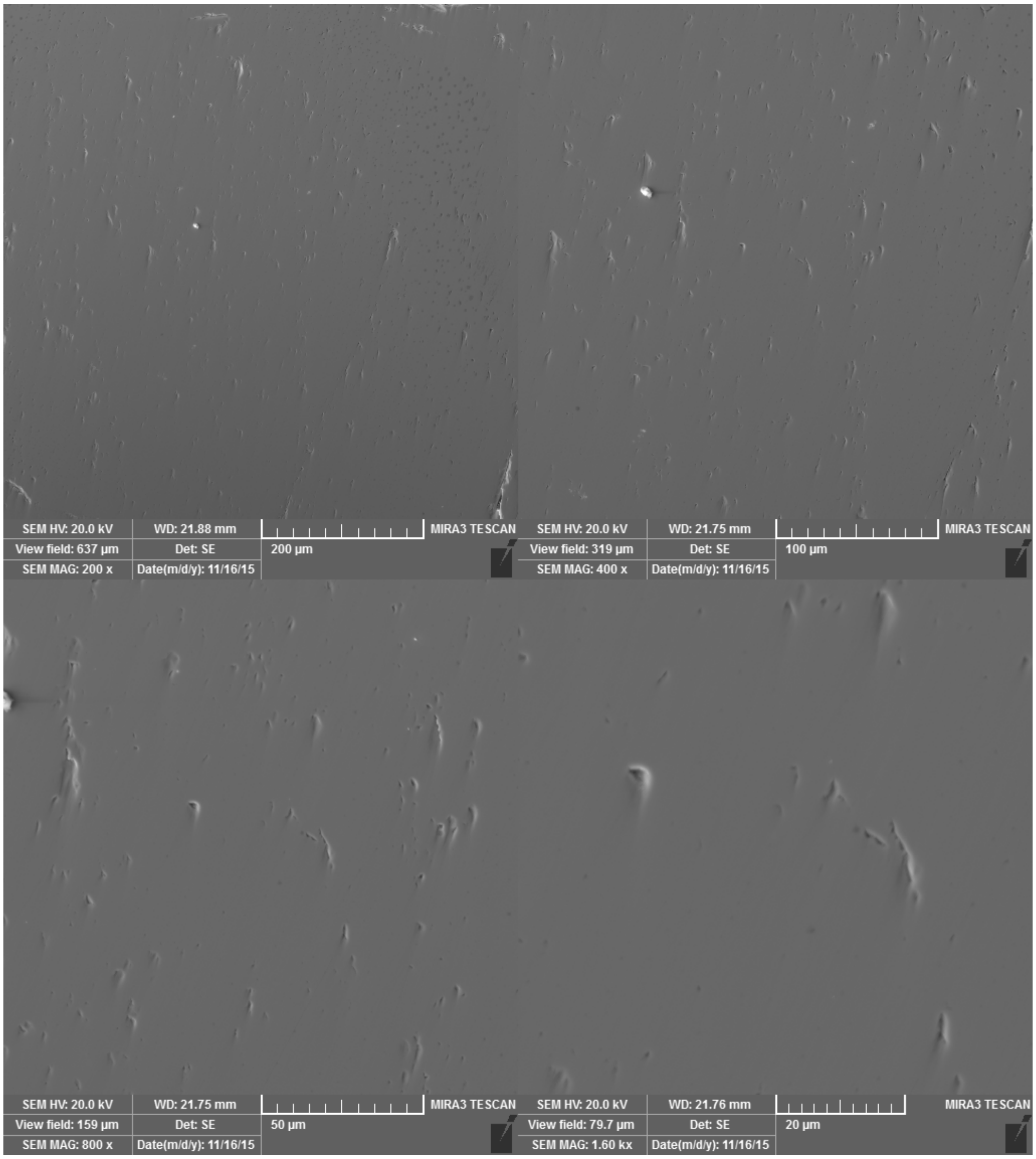

Figure 133: Ce:LuAG crystal, under various magnifications (Sample 2, Trial 3).

SEM Results: Uncoated LBNL Ce:LuAG Sample 1468.7M

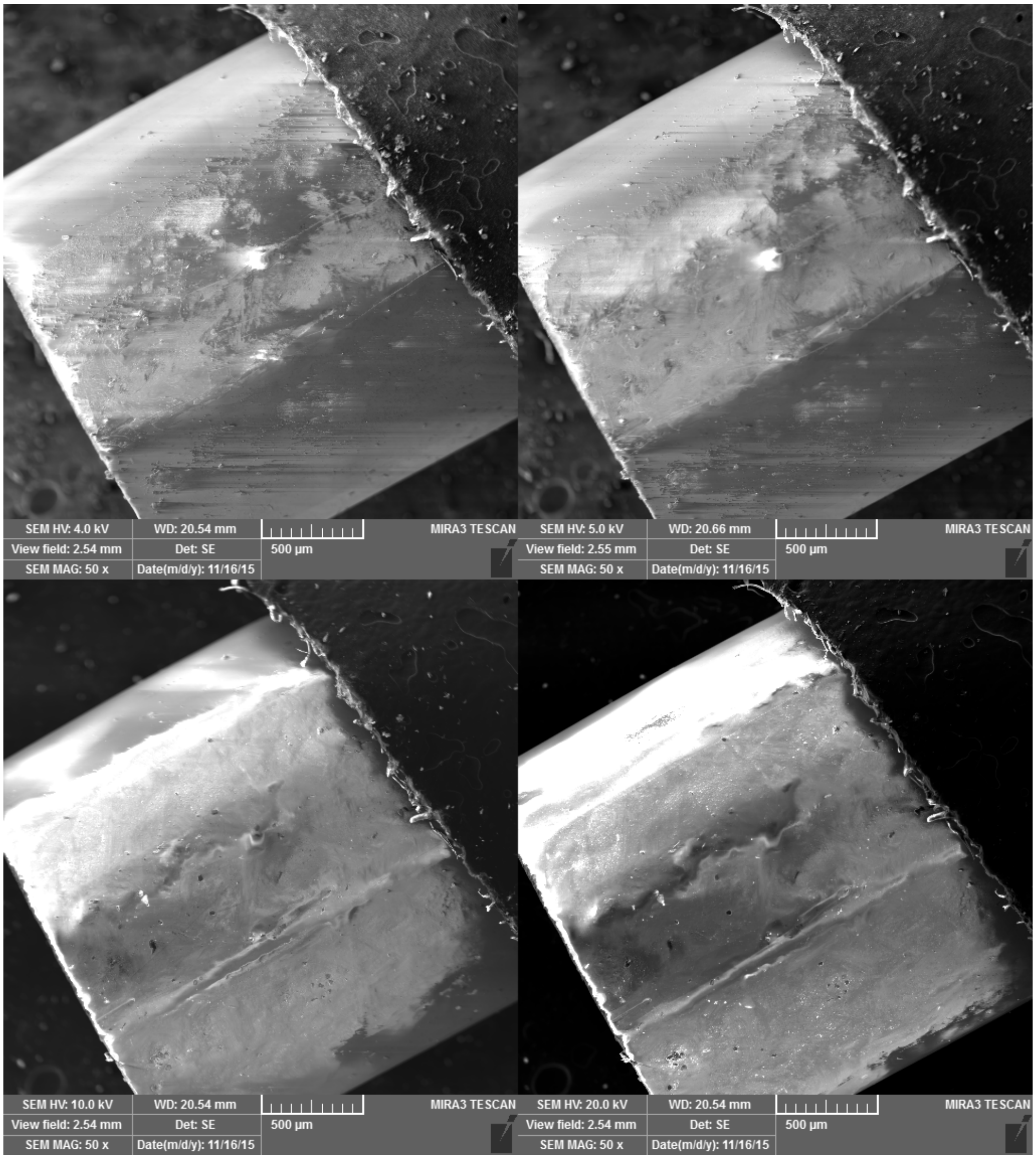

Figure 134: Ce:LuAG crystal, under various magnifications (Sample 1, Trial 2).

SEM Results: $MgTa_2O_6$ Sample 4, Trial 5

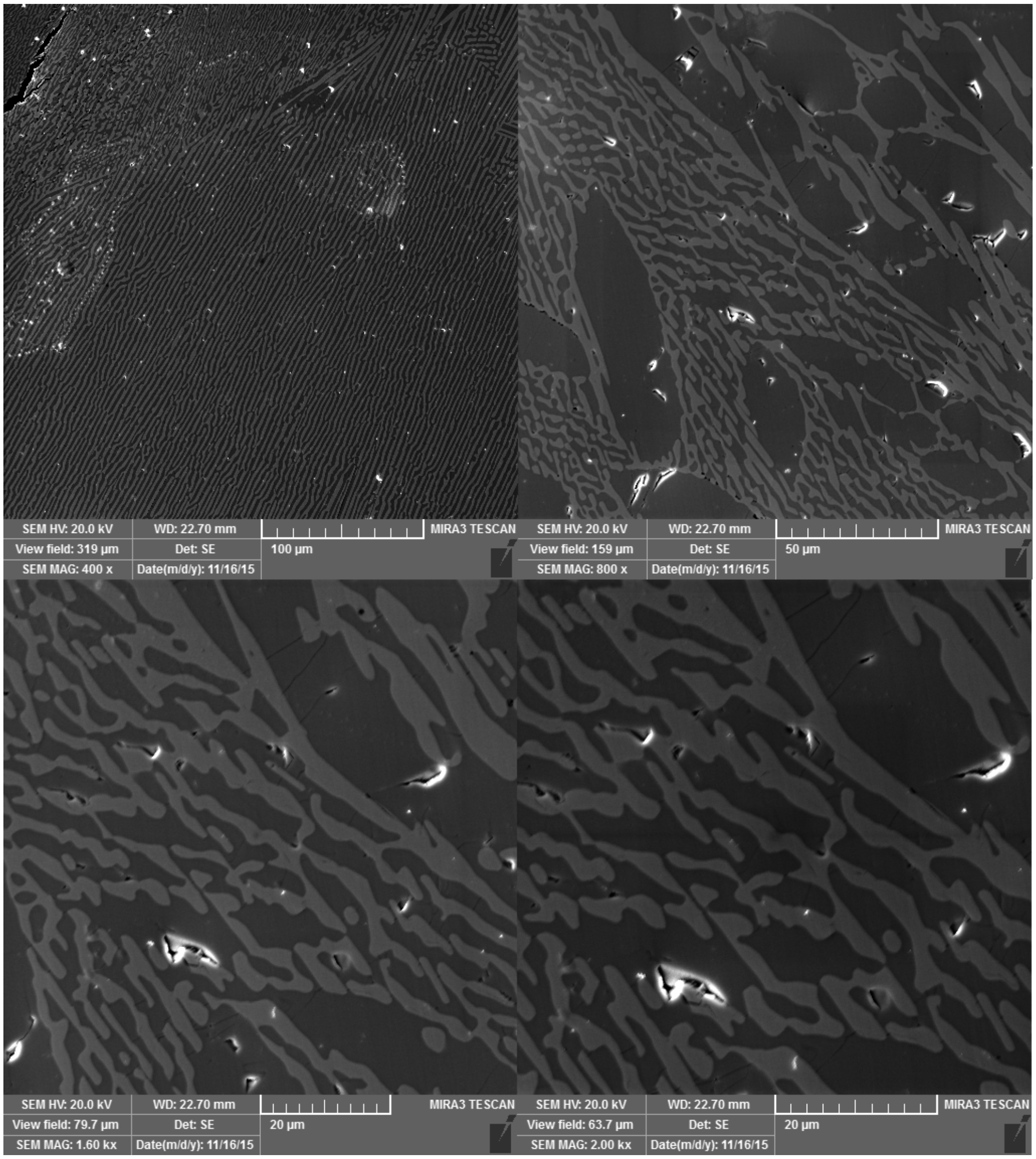

Figure 135: $MgTa_2O_6$ crystal, under various magnifications (Sample 4, Trial 5).

EDS Results: Ce:LuAG Sample 2, Trial 3

Area 2

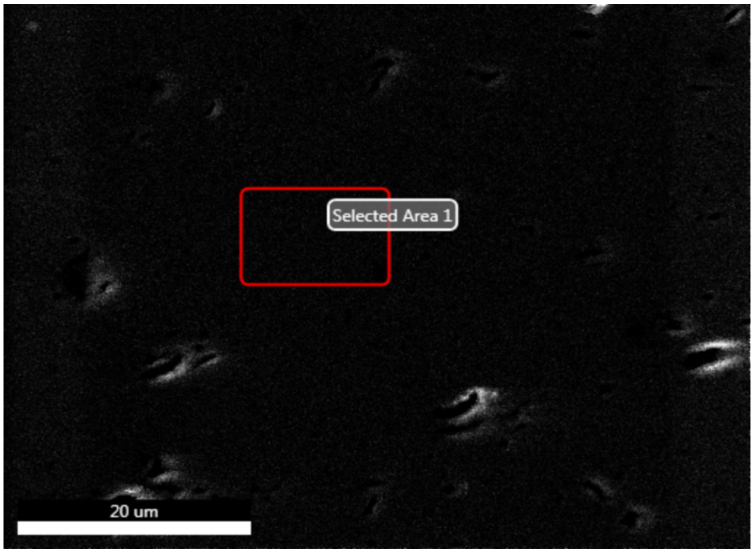

Figure 136: Highlighted region of EDS analysis. Area 2 of Ce:LuAG Sample 2, Trial 3 growth.

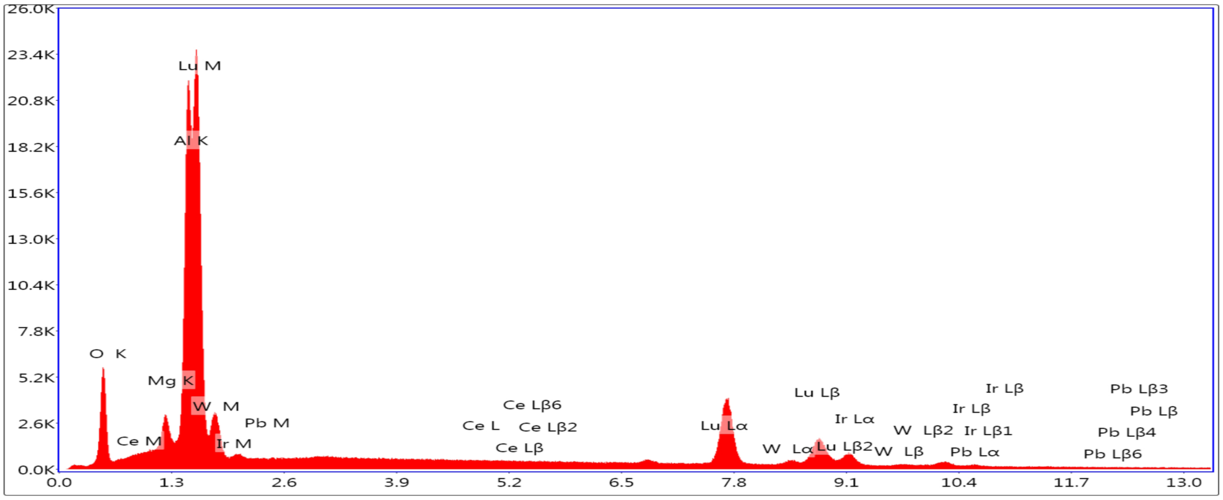

Figure 137: EDS output spectrum of Area 2 Ce:LuAG Sample 2, Trial 3 growth.

Element	Weight %	Atomic %	Net Intensity	Net Intensity Error
O K	20.45	57.95	1442.18	0.01
Mg K	0.33	0.62	90.21	0.10
Al K	14.91	25.05	4795.17	0.00
Pb M	0.11	0.02	7.81	0.31
Ce L	0.07	0.02	4.78	0.54
Lu L	50.21	13.01	1961.96	0.01
W L	3.42	0.84	90.03	0.26
Ir L	10.50	2.48	216.00	0.13

Table 18: eZAF Smart Quantitative Results from TEAM software. Area 2 of Ce:LuAG Sample 2, Trial 3 growth.

Area 3

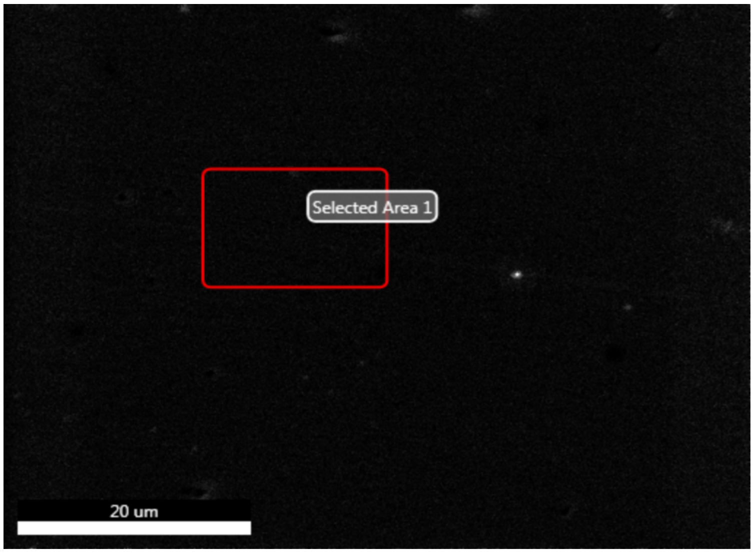

Figure 138: Highlighted region of EDS analysis. Area 3 of Ce:LuAG Sample 2, Trial 3 growth.

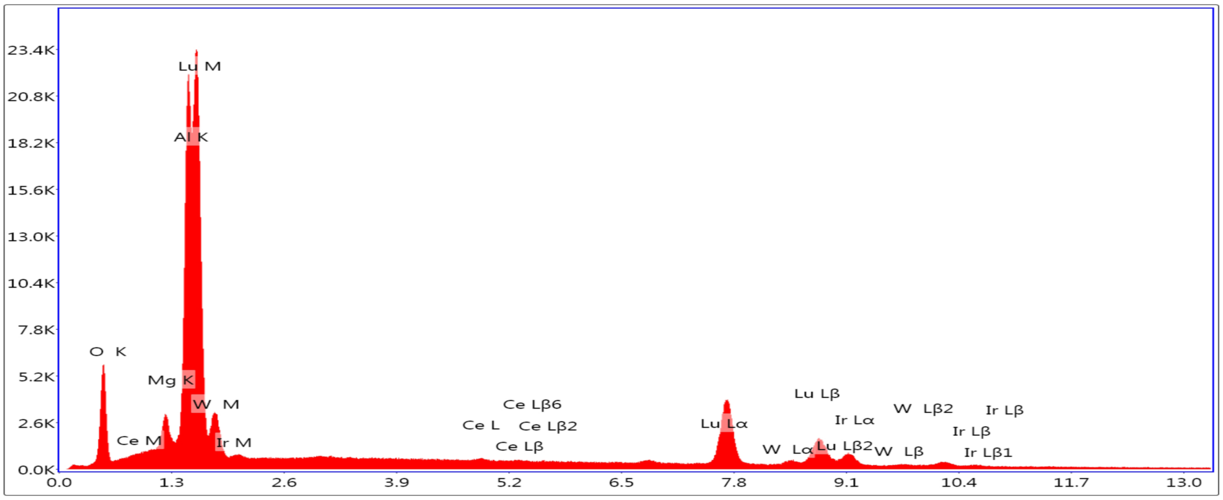

Figure 139: EDS output spectrum of Area 3 Ce:LuAG Sample 2, Trial 3 growth.

Element	Weight %	Atomic %	Net Intensity	Net Intensity Error
O K	20.88	58.38	1476.98	0.01
Mg K	0.30	0.55	79.89	0.11
Al K	15.08	25.01	4791.00	0.00
Ce L	0.62	0.20	41.24	0.41
Lu L	49.50	12.66	1920.99	0.01
W L	3.18	0.78	83.24	0.26
Ir L	10.44	2.43	213.21	0.14

Table 19: eZAF Smart Quantitative Results from TEAM software. Area 3 of Ce:LuAG Sample 2, Trial 3 growth.

EDS Results: LBNL Ce:LuAG Sample 1482.7

Area 2

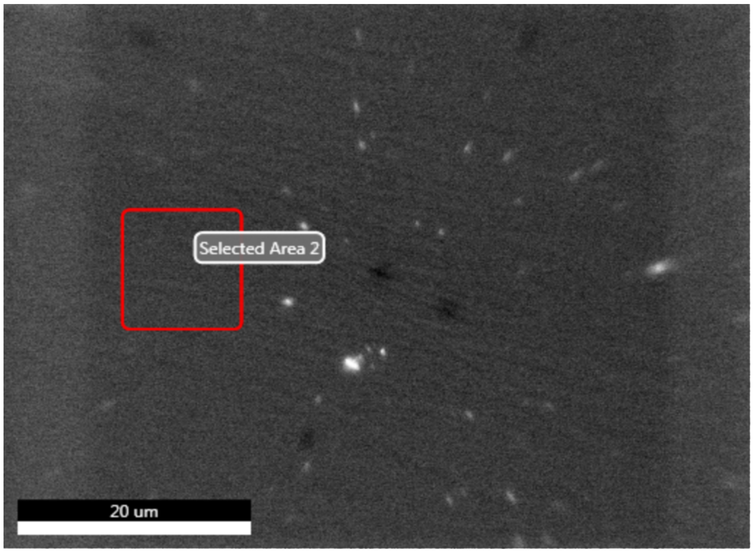

Figure 140: Highlighted region of EDS analysis. Area 2 of LBNL Ce:LuAG Sample 1468.7M growth.

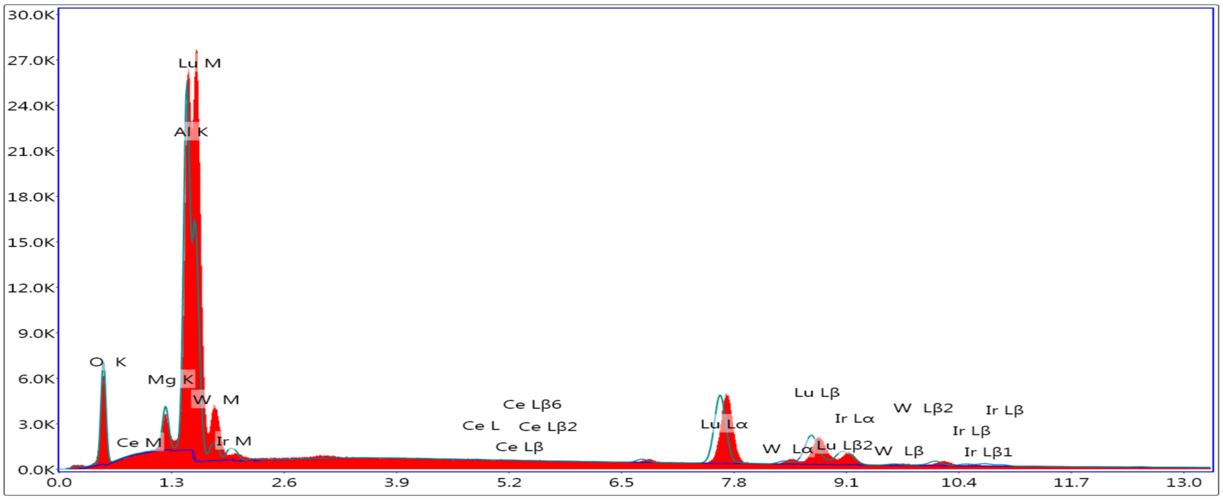

Figure 141: EDS output spectrum of Area 2 of LBNL Ce:LuAG Sample 1468.7M growth.

Element	Weight %	Atomic %	Net Intensity	Net Intensity Error
O K	18.75	55.20	1577.22	0.01
Mg K	0.61	1.18	200.7	0.05
Al K	15.05	26.27	5857.56	0.00
Ce L	0.13	0.05	10.95	0.53
Lu L	50.82	13.68	2411.79	0.01
W L	3.71	0.95	118.69	0.22
Ir L	10.92	2.68	272.83	0.13

Table 20: eZAF Smart Quantitative Results from TEAM software. Area 2 of LBNL Ce:LuAG Sample 1468.7M growth.

Area 3

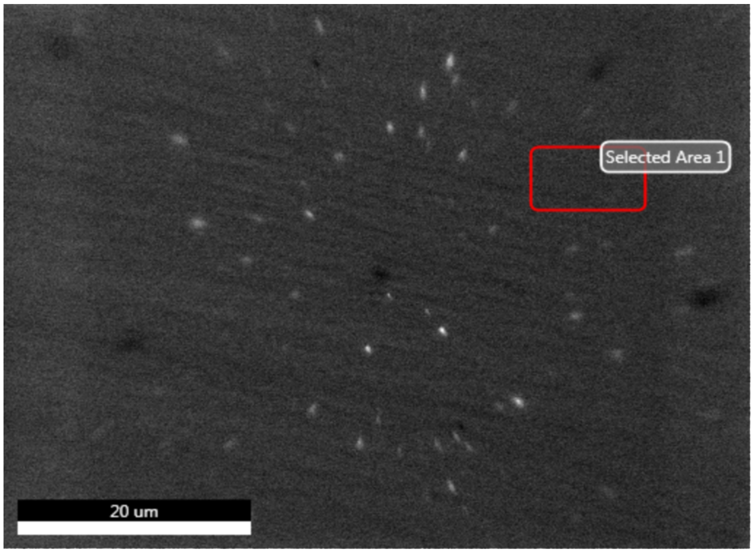

Figure 142: Highlighted region of EDS analysis. Area 3 of LBNL Ce:LuAG Sample 1468.7M Growth.

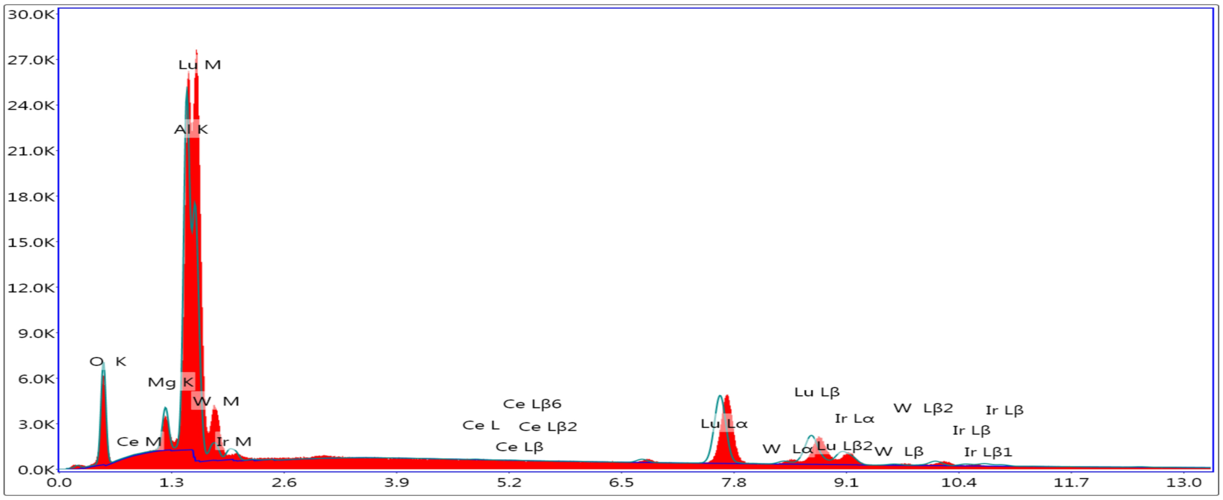

Figure 143: EDS output spectrum of Area 3 of LBNL Ce:LuAG Sample 1468.7M growth.

Element	Weight %	Atomic %	Net Intensity	Net Intensity Error
O K	18.74	55.23	1572.99	0.01
Mg K	0.60	1.17	198.3	0.05
Al K	15.00	26.21	5824.04	0.00
Ce L	0.16	0.06	13.30	0.54
Lu L	50.67	13.66	2402.55	0.01
W L	3.56	0.91	113.53	0.23
Ir L	11.27	2.77	281.45	0.13

Table 21: eZAF Smart Quantitative Results from TEAM software. Area 3 of LBNL Ce:LuAG Sample 1468.7M growth.

$MgTa_2O_6$: Sample 4, Trial 5

Area 2

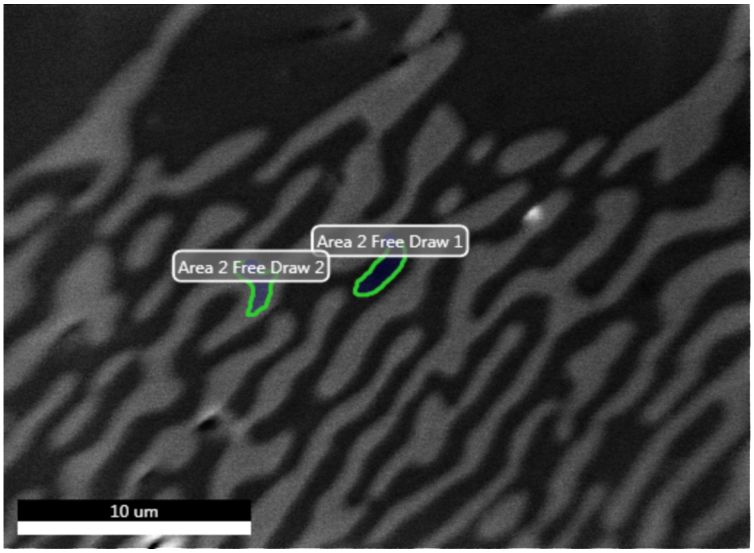

Figure 144: Highlighted regions of EDS analysis. Area 2 of $MgTa_2O_6$ Sample 4, Trial 5 growth.

Element	Weight %	Atomic %	Net Intensity	Net Intensity Error
O K	19.03	65.27	981.58	0.01
Mg K	5.27	11.90	1000.87	0.01
Ta L	51.16	15.51	1263.79	0.02
W L	24.13	7.20	494.26	0.05
Ir L	0.40	0.11	6.39	0.52

Table 22: Dark phase eZAF Smart Quantitative Results from TEAM software. Area 2 of $MgTa_2O_6$ Sample 4, Trial 5 growth.

Element	Weight %	Atomic %	Net Intensity	Net Intensity Error
O K	18.92	72.01	940.03	0.01
Mg K	0.39	0.97	70.57	0.10
Ta L	55.41	18.65	1366.9	0.02
W L	25.20	8.35	515.63	0.05
Ir L	0.09	0.03	1.39	0.53

Table 23: Light phase eZAF Smart Quantitative Results from TEAM software. Area 2 of $MgTa_2O_6$ Sample 4, Trial 5 growth.

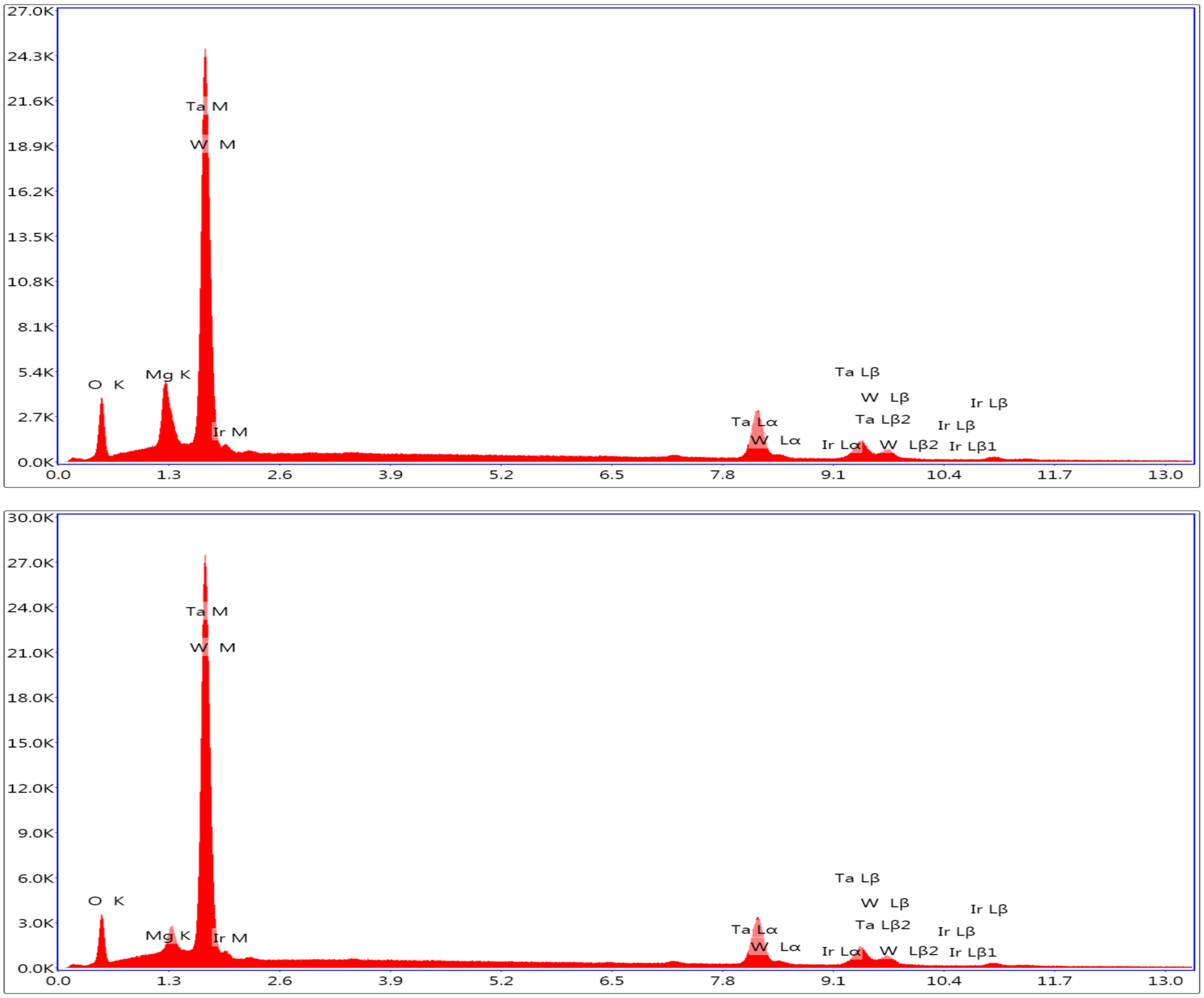

Figure 145: EDS output spectrum of light phase (top) and dark phase (bottom), note the discrepancy in the Mg K peaks. Area 2 of $MgTa_2O_6$ Sample 4, Trial 5 growth.

Area 3

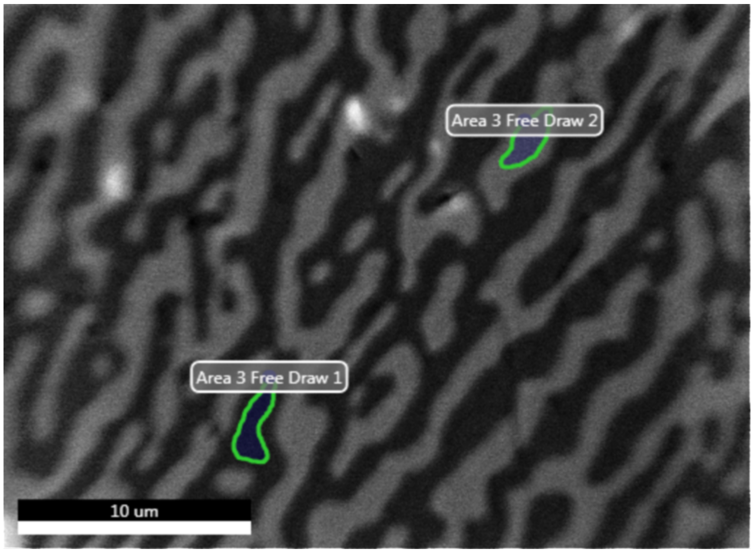

Figure 146: Highlighted area of EDS analysis. Area 3 of $MgTa_2O_6$ Sample 4, Trial 5 growth.

Element	Weight %	Atomic %	Net Intensity	Net Intensity Error
O K	19.11	65.36	981.28	0.01
Mg K	5.29	11.90	998.4	0.01
Ta L	50.81	15.36	1248.37	0.02
W L	24.52	7.30	499.45	0.05
Ir L	0.27	0.08	4.28	0.53

Table 24: Dark phase eZAF Smart Quantitative Results from TEAM software. Area 2 of $MgTa_2O_6$ Sample 4, Trial 5 growth.

Element	Weight %	Atomic %	Net Intensity	Net Intensity Error
O K	18.77	71.83	919.70	0.01
Mg K	0.37	0.93	66.97	0.12
Ta L	55.78	18.88	1359.15	0.02
W L	25.04	8.34	506.16	0.05
Ir L	0.04	0.01	0.64	0.58

Table 25: Light phase eZAF Smart Quantitative Results from TEAM software. Area 3 of $MgTa_2O_6$ Sample 4, Trial 5 growth.

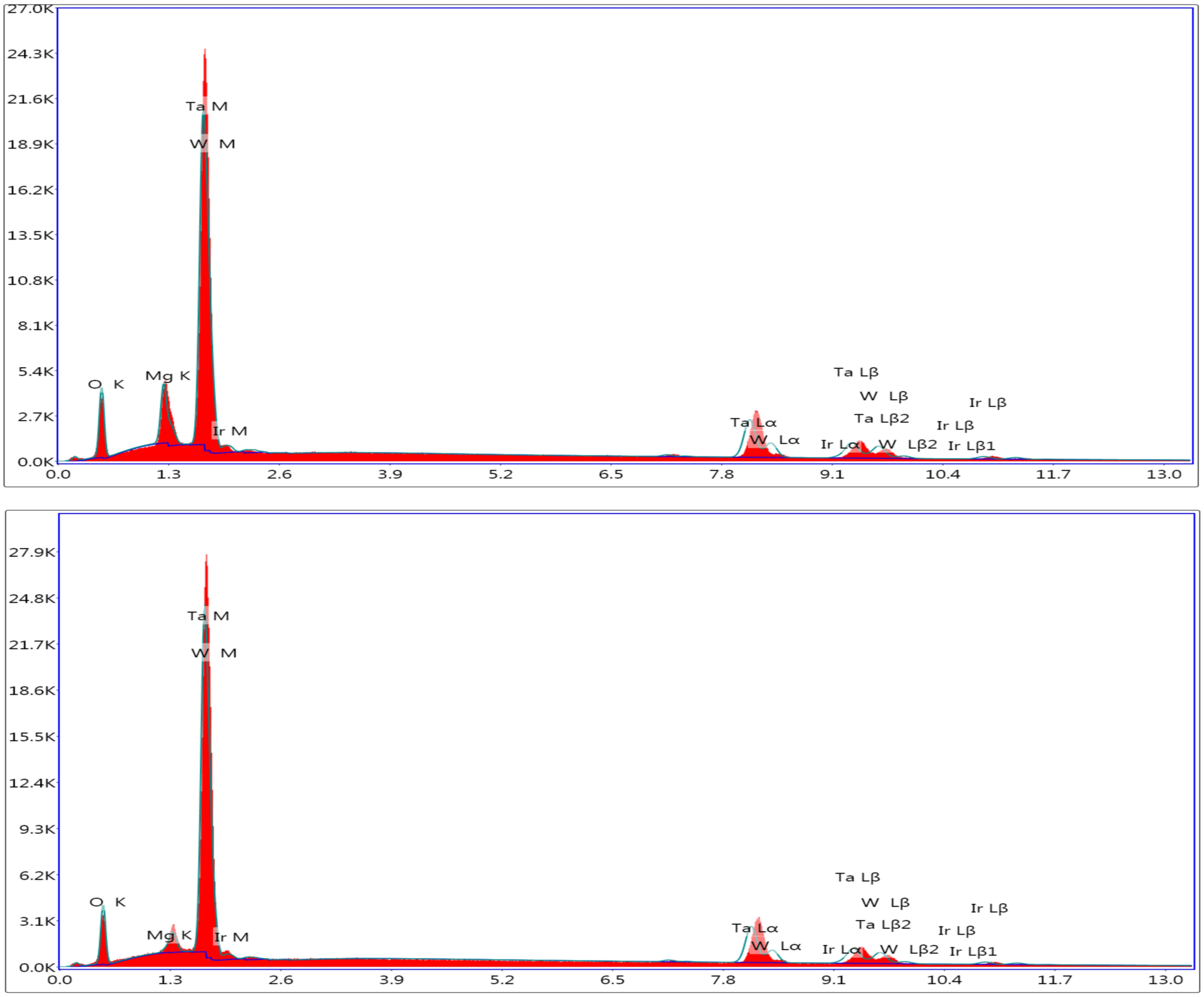

Figure 147: EDS output spectrum of light phase (top) and dark phase (bottom), note the discrepancy in the Mg K peaks. Area 3 of $MgTa_2O_6$ Sample 4, Trial 5 growth.

Software source code

Source code for programs and scripts are shown. The Windows application that the user used to capture images was written in VB while the post-processing scripts were written in Python.

```
import os
import math
from PIL import Image
from PIL import ImageFont
from PIL import ImageDraw

def Cropper(directory):
    for filename in os.listdir(directory):
        print(filename)
        img = Image.open(directory + filename)
        # Define the crop region in pixels
        left = 300
        top = 125
        right = left+375
        bottom = top+360
        box = (left, top, right, bottom)
        area = img.crop(box)
        # Save off cropped image
        area.save(directory + filename, 'png')

def TextAdder(directory):
   # Write crystal being grown on each images
    crystal = 'MgTa2O6' #'LuAG:Ce'
    # Write date of experiment on each image
    date = '2015.08.11'
    # Write the location of the experiment on each image
    site = 'LBNL'
    # Define font used on appended image text
    font_used = '/usr/share/fonts/truetype/ttf-dejavu/DejaVuSans.ttf'

    path, dirs, files = os.walk(directory).next()
    file_count = len(files)
    i=1
    for filename in sorted(os.listdir(directory)):

        setpoint = filename[20:]
        setpoint = setpoint[:-4]

        temperature = 1742*(math.pow(float(setpoint), 0.1287))-859

        print(filename)
        img = Image.open(directory + '/' + filename)
        draw = ImageDraw.Draw(img)
        font = ImageFont.truetype(font_used, 16)
        draw.text((20, 15),  crystal + "             " + filename[11]+filename[12]
               \
        + ":" + filename[14] + filename[15] + filename[16]+filename[17]+ \
        filename[18]+"             " + str(i) + \
        "/" + str(file_count),(255,255,255),font=font)
        draw.text((20, 315),site,(255,255,255),font=font)
        draw.text((20, 340), date+ "            Temp: ~" + str(int(temperature)) +
               \
        "C (SP:" + setpoint + ")",(255,255,255),font=font)
        img.save(directory + '/' + filename)
        i=i+1

# Renaming files is required for post-processing images into a video
# in some third party programs
def Renamer(directory):
    i=1
    for filename in sorted(os.listdir(directory)):
        print(filename)
        os.rename(directory + filename, directory + str(i) + '.png')
        i=i+1
# Start of program
# Directory where raw image captures have been stored
directory = '/home/citadel/Codes/LBNL/Image/'
# Calls the image cropping function
Cropper(directory)
# Calls the append text to images function
TextAdder(directory)
# Calls image renamer function
Renamer(directory)
```

Figure 148: Python programming language.

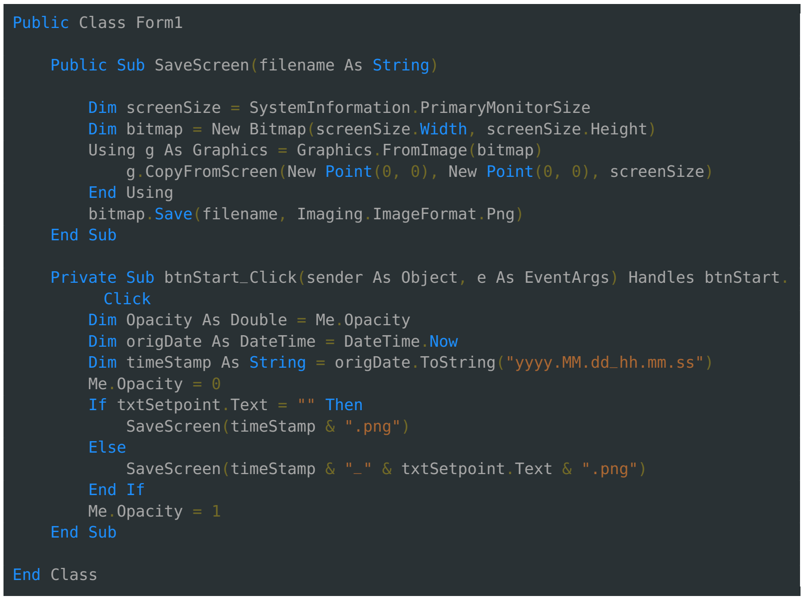

```
Public Class Form1

    Public Sub SaveScreen(filename As String)

        Dim screenSize = SystemInformation.PrimaryMonitorSize
        Dim bitmap = New Bitmap(screenSize.Width, screenSize.Height)
        Using g As Graphics = Graphics.FromImage(bitmap)
            g.CopyFromScreen(New Point(0, 0), New Point(0, 0), screenSize)
        End Using
        bitmap.Save(filename, Imaging.ImageFormat.Png)
    End Sub

    Private Sub btnStart_Click(sender As Object, e As EventArgs) Handles btnStart.
          Click
        Dim Opacity As Double = Me.Opacity
        Dim origDate As DateTime = DateTime.Now
        Dim timeStamp As String = origDate.ToString("yyyy.MM.dd_hh.mm.ss")
        Me.Opacity = 0
        If txtSetpoint.Text = "" Then
            SaveScreen(timeStamp & ".png")
        Else
            SaveScreen(timeStamp & "_" & txtSetpoint.Text & ".png")
        End If
        Me.Opacity = 1
    End Sub

End Class
```

Figure 149: Visual Basic programming language.

Glossary

Activator Small amount of impurities introduced to the lattice to enhance photon emission. 1

Afterglow Fraction of scintillating light present for a given period of time once the ionizing radiation has stopped. 6

Bragg's Law Diffraction relationship that defines the conditions presented by a set of crystallographic planes. 20

Compton scattering Scattering of a photon by a charged particle, typically an electron. 5

Conduction band Consists of electrons that have sufficient energy to travel throughout a material. This band is generally empty. 1

Convection Heat transfer by mass motion of a fluid such as air or water when the heated fluid is caused to move away from the source of heat, carrying energy with it. 18

Eddy currents The alternating current induced in a conductor when it is subjected to a time-varying magnetic field in accordance with Lenz's law. 17

Energy gap Also referred to as the band gap, this region is the forbidden gap where no electron states exist. This gap is located between the top of the valence band and the bottom of the conduction band. 1

Energy-dispersive x-ray spectroscopy Utilizes the photoelectric effect to produce a spectrum of counts that can identify elements within a compound. 21

Exciton An electrically neutral quasiparticle that occurs where an electron and an electron-hole are attracted to each other by electrostatic Coulomb forces. 6

Full width at half maximum Describes the width of a function where the distance between extreme points on the curve reaches half its maximum value. 5

Light yield A measure of light output from a scintillator, typically measured in photons/MeV, that is an important characteristic in determining an appropriate scintillator for an application. 4

Marangoni convection This effect (also called the Gibbs-Marangoni effect) is the mass transfer along an interface between two fluids due to surface tension gradient. In the case of temperature dependence, this phenomenon may be called thermo-capillary convection (or Benard-Marangoni convection). 19

Poiseuille flow Steady viscous fluid flow driven by an effective pressure gradient established between the two ends of a long straight pipe of uniform circular cross-section. First studied experimentally by J.L.M. Poiseuille in 1838. 19

Pyrometer A pyrometer is a type of remote-sensing thermometer used to measure the temperature of a surface. 26, 28

Scanning electron microscope A microscope that uses a focused electron beam to image samples.. 21

Scintillator A material possessing luminescent centers that absorbs high-energy photons and emits light in the visible or near-visible spectrum. 1

Valence band Highest range of electron energies in which electrons are typically present and are bound to the lattice structure. 1

X-ray luminescence Technique used to analyze emission spectra of scintillator crystals and determine the peak of its emission band. 21

X-ray powder diffraction Technique used to analyze fine powder samples based off the repeating lattice structure of a solid it can accurately determine compositions of compounds. 20

BIBLIOGRAPHY

[1] E. Auffray, D. Abler, S. Brunner, B. Frisch, A. Knapitsch, P. Lecoq, G. Mavromanolakis, O. Poppe, and A. Petrosyan. LuAG material for dual readout calorimetry at future high energy physics accelerators. *IEEE Nuclear Science Symposium Conference Record*, pages 2245–2249, 2009.

[2] M. Balcerzyk, M. Moszyński, M. Kapusta, D. Wolski, J. Pawelke, and C. L. Melcher. Yso, lso, gso and lgso. a study of energy resolution and nonproportionality. *IEEE Transactions on Nuclear Science*, 47(4):1319–1323, 2000.

[3] V.G. Baryshevsky, M.V. Korzhik, V.I. Moroz, V.B. Pavlenko, A.A. Fyodorov, S.A. Smirnova, O.A. Egorycheva, and V.A. Kachanov. $YAlO_3$:Ce-fast-acting scintillators for detection of ionizing radiation. *Nuclear Instruments and Methods in Physics Research Section B: Beam Interactions with Materials and Atoms*, 58(2):291–293, 1991.

[4] Y. Baskin and D.C. Schell. Phase studies in the binary system MgO-Ta_2O_5. *Journal of the American Ceramic Society*, 46(4):174–177, 1963.

[5] M. Belhaj, O. Jbara, S. Odof, K. Msellak, E.I. Rau, and M.V. Andrianov. An anomalous contrast in scanning electron microscopy of insulators: The pseudo-mirror effect. *Scanning*, 22(6):352–356, 2000.

[6] M.D. Birowosuto, P. Dorenbos, C.W.E. van Eijk, K.W. Krämer, and H.U. Güdel. High-light-output scintillator for photodiode readout: LuI_3:Ce_3. *Journal of Applied Physics [H.W. Wilson - AST]*, 99(12):123520, 2006.

[7] G. Blasse and B.C. Grabmaier. *Luminescent Materials*. Springer-Berlin Heidelberg, first edition, 1994.

[8] J.T.M. de Haas and P. Dorenbos. Advances in yield calibration of scintillators. *IEEE Transactions on Nuclear Science*, 55(3):860–864, June 2008.

[9] J.T.M. de Haas, P. Dorenbos, and C.W.E. van Eijk. Measuring the absolute light yield of scintillators. *Nuclear Instruments and Methods in Physics Research Section A: Accelerators, Spectrometers, Detectors and Associated Equipment*, 537(1-2):97–100, 2005.

[10] S.E. Derenzo, E.D. Bourret-Courchesne, M.J. Weber, and M.K. Klintenberg. Scintillation studies of CdS(In): effects of various semiconductor doping strategies. *Nuclear Instruments and Methods in Physics Research Section A: Accelerators, Spectrometers, Detectors and Associated Equipment*, 537(1-2):261–265, 2005.

[11] S.E. Derenzo, W.W. Moses, J.L. Cahoon, R.C.C. Perera, and J.E. Litton. Prospects for new inorganic scintillators. *IEEE Transactions on Nuclear Science*, 37(2):203–208, 1990.

[12] S.E. Derenzo, M.J. Weber, E.D. Bourret-Courchesne, and M.K. Klintenberg. The quest for the ideal inorganic scintillator. *Nuclear Instruments and Methods in Physics Research Section A: Accelerators, Spectrometers, Detectors and Associated Equipment*, 505(1-2):111–117, 2003.

[13] S.E. Derenzo, M.J. Weber, W.W. Moses, and C. Dujardin. Measurements of the intrinsic rise times of common inorganic scintillators. *IEEE Transactions on Nuclear Science*, 47(3):860–864, 2000.

[14] G. Dhanaraj. *Springer Handbook of Crystal Growth*. Springer-Verlag, first edition, 2010.

[15] P. Dorenbos. Electronic structure engineering of lanthanide activated materials. *Journal of Materials Chemistry*, 22(42):22344–22349, 2012.

[16] W. Drozdowski, P. Dorenbos, and J.T.M. de Haas. Scintillation properties of praseodymium activated $Lu_3Al_5O_{12}$ single crystals. *IEEE Transactions on Nuclear Science [H.W. Wilson - AST]*, 55(4):2420, 2008.

[17] C. Dujardin, C. Mancini, D. Amans, G. Ledoux, D. Abler, E. Auffray, P. Lecoq, D. Perrodin, A. Petrosyan, and K.L. Ovanesyan. LuAG:Ce fibers for high energy calorimetry. *Journal of Applied Physics*, 108(1), 2010.

[18] B.M. Epelbaum, G. Schierning, and A. Winnacker. Modification of the micro-pulling-down method for high-temperature solution growth of miniature bulk crystals. *Journal of Crystal Growth*, 275(1):867–870, December 2005.

[19] H.S. Fang, Z.W. Yan, and E.D. Bourret-Courchesne. Numerical study of the micro-pulling-down process for sapphire fiber crystal growth. *Crystal Growth & Design*, 11(1):121–129, 2011.

[20] T. Fukuda and V.I. Chani. *Shaped Crystals: Growth by Micro-Pulling-Down Technique*. Springer-Verlag, first edition, 2007.

[21] T. Fukuda, P. Rudolph, and S. Uda. *Fiber Crystal Growth from the Melt*, volume 6. Springer Berlin Heidelberg, 2004.

[22] A.V. Gektin. *Trends in Scintillation Crystals*, chapter 17, pages 299–312. Wiley-VCH Verlag GmbH and Co. KGaA, 2010.

[23] J. Glodo, E.V.D. van Loef, W.M. Higgins, and K.S. Shah. Mixed lutetium iodide compounds. *IEEE Transactions on Nuclear Science*, 55(3):1496–1500, 2008.

[24] B.C. Grabmaier. Crystal scintillators. *IEEE Transactions on Nuclear Science*, 31(1):372–376, 1984.

[25] B.C. Grabmaier, W. Rossner, and J. Leppert. Ceramic scintillators for x-ray computed tomography. *Physica Status Solidi (a)*, 130(2):K183–K187, April 1992.

[26] C. Greskovich and S. Duclos. Ceramic scintillators. *Annual Review of Materials Science*, 27(1):69–88, August 1997.

[27] G. Halle and H. Mueller-Buschbaum. Investigations of Zn(1-x) M(x)Ta_2O_6 (M = Mg, and Ni) with a refinement of the crystal structure of $MgTa_2O_6$. *Journal of The Less-Common Metals*, 142:263–268, September 1988.

[28] M. Higuchi, K. Ando, J. Takahashi, and K. Kodaira. Growth of $MgTa_2O_6$ single crystals by floating zone method and their optical properties. *Journal of the Ceramic Society of Japan*, 101(1):118–120, 1993.

[29] I. Holl, E. Lorenz, and G. Mageras. A measurement of the light yield of common inorganic scintillators. *IEEE Transactions on Nuclear Science*, 35(1):105–109, 1988.

[30] A. Jouini, H. Sato, A. Yoshikawa, T. Fukuda, G. Boulon, K. Kato, and E. Hanamura. Crystal growth and optical absorption of pure and Ti, Mn-doped $MgAl_2O_4$ spinel. *Journal of Crystal Growth*, 287(2):313–317, 2006.

[31] S. Kasap. *Principles of Electronic Materials and Devices*. McGraw-Hill Education, third edition, March 2005.

[32] W. Klamra, T. Szczesniak, M. Moszynski, J. Iwanowska, L. Swiderski, A. Syntfeld-Kazuch, V.N. Shlegel, Y.V. Vasiliev, and E.N. Galashov. Properties of $CdWO_4$ and $ZnWO_4$ at liquid nitrogen temperature. *IEEE Nuclear Science Symposium Conference Record*, pages 1561–1565, 2009.

[33] D. Klimm. The melting behavior of lutetium aluminum perovskite $LuAlO_3$. *Journal of Crystal Growth*, 312:730–733, 2010.

[34] H.J. Koh, Y. Furukawa, P. Rudolph, and T. Fukuda. Oxide mixed crystals grown by heater-immersed zone melting method with multi-capillary holes. *Journal of Crystal Growth*, 149(3):236–240, 1995.

[35] J.B. Kortright and A.C. Thompson. *X-ray data booklet*, chapter 1, pages 8–13. Lawrence Berkeley National Laboratory, 2009.

[36] V.N. Kurlov and B.M. Epelbaum. EFG growth of sapphire tubes up to 85 mm in diameter. *Journal of Crystal Growth*, 187(1):107–110, 1998.

[37] M. Laval, M. Moszyński, R. Allemand, E. Cormoreche, P. Guinet, R. Odru, and J. Vacher. Barium fluoride âĂŤ Inorganic scintillator for subnanosecond timing. *Nuclear Instruments and Methods In Physics Research*, 206(1):169–176, 1983.

[38] P. Lecoq, A. Annenkov, A. Gektin, M. Korzhik, and C. Pedrini. *Inorganic Scintillators for Detector Systems: Physical Principles and Crystal Engineering*. Springer-Verlag, first edition, 2006.

[39] W. Lehmann. Edge emission of n-type conducting ZnO and CdS. *Solid-State Electronics*, 9(11):1107–1110, 1966.

[40] A. Lempicki, E. Berman, A. J. Wojtowicz, M. Balcerzyk, and L.A. Boatner. Cerium-doped orthophosphates: new promising scintillators. *IEEE Transactions on Nuclear Science*, 40(4):384–387, 1993.

[41] A. Lempicki, M.H. Randles, D. Wisniewski, M. Balcerzyk, C. Brecher, and A.J. Wojtowicz. $LuAlO_3$:Ce and other aluminate scintillators. *IEEE Transactions on Nuclear Science*, 42(4):280, 1995.

[42] S. Liu, X. Feng, M. Nikl, L. Wu, Z. Zhou, J. Li, H. Kou, Y. Zeng, Y. Shi, Y. Pan, and A. Setlur. Fabrication and Scintillation Performance of Nonstoichiometric LuAG:Ce Ceramics. *Journal of the American Ceramic Society*, 98(2):510 – 514, February 2015.

[43] J.A. Mares, A. Beitlerova, M. Nikl, N. Solovieva, C. D'Ambrosio, K. Blazek, P. Maly, K. Nejezchleb, and F. de Notaristefani. Scintillation response of ce-doped or intrinsic scintillating crystals in the range up to 1 mev. *Radiation Measurements*, 38(4):353–357, 2004.

[44] C.L. Melcher, R.A. Manente, and J. S. Schweitzer. Applicability of barium fluoride and cadmium tungstate scintillators for well logging. *IEEE Transactions on Nuclear Science*, 36(1):1188–1192, 1989.

[45] C.L. Melcher, J.S. Schweitzer, C.A. Peterson, R.A. Manente, and H. Suzuki. Crystal growth and scintillation properties of the rare earth oxyorthosilicates. *Delft Unviersity Press*, SCINT95:309–316, 1996.

[46] E. Mihóková, M. Nikl, J.A. Mareš, A. Beitlerová, A. Vedda, K. Nejezchleb, K. Blažek, and C. D'Ambrosio. Luminescence and scintillation properties of YAG:Ce single crystal and optical ceramics. *Journal of Luminescence*, 126(1):77–80, 2007.

[47] V.B. Mikhailik, H. Kraus, S. Henry, and A.J.B. Tolhurst. Scintillation studies of $CaWO_4$ in the millikelvin temperature range. *Physical Review B*, 75(18):184308, May 2007.

[48] W.W. Moses and S.E. Derenzo. Cerium fluoride, a new fast, heavy scintillator. *IEEE Transactions on Nuclear Science*, 36(1):173–176, 1989.

[49] W.W. Moses, S.E. Derenzo, A. Fyodorov, M. Korzhik, A. Gektin, B. Minkov, and V. Aslanov. $LuAlO_3$:Ce-a high density, high speed scintillator for gamma detection. *Nuclear Science, IEEE Transactions on*, 42(4):275–279, August 1995.

[50] M. Moszyński, R. Allemand, M. Laval, R. Odru, and J. Vacher. Recent progress in fast timing with CsF scintillators in application to time-of-flight positron tomography in medicine. *Nuclear Instruments and Methods in Physics Research*, 205(1-2):239–249, 1983.

[51] M. Moszynski, M. Balcerzyk, and M. Kapusta. $CdWO_4$ crystal in gamma-ray spectrometry. *IEEE Transactions on Nuclear Science [H.W. Wilson - AST]*, 52(6):3124, 2005.

[52] M. Moszynski, M. Balcerzyk, and M. Kapusta. Growth of Yb^{3+}-doped Y_2O_3 single crystal rods by the micro-pulling-down method. *Materials Research Bulletin*, 40(8):1235 – 1243, 2005.

[53] M. Moszynski, M. Kapusta, M. Mayhugh, D. Wolski, and S.O. Flyckt. Absolute light output of scintillators. *IEEE Transactions on Nuclear Science*, 44(3):1052–1061, 1997.

[54] R.B. Murray. Use of Li6I(Eu) as a scintillation detector and spectrometer for fast neutrons. *Nuclear Instruments*, 2(3):237–248, 1958.

[55] N.G. Nause. Powder x-ray diffraction data for rare earth garnets. Master's thesis, Stephen F. Austin State University, 2003.

[56] M. Nikl, J.A. Mares, N. Solovieva, J. Hybler, A. Voloshinovskii, K. Nejezchleb, and K. Blazek. Energy transfer to the Ce^{3+} centers in $Lu_3Al_5O_{12}$:Ce scintillator. *Physica status solidi*, 201(7):R41 – R44, May 2004.

[57] M. Nikl, J.A. Mares, N. Solovieva, H. Li, X. Liu, L. Huang, I. Fontana, M. Fasoli, A. Vedda, and C. D Ambrosio. Scintillation characteristics of $Lu_3Al_5O_12$:Ce optical ceramics. *Journal of Applied Physics*, 104(3):033515 – 033515–5, 2005.

[58] J.A. Nolen. An easily prepared scintillator for viewing accelerator beam spots. *Nuclear Instruments and Methods*, 156(3):595–596, November 1978.

[59] A. Novoselov, H. Ogino, A. Yoshikawa, M. Nikl, J. Pejchal, J.A. Mares, A. Beitlerova, C. D'Ambrosio, and T. Fukuda. Study on crystal growth and luminescence properties of Pr-doped RE_2SiO_5 (RE=Y, Lu). *Journal of Crystal Growth*, 287(2):309–312, 2006.

[60] H. Ogino, A. Yoshikawa, M. Nikl, A. Krasnikov, K. Kamada, and T. Fukuda. Growth and scintillation properties of Pr-doped $Lu_3Al_5O_{12}$ crystals. *Journal of Crystal Growth*, 287(2):335–338, 2006.

[61] D.E. Persyk and T.E. Moi. State-of-the-art photomultipliers for anger cameras. *IEEE Transactions on Nuclear Science*, 25(1):615–619, 1978.

[62] A.G. Petrosyan, V.F. Popova, V.V. Gusarov, G.O. Shirinyan, C. Pedrini, and P. Lecoq. The Lu_2O_3-Al_2O_3 system, relationships for equilibrium-phase and supercooled states. *Journal of Crystal Growth*, 293(1):74–77, 2006.

[63] Y.D. Porter-Chapman, E.D. Bourret-Courchesne, and S.E. Derenzo. Bi3+ luminescence in abio2cl (a = sr, ba) and babio2br. *Journal of Luminescence*, 128(1):87–91, 2008.

[64] B.D. Ratner and D.G. Castner. *Electron Spectroscopy for Chemical Analysis*, pages 47 – 112. John Wiley and Sons, Ltd, 2009.

[65] C.R. Ronda and A.M. Srivastava. *Scintillators*, chapter 5, pages 105–132. Wiley-VCH Verlag GmbH and Co. KGaA, 2007.

[66] E. Sakai. Recent measurements on scintillator-photodetector systems. *IEEE Transactions on Nuclear Science*, 34(1):418–422, 1987.

[67] K.S.G. Shah, P. Wong, M. Klugerman, M.J. Weber, P. Dorenbos, W.W. Moses, T. Gupta, S.E. Derenzo, and W. Higgins. Lui3:ce–a new scintillator for gamma ray spectroscopy. *IEEE Transactions on Nuclear Science*, 51(5):2302, 2004.

[68] L. Swiderski, M. Moszynski, A. Nassalski, A. Syntfeld-Kazuch, T. Szczesniak, K. Kamada, K. Tsutsumi, Y. Usuki, T. Yanagida, and A. Yoshikawa. Light yield non-proportionality and energy resolution of praseodymium doped LuAG scintillator. *IEEE Transactions on Nuclear Science*, 56(3):934–938, 2009.

[69] A. Syntfeld, M. Moszynski, R. Arlt, M. Balcerzyk, M. Kapusta, M. Majorov, R. Marcinkowski, P. Schotanus, M. Swoboda, and D. Wolski. [sup.6]lii in neutron and [gamma]-ray spectrometry–a highly sensitive thermal neutron detector. *IEEE Transactions on Nuclear Science*, 52(6):3151–3156, 2005.

[70] C. Tealdi, M.S. Islam, L. Malavasi, and G. Flor. Defect and dopant properties of $MgTa_2O_6$. *Journal of Solid State Chemistry*, 177(11):4359–4367, 2004.

[71] C.W.E. van Eijk. Inorganic-scintillator development. *Nuclear Instruments and Methods in Physics Research Section A: Accelerators, Spectrometers, Detectors and Associated Equipment*, 460(1):1–14, 2001.

[72] C.W.E. van Eijk, J. Andriessen, P. Dorenbos, J. Jansons, N. Khaidukov, Z. Rachko, and J. Valbis. *Experimental and theoretical studies of cross luminescence*, pages 161–166. Editions Frontieres (Crystal 2000], 1993.

[73] C.W.E. van Eijk, J. Andriessen, P. Dorenbos, and R. Visser. Ce^{3+} doped inorganic scintillators. *Nuclear Instruments and Methods in Physics Research Section A: Accelerators, Spectrometers, Detectors and Associated Equipment*, 348(2-3):546–550, 1994.

[74] E.V.D. van Loef. Scintillation properties of LaBr3:Ce^{3+} crystals: fast, efficient and high-energy-resolution scintillators. *Nuclear Instruments and Methods in Physics Research Section A: Accelerators, Spectrometers, Detectors and Associated Equipment*, 486(1-2):254–258, 2002.

[75] E.V.D. van Loef, L.P. Dorenbos, C.W.E. van Eijk, K. Kramer, and H.U. Gudel. Scintillation properties of LaCl3:Ce^{3+} crystals: fast, efficient, and high-energy resolution scintillators. *IEEE Transactions on Nuclear Science*, 48(3):341, 2001.

[76] M.J. Weber. Inorganic scintillators: today and tomorrow. *Journal of Luminescence*, 100(1-4):35–45, 2002.

[77] M.J. Weber. Scintillation: mechanisms and new crystals. *Nuclear Instruments and Methods in Physics Research Section A: Accelerators, Spectrometers, Detectors and Associated Equipment*, 527(1-2):9–14, 2004.

[78] X. Xu, K. Lebbou, F. Moretti, K. Pauwels, P. Lecoq, E. Auffray, and C. Dujardin. Ce-doped LuAG single-crystal fibers grown from the melt for high-energy physics. *Acta Materialia*, 67:232–238, April 2014.

[79] T. Yanagida, Y. Fujimoto, Y. Yokota, K. Kamada, S. Yanagida, A. Yoshikawa, H. Yagi, and T. Yanagitani. Comparative study

of transparent ceramic and single crystal Ce doped LuAG scintillators. *Radiation Measurements*, 46(12):1503–1505, 2011.

[80] A. Yoshikawa, M. Nikl, G. Boulon, and T. Fukuda. Growth and luminescent properties of pr:ky3f10 single crystal. *Journal of Crystal Growth*, 285(4):445 – 449, 2005.

[81] Y.G. Zdesenko, F.T. Avignone, V.B. Brudanin, F.A. Danevich, S.S. Nagorny, I.M. Solsky, and V.I. Tretyak. Scintillation properties and radioactive contamination of $CaWO_4$ crystal scintillators. *Nuclear Instruments and Methods in Physics Research Section A: Accelerators Spectrometers Detectors and Associated Equipment*, 538(1):657–667, 2005.

[82] Y. Zorenko, V. Gorbenko, I. Konstankevych, B. Grinev, and M. Globus. Scintillation properties of $Lu_3Al_5O_{12}$:Ce single-crystalline films. *Nuclear Instruments and Methods in Physics Research Section A: Accelerators, Spectrometers, Detectors and Associated Equipment*, 486(1-2):309 – 314, 2002.

Index